CR 134214

HREC-1156-1
LMSC/HREC D162657

LOCKHEED MISSILES & SPACE COMPANY
HUNTSVILLE RESEARCH & ENGINEERING CENTER
HUNTSVILLE RESEARCH PARK
4800 BRADFORD DRIVE, HUNTSVILLE, ALABAMA

SPACE SHUTTLE VEHICLE ROCKET PLUME IMPINGEMENT STUDY FOR SEPARATION ANALYSIS

TASKS II and III

DEFINITION AND PRELIMINARY PLUME IMPINGEMENT ANALYSIS FOR THE MSC BOOSTER

November 1970

Contract NAS9-11156

by

Carl J. Wojciechowski
Morris M. Penny
Robert J. Prozan

APPROVED: George D. Reny, Manager
Aeromechanics Dept.

J. S. Farrior
Resident Director

FOREWORD

This report presents the results of Tasks II and III performed by Lockheed's Huntsville Research & Engineering Center for the Flight Technology Branch of NASA's Manned Spacecraft Center, Houston, Texas. This work was performed under Contract NAS9-11156 and was monitored by Mrs. I. H. Fossler.

Task I was previously issued as Lockheed document LMSC/HREC D162574, dated August 1970.

SUMMARY

This document presents the results of a space shuttle plume impingement study for the Manned Spacecraft Center configuration. This study was conducted as two tasks which were to: (1) define the orbiter main stage engine exhaust plume flow field, and (2) define the plume impingement heating, force and resulting moment environments on the booster during the staging maneuver. To adequately define these environments during the staging maneuver and allow for deviation from the nominal separation trajectory, a multitude of relative orbiter/booster positions are analyzed which map the region that contains the separation trajectories. The data presented in this report can be used to determine a separation trajectory which will result in acceptable impingement heating rates, forces, and the resulting moments. The data, presented in graphical form, include the effect of roll, pitch and yaw maneuvers for the booster.

Quasi-steady state analysis methods were used with the orbiter engine operating at full thrust. To obtain partial thrust results, simple ratio equations are presented. Using a simplified thrust buildup curve, the heating rate time histories to selected points on the booster vertical tail are used in a one-dimensional heat conduction program to calculate the surface temperature-time histories. These surface temperature-time histories are calculated for two separation trajectories. The maximum calculated surface temperature at the leading edge of the vertical tail is 1800°F for both of the separation trajectories analyzed. The titanium skin on the sides of the vertical tail reached 480°F and 440°F for the two separation trajectories analyzed.

The plume impingement force and moment analysis for the booster discloses several cases which could be potential problems during staging. The analysis revealed that if the booster was perturbed in the yaw plane during the staging sequence, the orbiter plume will produce an unstable condition for the booster, i.e., moments generated during plume impingement will augment the booster yaw motion. The analysis also reveals that the orbiter plume impingement will produce moments in pitch that will augment any positive pitch motion of the booster.

CONTENTS

NOMENCLATURE

A	area, units consistent with surface equations
A/A*	engine area ratio, dimensionless
C_{ps}	stagnation pressure coefficient behind a normal shock, dimensionless
erf(γ, S)	error function of the molecular speed ratio, S_R
e	denotes unit vector quantity
$\vec{F}$	force vector, $F_x\hat{i} + F_y\hat{j} + F_z\hat{k}$, lb_f
K_n	Knudsen number, dimensionless
k, ℓ, t	direction cosines between the subshape axis system and the local force direction
M	number of elemental areas used to describe a given subshape
$\vec{M}$	moment vector, $M_x\hat{i} + M_y\hat{j} + M_z\hat{k}$, ft-$lb_f$
M_N	component of Mach number normal to the elemental area, dimensionless
N	number of subshapes, used in Eqs. (C-6) and (C-8)
O/F	engine propellant oxidizer to fuel ratio, dimensionless
P	local static pressure, psi
P_{imp}	body/local impact pressure, psi
R	gas constant, $ft^2/sec^2/^oR$
S_R	molecular speed ratio, V/ 2RT
$\vec{r}$	distance vector, units consistent with subshape surface equation
T	local static temperature, ^oR
T_i	incident molecular temperature, ^oR
T_R	reflected molecular temperature and is equal to the body temperature for complete energy accommodation
$[T_{M-B}]$	transformation matrix from a given subshape coordinate system to the booster reference coordinate system

S	entropy, $ft^2/sec^2/^oR$
V	velocity, ft/sec
$\hat{i}, \hat{j}, \hat{k}$	plume Cartesian coordinate system
$\hat{i}, \hat{j}_r$	plume cylindrical coordinate system

Greek

α	local impingement angle of velocity vector with respect to the local body surface tangent (degrees)
β	1/2 RT
γ	ratio of specific heats, dimensionless
$\vec{\eta}$	local surface unit normal vector written in local subshape coordinate system
ξ	density of molecules
ρ	density, $slugs/ft^3$
ρ, γ, η	direction cosines between the subshape local axis system and the mass velocity
$\sum$	indicates summation
Λ	unit vector

Subscripts

∞	indicates free stream conditions
tran	indicates transitional flow regime
cont	indicates continuum flow regime
f.m.	indicates free-molecular flow regime
B.N.	indicates booster nose
θ_{exit}	engine lip angle, degrees

Section 1
INTRODUCTION

The separation of launch vehicle stages during boost usually results in the rocket exhaust plume from the upper stage impinging on the lower stage. For expendable boosters, the impingement has historically been of minor consequence. For the fully reusable space shuttle vehicle, however, the impingement problem is significant because control of the lower stage must be maintained, and the structure must not be damaged. The impingement environment imposed on the booster can be severe if ignition of the orbiter main propulsion system occurs while the stages are close together. If ignition of the orbiter is delayed until after the booster is far away, resulting in the impingement environment being either inconsequential or nonexistent, then payload performance penalties can occur. An assessment is needed of the significance of the staging plume impingement problem along with the definition of an "optimum" staging trajectory. This optimum trajectory should provide an acceptable tradeoff between impact of the vehicle design to accept the plume impingement environment and penalties incurred in system performance and/or operation.

Task II of this contract defines the engine plume flow field of the Manned Spacecraft Center (MSC) Space Shuttle orbiter and is presented in this document as Appendix A. Task III, presented in the following sections, defines the orbiter plume impingement heating, force, and moment environments on the MSC booster during the staging maneuver.

1.1 PROBLEM DESCRIPTION

The geometrical orientation for the MSC Space Shuttle arrangement is shown in Fig. 1.1. A reference coordinate system is located at the nose of the booster on the vehicle centerline. All forces and moments presented are referenced to this point. A simulated multiple nozzle was used to represent the main stage engines of the orbiter. The simulated nozzle has the same mass flow rate as the orbiter engine cluster and approximately the same plume shape. Details of the orbiter plume generation are presented in Appendix A.

1.2 DEFINITION OF THE PLUME IMPINGEMENT CHARACTERISTICS

The impingement characteristics were calculated by Lockheed's Plume Impingement Computer Program. Basically, the procedure for obtaining the impingement characteristics is as follows:

The vehicle (composite shape) and the particular motor are located with respect to the reference coordinate system. The composite shape is represented by a number of geometrically simple subshapes (each of which has its own local coordinate system). These subshapes are then subdivided into elemental areas. Local flow conditions on a given body are obtained by locating the centroid of each elemental area in the free plume from a search of the plume flow field which is stored on magnetic tape. The flow properties thus obtained are assumed to act uniformly over the elemental area.

The body local flow regimes were determined by the value of the local Knudsen number. In this analysis, continuum flow was assumed to exist for Knudsen numbers less than 0.01; transitional flow exists for Knudsen numbers between 0.01 and 10.0; and Knudsen numbers greater than 10.0 define the "free molecular flow" regime. The characteristics length used in the Knudsen number calculations were a representative dimension (element area dimension) of the body in question so that the elemental area local flow regime is determined by comparing the mean free molecular path of the local plume to the body dimension.

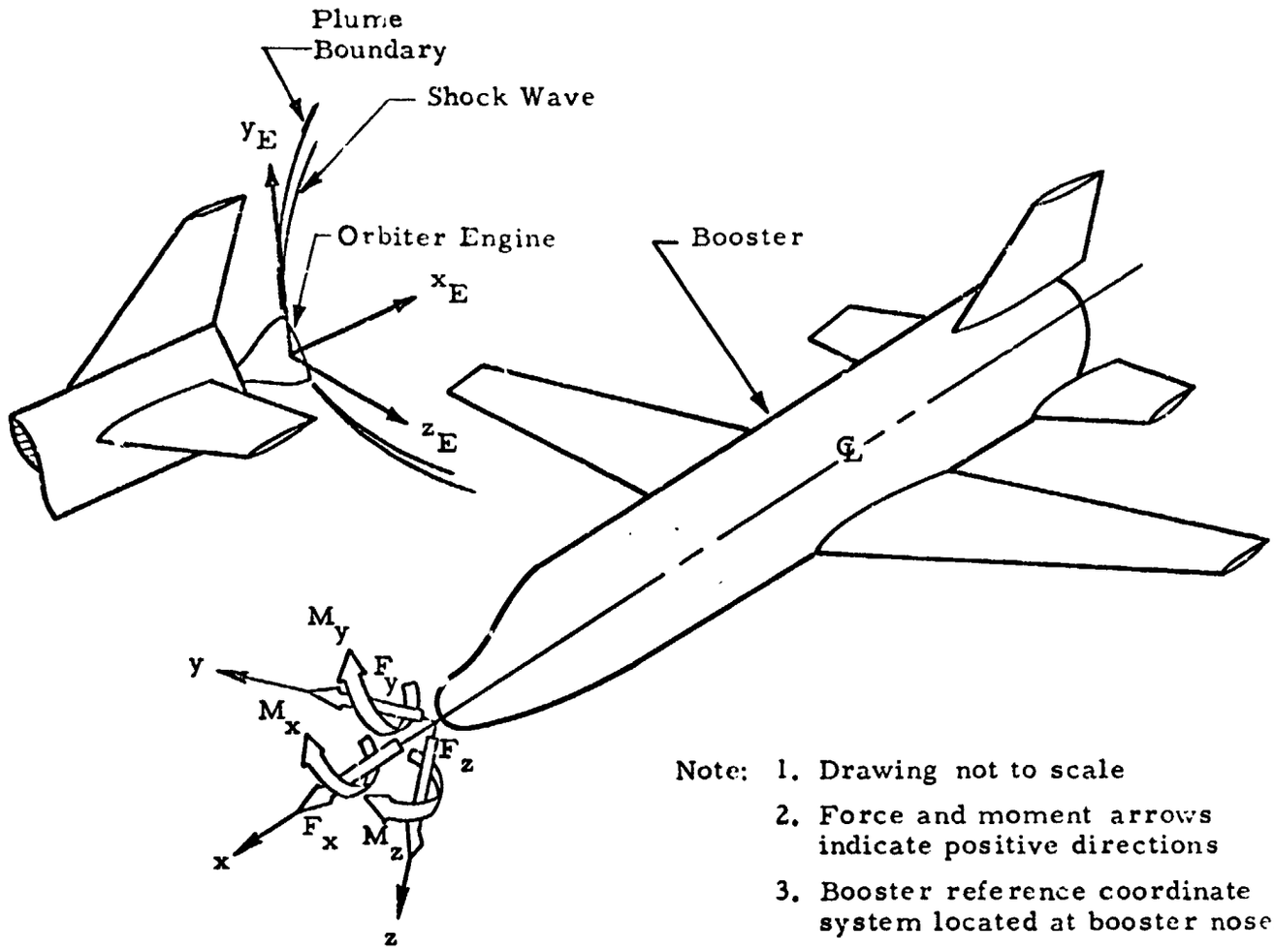

Fig. 1-1 - Three-Dimensional Perspective of the Booster Reference Coordinate System and the Orbiter Plume Coordinate System

The plume coordinates with respect to the surface immersed in the plume are shown in the sketch below:

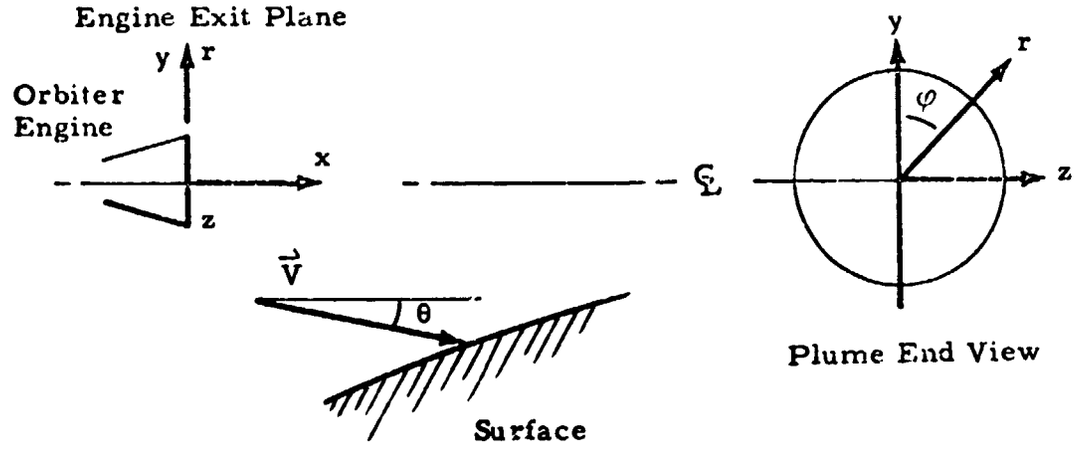

The body local flow properties are computed for a surface immersed in a free plume. The properties for a point r, x in the plume coordinate system are obtained from a search of the flowfield data stored on magnetic tape. The tape search routines use a four-point interpolation scheme to obtain the flow properties at the point (r, x).

The plume velocity vector is given by:

$$\vec{V} = V_x \hat{i} + V_r \hat{j}_r \tag{1}$$

where

$$\begin{aligned} V_x &= V \cos\theta \\ V_r &= V \sin\theta \end{aligned} \tag{2}$$

The velocity vector at the body point with respect to the radial orientation within the plume is given by:

$$\vec{V} = V_x \hat{i} + V_y \hat{j} + V_z \hat{k} \tag{3}$$

where

$$\left.\begin{aligned} V_y &= V_r \cos\varphi, \quad \cos\varphi = y/r \\ V_z &= V_r \sin\varphi, \quad \sin\varphi = z/r \end{aligned}\right\}. \tag{4}$$

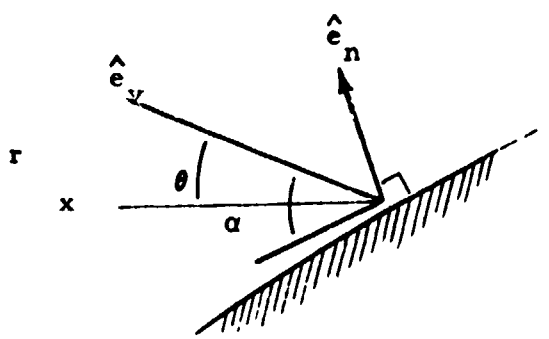

α = inclination of the local velocity vector with respect to the local surface tangent

The body local impingement angle (shown in the sketch above) is then given by

$$\alpha = 90.0 - 57.295778 \left(\cos^{-1}(\hat{e}_v \cdot \hat{e}_n)\right). \tag{5}$$

Section 2
DISCUSSION OF RESULTS

The MSC booster configuration analyzed is depicted in Fig. 2-1a. The overall dimensions used are shown as well as the locations of each of the vehicle subshapes (i.e., wings, tail, fuselage, etc.) analyzed. The solid outlines show the vehicle shape as analyzed while the dashed outlines show the actual vehicle shape. Fig. 2-1b shows a three-dimensional perspective view of the booster reference coordinate system used as well as the orbiter plume reference coordinate system used.

Shown on Fig. 2-1c are the assumed directions of positive yaw, ψ, pitch, θ and roll, φ, of the booster as used to generate the data in Figs. 2-2 through 2-22. Also indicated is the coordinate transformation matrix used to locate the booster nose with respect to the orbiter plume coordinate system (Fig. 2-1c). It should be noted that the order of axis rotation to obtain the transformation matrix is the yaw, pitch and roll directions, respectively. A discussion of the method used to obtain the properties at a point on the booster with respect to the orbiter plume is given in Appendixes B and C, respectively.

In the plume impingement analysis, the various components of the booster were represented by four basic subshapes (Fig. 2-1d). These were: (1) a cylinder for the upper portion of the fuselage; (2) flat plates for the lower sides of the fuselage; (3) a conical nose; and (4) airfoil shape NACA 0012-64 for the wing, vertical and horizontal tails, respectively. A detailed description of the airfoil subroutine is presented in Appendix B.

In the numerical integration scheme, the cylindrical portion of the fuselage and the conical nose section were divided in rings of 100 inches in

increment with each ring further subdivided into 10-degree radial increments. All wing sections were divided into approximately 50-inch increments in the span direction. As discussed in Appendix B, a cosine distribution function is used to distribute the chord direction. This scheme biases the point distribution to wing-leading edge where largest gradients in surface curvature occur. Twenty increments in the chord direction were used on the wing, horizontal and vertical tail surfaces. Uniform flow was assumed to exist over each elemental area of the respective surfaces with vacuum conditions considered to exist on the surfaces not exposed to the engine exhaust plume. Figs. 2-1e through 2-1m show various subshapes used to represent the booster. All wing surfaces (see Appendix B) were represented by airfoil shape NACA 0012-64.

A graphic representation of the orbiter engine exit plane/booster separation distances used to map the plume impingement environment on the booster are shown in Fig. 2-1n as "o" points. A plume overlay is provided with Fig. 2-1n to aid in visualization of the orbiter exhaust plume impingement on the various booster surfaces. The basic plume used in the analysis (see Appendix A) was generated assuming the staging altitude to be 283,000 feet with a freestream Mach number of 12.08. The resulting plume shape and distribution of plume flow field properties are shown on Figs. A-1 through A-6.

2.1 IMPINGEMENT FORCE AND MOMENT ANALYSIS

The resultant forces and moments acting on the booster resulting from the orbiter main stage engine exhaust plume impingement are presented in Figs. 2-2 through 2-22. The data presented comprise a map of the expected forces and moments acting on the booster over the region of the separation trajectory of the orbiter vehicle (Fig. 2-1n). For this study the reference coordinate system for the moments is located at the nose of the booster

(Fig. 2-1b). The moment data as presented can be referenced to the booster center of gravity by the following relation:

$$\vec{M}_{c.g.} = \vec{M}_{b.n.} - \vec{r}_{c.g.} \times \vec{F}_{b.n.}; \qquad (3.1)$$

where the vector quantity $\vec{r}_{c.g.}$ is the vector from the booster nose to the booster c.g.

The impingement data presented were generated assuming the orbiter main stage engine to be operating at full thrust. However, the force and moment components at any time, t, during the engine buildup to full thrust may be approximated by multiplying the force and moment data by the ratio of the chamber pressure at the time, t, to an engine chamber pressure of 3000 psia (see discussion in Appendix C).

Figs. 2-2 through 2-4 show the impingement force and moment maps for the zero pitch, roll and yaw cases. All physical dimensions are with respect to the reference coordinate system and are located at the booster nose and indicate various positions of the orbiter engine exit plane with respect to the booster nose. Since that portion of the booster which is subject to orbiter exhaust plume impingement is symmetrical about the booster centerline (Fig. 2-1b), the moments acting about the booster x (roll) and z (yaw) axes are zero with a zero force component in the y direction also. Due to the large change in the impingement forces and the resulting moments over the region of interest a semi-log interpolation scheme should be employed when using the data in tabulated form. The very large increase in the magnitude of the impingement data is due to the booster surfaces becoming more fully immersed in the orbiter exhaust plume as the separation distance between the vehicle increases.

Figs. 2-5 through 2-7 present impingement data for the booster due to a 5-degree pitch maneuver of the booster with respect to the orbiter exhaust

plume. This maneuver represents a rotation of the booster nose into the orbiter exhaust plume. Figs. 2-8 through 2-10 present the impingement data for the booster pitched minus 5-degrees with respect to the orbiter exhaust plume. An examination of the figures which show the positive moment direction and the impingement data of Figs. 2-7 and 2-8 indicates the following interesting problem. When the booster is rotated in a positive pitch maneuver (+ pitch) the resulting moment will tend to augment the rotation (continue to rotate the vehicle in the positive pitch direction). However, the resulting pitching moment for a maneuver which tends to pitch the booster vehicle in the negative pitch direction (-pitch) will tend to counteract the original direction of rotation; i.e., the direction of rotation due to the pitching moment would be opposite the original direction of rotation of the booster nose. The above discussion is true for all cases in which the plume impingement center of pressure, (booster location where the resultant plume impingement force is acting) is aft of the booster center of gravity. The reverse is true when the plume impingement center of pressure moves forward of the booster center of gravity (which would occur at large separation distances).

Figs. 2-11 through 2-16 present the impingement data for a 5-degree roll maneuver of the booster while Figs. 2-17 through 2-22 present the impingement data for a 5-degree yawing maneuver. Two items of consequence should be noted here. First, similar to the positive pitch case discussed previously, any yawing maneuver will result in an unstable action of the booster in the yaw direction. That is, the direction of rotation of the yawing moment acting on the booster due to the orbiter exhaust plume impingement will be in the same direction as the yawing maneuver. Hence the yawing moment due to the orbiter exhaust plume impingement produces an unstable rotation about the booster z axis (Fig. 2-1b). This action could result from any one of several causes. These include: (1) one engine out of the (side-by-side" engine arrangement; (2) an engine lag in the ignition sequence for

the side-by-side mounted engines; (3) angularities and misalignment of the wings, horizontal and vertical tail sections mating to the booster fuselage; and (4) angularities and misalignment in the engine manufacture and attachment at the engine gimbal station.

The second item of consequence is the roll moment acting on the vehicle during a vehicle rolling or yawing maneuver. During the initial phase of the staging sequence a rolling maneuver in the positive roll direction (Fig. 2-1c) will produce a moment which tends to increase the roll. As the vertical distance as well as the axial distance between the vehicles increases, however, the plume external shock will impinge on the wing or horizontal tail surfaces. This greatly increases the local loading on the surface which is being rotated into the plume. Hence, the increased loading will produce a change in the roll moment direction and will tend to then act in a direction opposite the vehicle roll direction. It should also be noted that a yawing maneuver will produce a roll moment acting on the vehicle. This results since the yawing rotation about the vehicle z axis will tend to produce nonsymmetric orbiter exhaust plume impingement. The loading on the wings horizontal and vertical tails are then unequal so that a roll moment is also produced.

Vacuum conditions were assumed to exist on all surfaces not subject to the orbiter exhaust plume impingement. A preliminary calculation indicated the aerodynamic force at the separation altitude of 283,000 feet is negligible compared to the predicted impingement forces.

The results of this study were obtained using an equivalent plume which has the same mass flow rate as the main stage engines. This analysis included the effects of the nozzle lip shock in the impingement analysis. A more detailed study which includes the effects of the nozzle internal shock wave and the shock wave resulting from the intersection of the two engine plumes will result in a redistribution of the local impingement properties in the vicinity

of the shock wave. However, the trends predicted by this study are considered to be a reasonable representation of the actual case. Therefore, the results of the study during this phase should give realistic data for use in preliminary staging studies and for defining potential problems such as those discussed above.

2.2 IMPINGEMENT HEATING ANALYSIS

Details of the methods used to calculate the plume impingement heating rates are presented in Appendix D. Briefly, yawed infinite cylinder theories were used to predict the stagnation line heat transfer rates to the fuselage, wings and tail surfaces in the continuum regime. Simple heat transfer distribution functions which are st ongly dependent on the ratio of the local pressure to the stagnation line pressure were used to predict heat transfer rates off the stagnation lines. For the range of separation distances studied, only the continuum regime was encountered.

The vertical tail (sketched below) will experience the highest impingement heating rates. The point A noted on the sketch is at the leading edge of

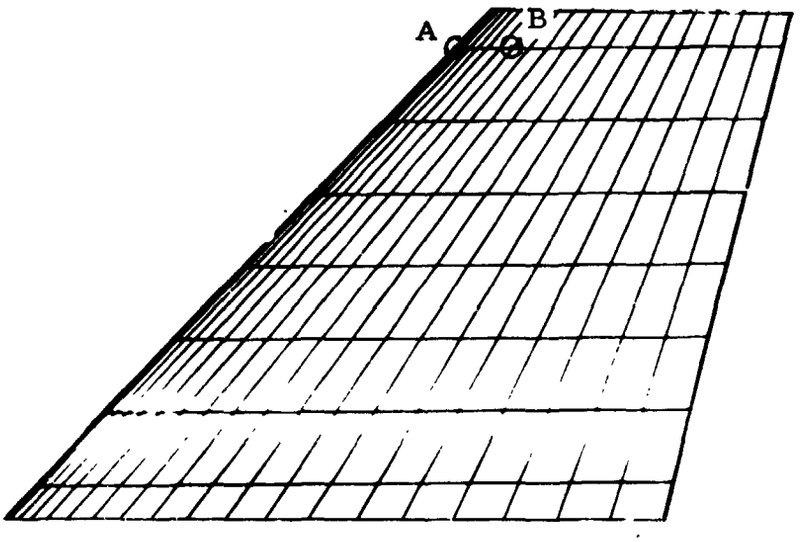

Fig. 2-23 - MSC Booster Vertical Tail

a chord located 27 inches from the top of the tail. The heating rates to this point are presented in Fig. 2-24 as a function of orbiter/booster separation distance. Shown on the figure is a line separating the turbulent from the laminar heating rates. The heating rates presented in Fig. 2-24 are full thrust values. Heating rate values for partial thrust values can be obtained from the following equation using the chamber pressure ratio, i.e., for turbulent flow,

$$\dot{Q}_{turb} = \dot{Q}_{\substack{full \\ thrust}} \times \left(\frac{\text{Chamber Pressure}}{3000 \text{ psi}}\right)^{0.8}$$

and for laminar flow,

$$\dot{Q}_{lam} = \dot{Q}_{\substack{full \\ thrust}} \times \left(\frac{\text{Chamber Pressure}}{3000 \text{ psi}}\right)^{0.5} .$$

Fig. 2-25 shows the variation of the heating rate along the stagnation line on the vertical tail for cases*1-14 denoted in Fig. 2-1n. For case 1, the variation of the heating rate along the chord of the vertical tail containing point A (refer to Fig. 2-23, page 2-6) is plotted in Fig. 2-26. It can be seen in Fig. 2-26 that the heating rate drops off rapidly away from the stagnation line.

Shown in Fig. 2-27 are the heating rate contours on the vertical tail for cases 1, 4, 10, 12 and 15. The heating rates shown in Fig. 2-27 do not include any localized effect due to the nozzle lip shock/fin bow shock interaction phenomena. It is planned to treat these phenomena in more detail in a subsequent report. Fig. 2-27e shows the increased heating to the vertical tail as the orbiter engine exit plane is moved closer to it. The variation of the heating rates along the top of the fuselage ahead of the root of the tail are shown in Fig. 2-28. They also do not contain any localized effects due to the nozzle lip shock/fuselage bow shock interaction phenomena. The distributions of the heating

* Case denotes Trajectory Point on Fig 2-1n

rates away from the stagnation line for a chord on the fuselage 5 inches in front of the root of the vertical tail are shown in Fig. 2-29 for cases 10 and 12.

In order to obtain the effect of these impingement heating rates on the skin temperature of the vertical tail a transient one-dimensional heat conduction analysis was performed. The separation trajectory used was the one labeled "trajectory 1, nominal" in Fig. 2-1n. The thrust-time buildup curve used is shown in Fig. 2-30. The points on the vertical tail that were analyzed are points A and B noted in Fig. 2-23. At point A, the leading edge, a 0.25-inch thick, carbon/carbon material was used. This leading edge material extends back to point B (approximately 15% of the chord length) where a titanium skin, 0.05-inch thick was used. The heating rates to points A and B versus time are plotted in Fig. 2-31 for this trajectory. The surface temperature-time histories are shown in Fig. 2-32 for the leading edge (point A) and the side of the vertical tail (point B). Point A reached a maximum temperature of 1800°F and point B reached a maximum temperature of 480°F, both below the structural temperature limits of 2700°F and 600°F, respectively. An initial temperature of 300°F was assumed in this analysis.

Since the more vertical separation trajectory maneuver is also of interest, the separation trajectory labeled "trajectory 2, vertical" in Fig. 2-1n was also analyzed. The heating rate contour plots on the vertical tail for selected orbiter/booster separation positions along this trajectory are shown in Fig. 2-33.

The variation of the heating rates along the leading edge of the vertical tail for selected points along trajectory 2 are shown in Fig. 2-34. The heating rate-time histories for points A and B on the vertical tail for trajectory 2 are shown in Fig. 2-35. The surface temperature-time histories for these points are shown in Fig. 2-32. It can be seen in Fig. 2-32 that the leading

edge temperature reached the same maximum (1800°F) as in separation trajectory 1. The titanium skin (point B) reached a temperature of 440°F or 40°F less than trajectory 1.

For separation trajectory 1 there was very little direct plume impingement on the booster fuselage ahead of the root of the vertical tail, therefore no surface temperature response was calculated for the booster. Only cases 10 and 12 had any impingement on the booster and these heating rates were rather low (4-6 Btu/ft^2-sec). This, combined with the fact that the heating rate pulse would only be for 2 to 3 seconds indicated that the surface temperature would remain below the structural limit of 600°F. For separation trajectory 2 there was no direct plume impingement on the booster ahead of the root of the vertical tail.

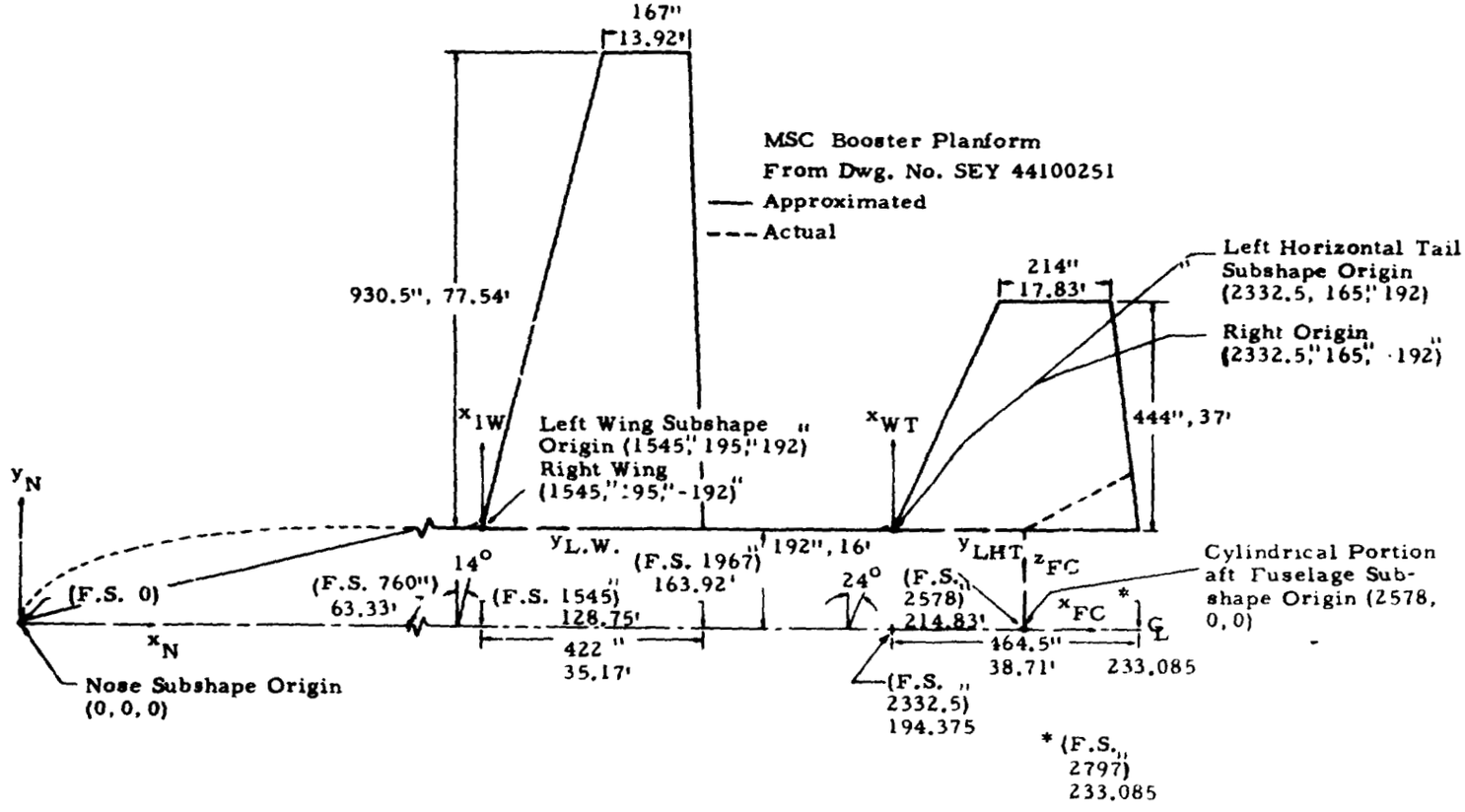

Fig. 2-1a - Schematic of Space Shuttle Booster Geometry and Booster Representation for Plume Impingement Analysis

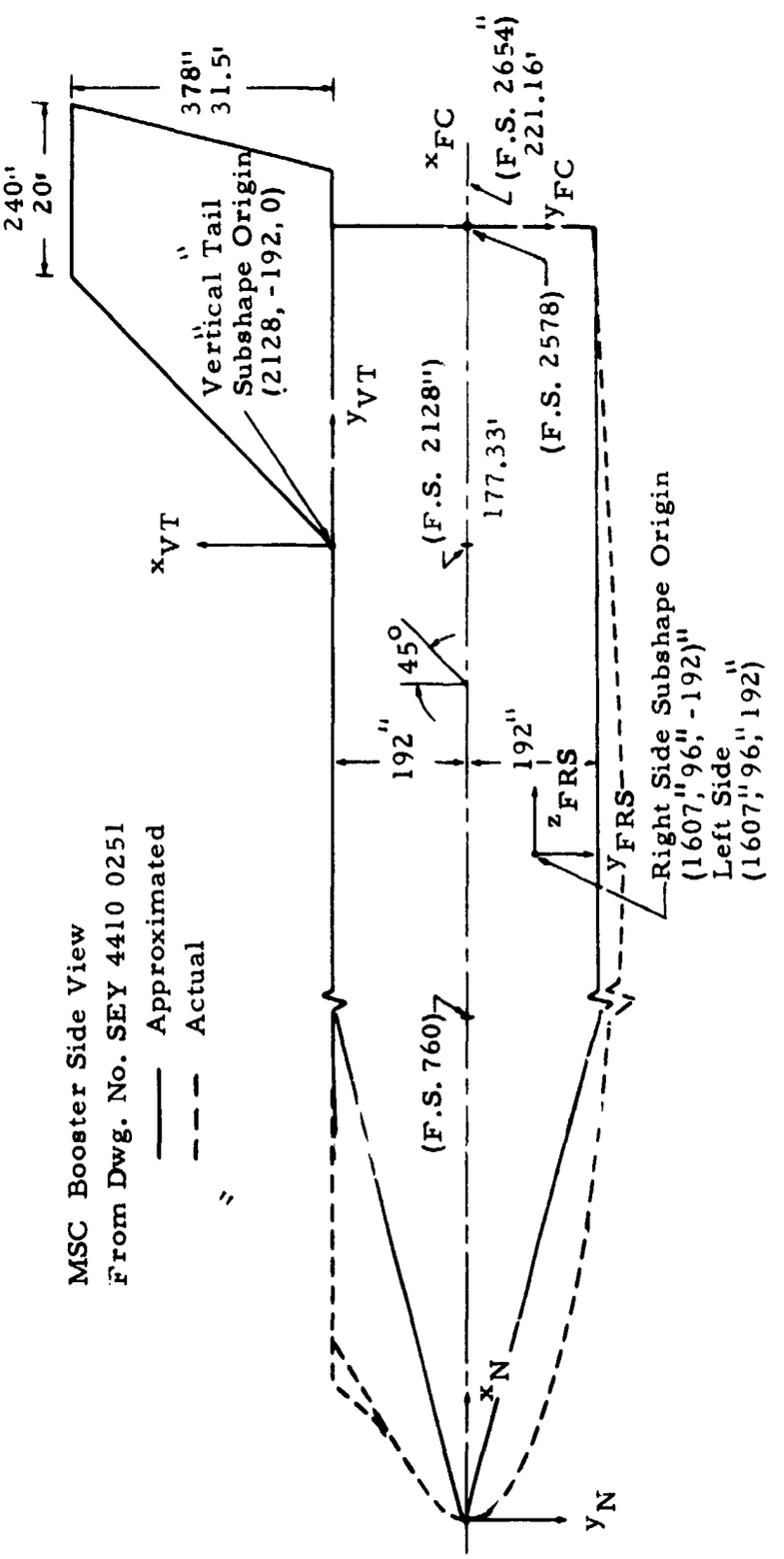

Fig. 2-1a (Continued)

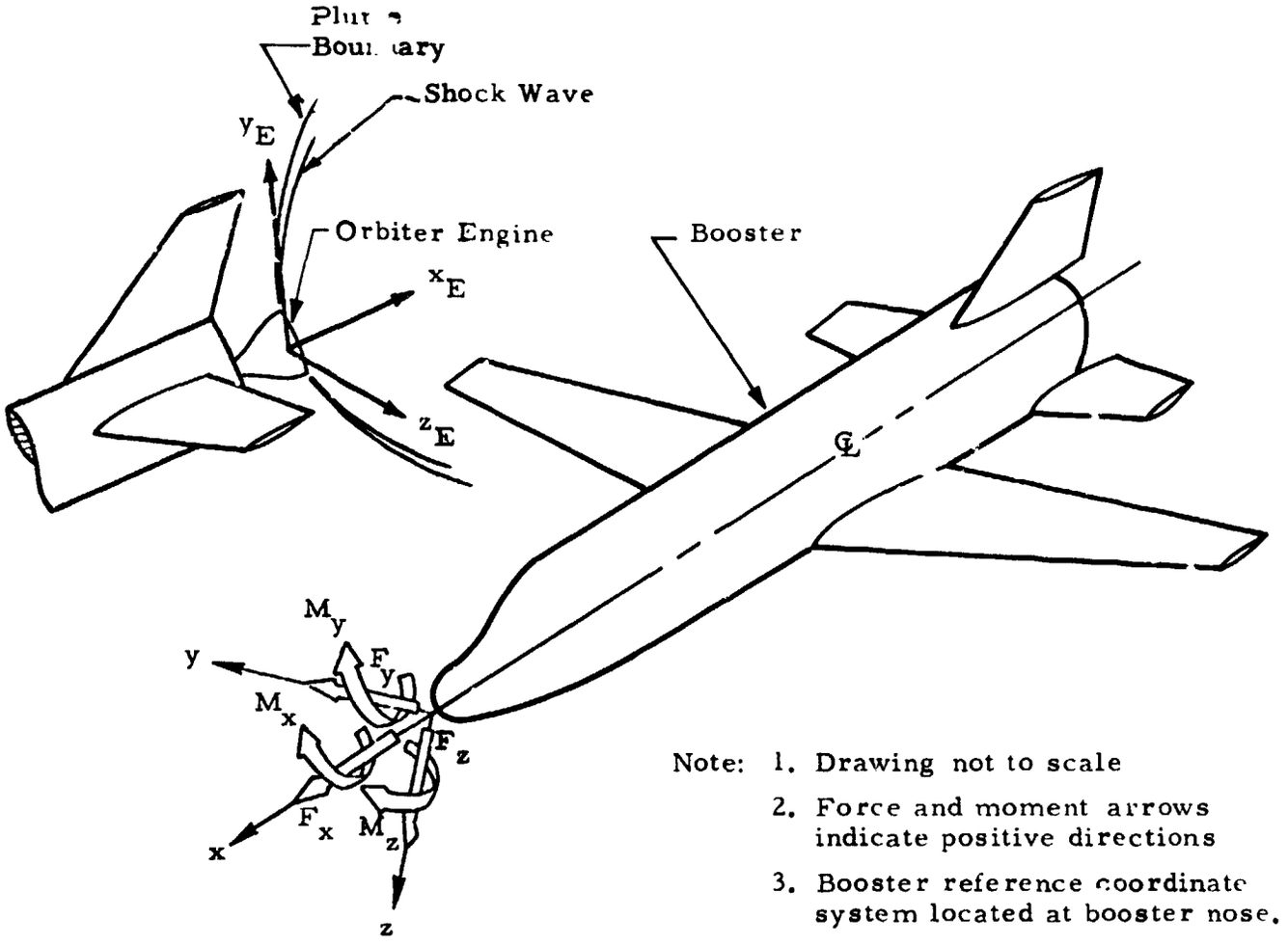

Fig. 2.1-b - Three-Dimensional Perspective of the Booster Reference Coordinate System and the Orbiter Plume Coordinate System

Transformation matrix from the booster coordinate system to the orbiter engine coordinate (order of axis rotations are: ψ, θ, φ)

$$\begin{Bmatrix} i \\ j \\ k \end{Bmatrix}_E = \begin{bmatrix} -\cos\theta\cos\varphi & \sin\theta & -\cos\theta\sin\varphi \\ -(\cos\psi\sin\varphi\sin\theta - \cos\varphi\sin\psi) & -\cos\theta\sin\varphi & -(\sin\psi\sin\varphi\sin\theta + \cos\varphi\cos\psi) \\ -(\cos\psi\cos\varphi\sin\theta + \sin\varphi\sin\psi) & -\cos\theta\cos\varphi & -(\sin\psi\cos\varphi\sin\theta - \sin\varphi\cos\psi) \end{bmatrix} \begin{Bmatrix} i \\ j \\ k \end{Bmatrix}_B \quad R_{E_N}$$

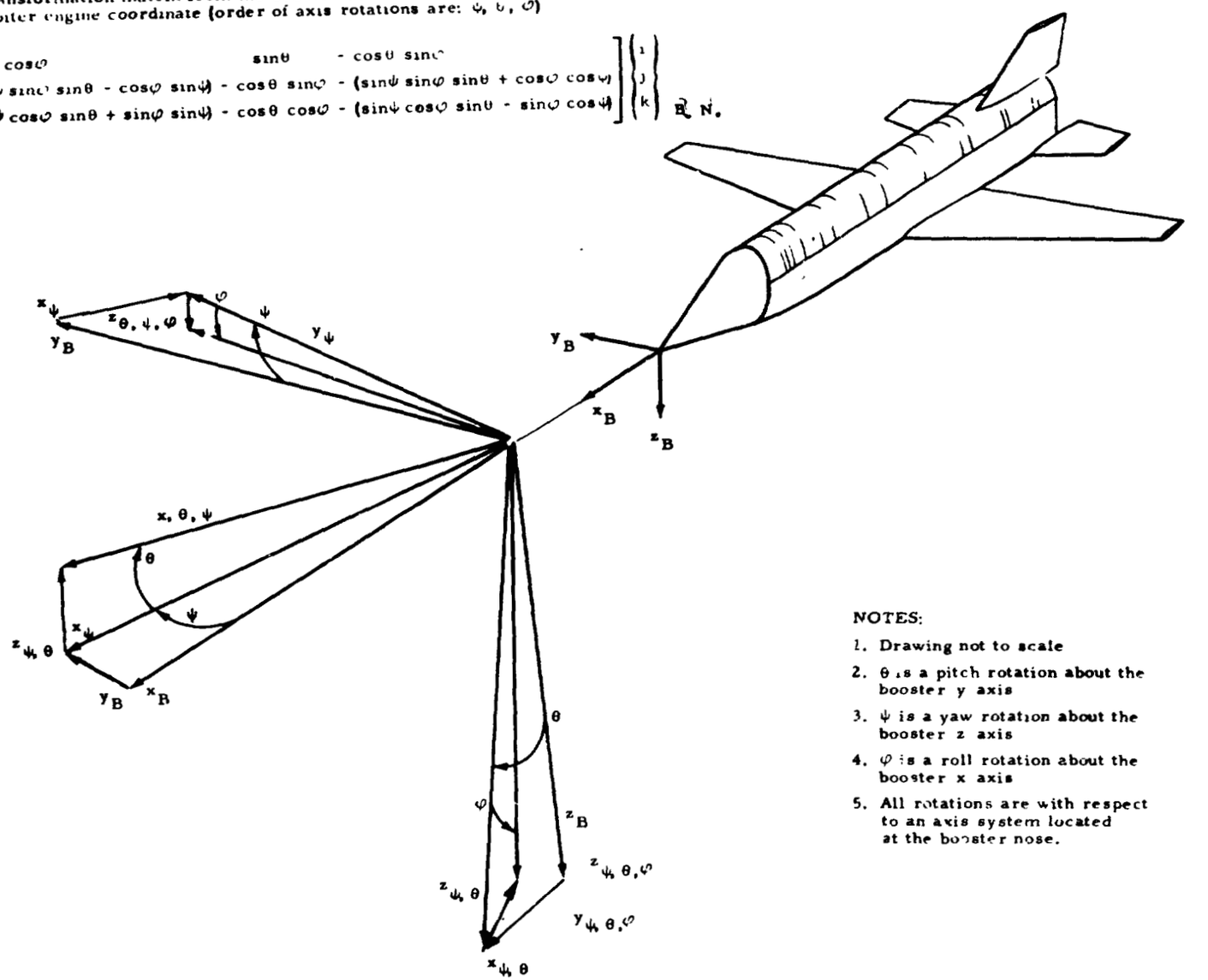

NOTES:

1. Drawing not to scale
2. θ is a pitch rotation about the booster y axis
3. ψ is a yaw rotation about the booster z axis
4. φ is a roll rotation about the booster x axis
5. All rotations are with respect to an axis system located at the booster nose.

Fig. 2-1c – Three-Dimensional Perspective of Rotations About the Booster Axes as used in the Booster Pitch, Roll and Yaw Plume Impingement Calculations

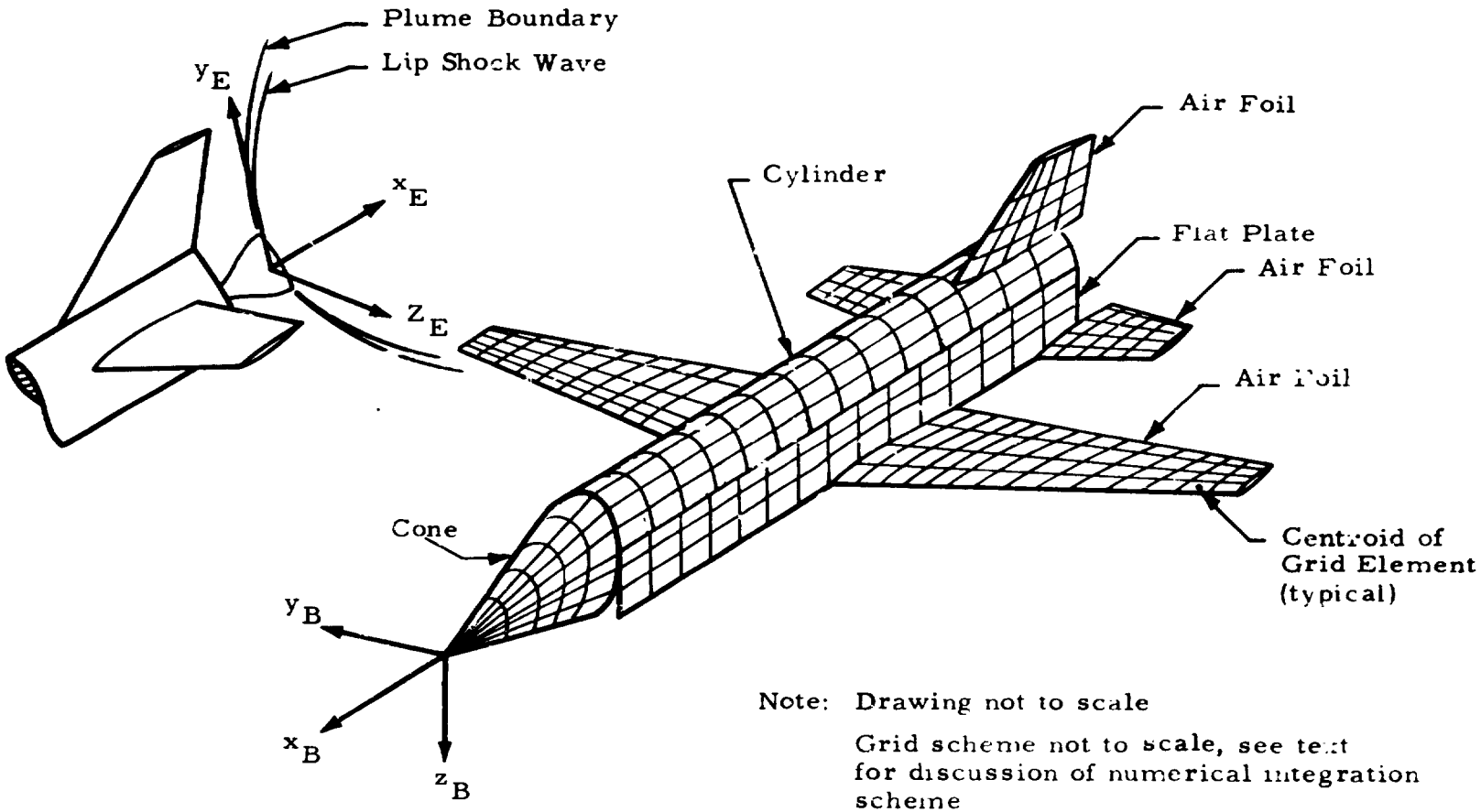

Note: Drawing not to scale

Grid scheme not to scale, see text for discussion of numerical integration scheme

The wing, horizontal and vertical tails are NACA airfoil 0012-64

Impingement data obtained at centroid of each grid element.

Fig. 2-14 - Sketch of Subshape System of Grid Scheme Used in the Force, Moment and Heating Analysis

FUSELAGE NOSE (CONE) SUBSHAPE

Subshape Information

Type: Cone (Conic)

Half Angle = 14.2 Degrees

Length = 760"

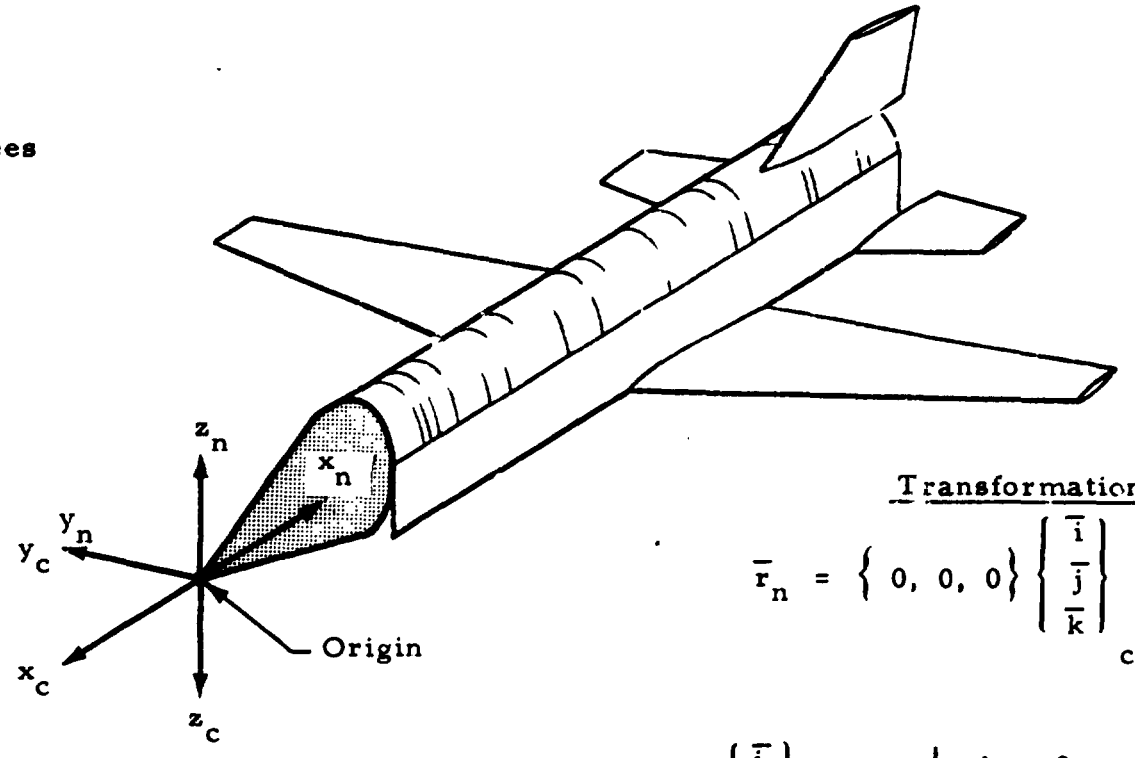

Transformation

$$\bar{r}_n = \left\{ 0,\ 0,\ 0 \right\} \left\{ \begin{matrix} \bar{i} \\ \bar{j} \\ \bar{k} \end{matrix} \right\}_c$$

$$\left\{ \begin{matrix} \bar{i} \\ \bar{j} \\ \bar{k} \end{matrix} \right\}_n = \begin{vmatrix} -1 & 0 & 0 \\ 0 & 1 & 0 \\ 0 & 0 & -1 \end{vmatrix} \left\{ \begin{matrix} \bar{i} \\ \bar{j} \\ \bar{k} \end{matrix} \right\}_c$$

Fig. 2-1e – Three-dimensional Perspective of the Conical Subshape Used to Represent the Booster Nose

Subshape Information

Type: Cylinder (Conic)

r = 192"

length = 1818"

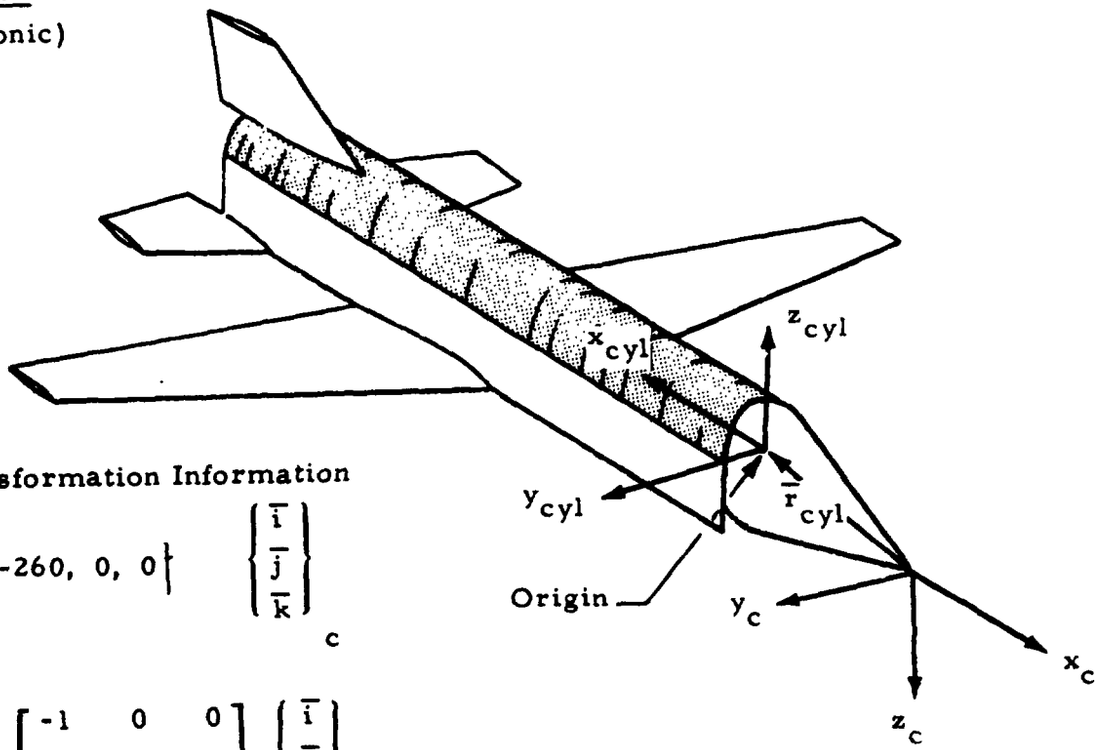

Transformation Information

$$\bar{r}_{cyl} = \begin{bmatrix} -260, & 0, & 0 \end{bmatrix} \begin{Bmatrix} \bar{i} \\ \bar{j} \\ \bar{k} \end{Bmatrix}_c$$

$$\begin{Bmatrix} \bar{i} \\ \bar{j} \\ \bar{k} \end{Bmatrix}_{cyl} = \begin{bmatrix} -1 & 0 & 0 \\ 0 & 1 & 0 \\ 0 & 0 & -1 \end{bmatrix} \begin{Bmatrix} \bar{i} \\ \bar{j} \\ \bar{k} \end{Bmatrix}_c$$

Fig. 2-1f – Three-Dimensional Perspective of the Cylindrical Section Used to Represent the Top of the Booster Fuselage.

RIGHT WING SUBSHAPE

Subshape Information

Type: Airfoil NACA 0012-64

Sweep Angle = 14°

Root Chord = 422"

Span = 930.5"

Taper Ratio = 0.396

Root Thickness = 50"

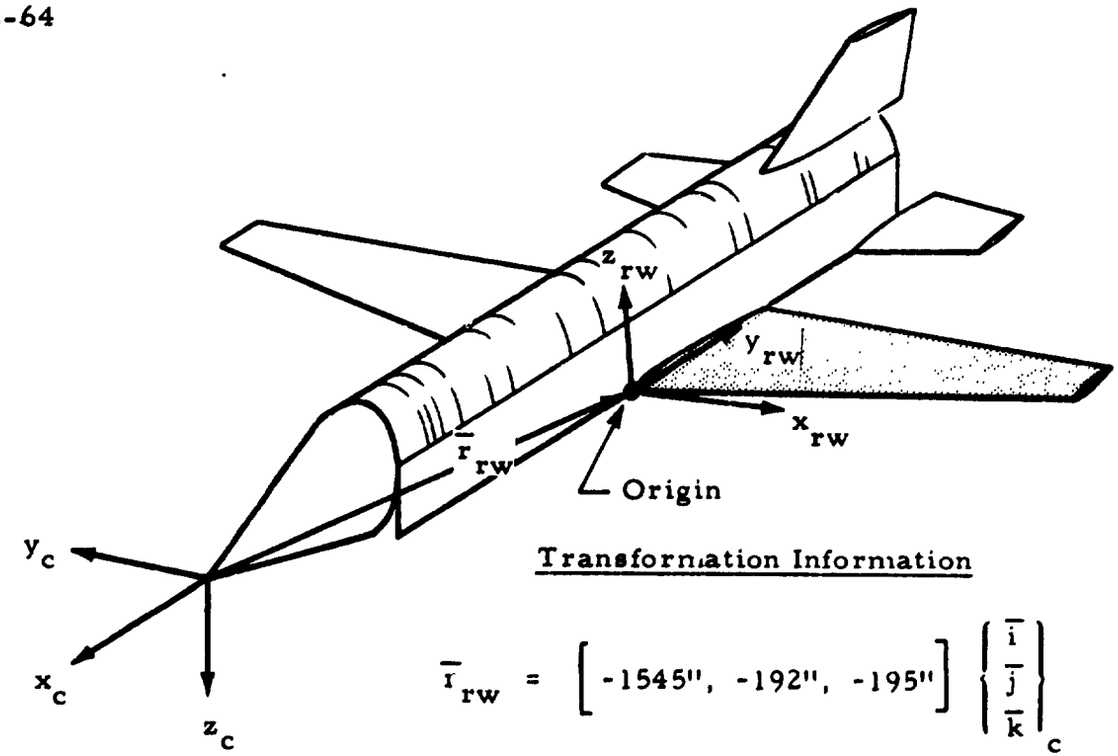

Transformation Information

$$\bar{r}_{rw} = \left[-1545", \ -192", \ -195" \right] \left\{ \begin{matrix} \bar{i} \\ \bar{j} \\ \bar{k} \end{matrix} \right\}_c$$

Wing Pitch (α) $\sim 2^\circ$; Dihedral (β) $\sim 7^\circ$

$$\left\{ \begin{matrix} \bar{i} \\ \bar{j} \\ \bar{k} \end{matrix} \right\}_{rw} = \begin{bmatrix} -\sin\alpha \sin\beta & \cos\beta & -\cos\alpha \sin\beta \\ -\cos\alpha & 0 & \sin\alpha \\ \sin\alpha \cos\beta & \sin\beta & \cos\alpha \cos\beta \end{bmatrix} \left\{ \begin{matrix} \bar{i} \\ \bar{j} \\ \bar{k} \end{matrix} \right\}_c$$

Fig. 2-1g – Three-Dimensional Perspective of the Booster Right Wing

Subshape Information

Type: Airfoil NACA 0012-64
Sweep Angle = 14°
Root Chord = 422"
Span = 930.5"
Taper Ratio = .396
Root Thickness = 50"

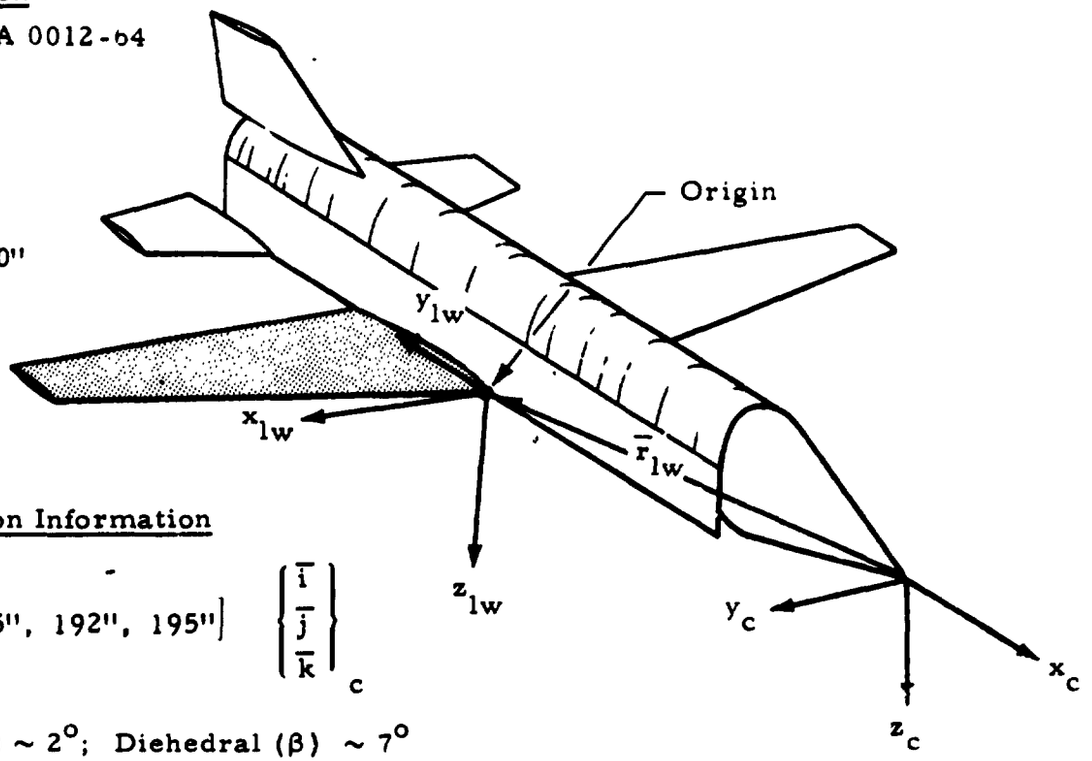

Transformation Information

$$\bar{r}_{lw} = \left[-1545", \ 192", \ 195"\right] \begin{Bmatrix} \bar{i} \\ \bar{j} \\ \bar{k} \end{Bmatrix}_c$$

Wing Pitch (α) ~ 2°; Diehedral (β) ~ 7°

$$\begin{Bmatrix} \bar{i} \\ \bar{j} \\ \bar{k} \end{Bmatrix}_{lw} = \begin{bmatrix} \sin\alpha \sin\beta & \cos\beta & -\cos\alpha \sin\beta \\ -\cos\alpha & 0 & \sin\alpha \\ \sin\alpha \cos\beta & \sin\beta & \cos\alpha \cos\beta \end{bmatrix} \begin{Bmatrix} \bar{i} \\ \bar{j} \\ \bar{k} \end{Bmatrix}_c$$

Fig. 2-1h — Three-Dimensional Perspective of the Booster Left Wing

Subshape Information

Type: Airfoil NACA 0012-64
Sweep Angle = 24°
Root Chord = 464.5"
Span = 444"
Taper Ratio = .461
Root Thickness = 40"

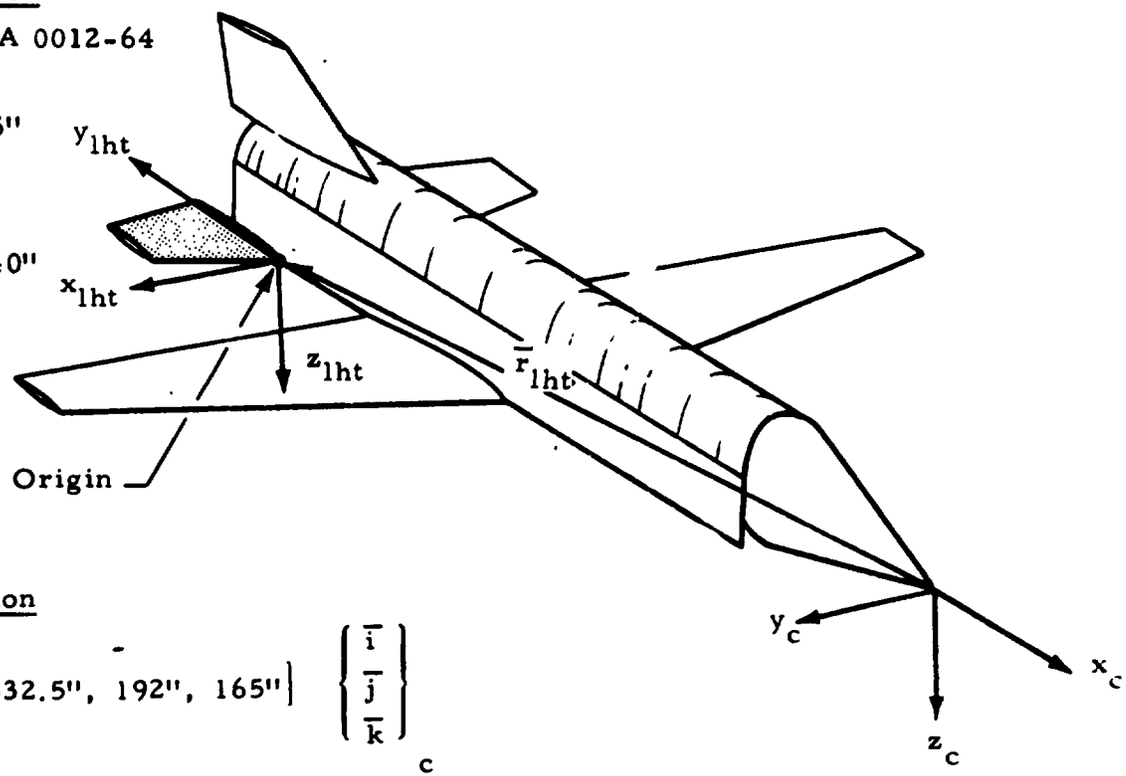

Transformation

$$\bar{r}_{lht} = \left|-2332.5",\ 192",\ 165"\right| \begin{Bmatrix} \bar{i} \\ \bar{j} \\ \bar{k} \end{Bmatrix}_c$$

$$\begin{Bmatrix} \bar{i} \\ \bar{j} \\ \bar{k} \end{Bmatrix}_{lht} = \begin{bmatrix} 0 & 1 & 0 \\ -1 & 0 & 0 \\ 0 & 0 & 1 \end{bmatrix} \begin{Bmatrix} \bar{i} \\ \bar{j} \\ \bar{k} \end{Bmatrix}_c$$

Fig. 2-1i — Three-Dimensional Perspective of the Booster Left Horizontal Tail

RIGHT HORIZONTAL TAIL

Subshape Information

Type: Airfoil NACA 0012-64
Sweep Angle = 24°
Root Chord = 464.5"
Span = 444"
Taper Ratio = .461
Root Thickness = 40"

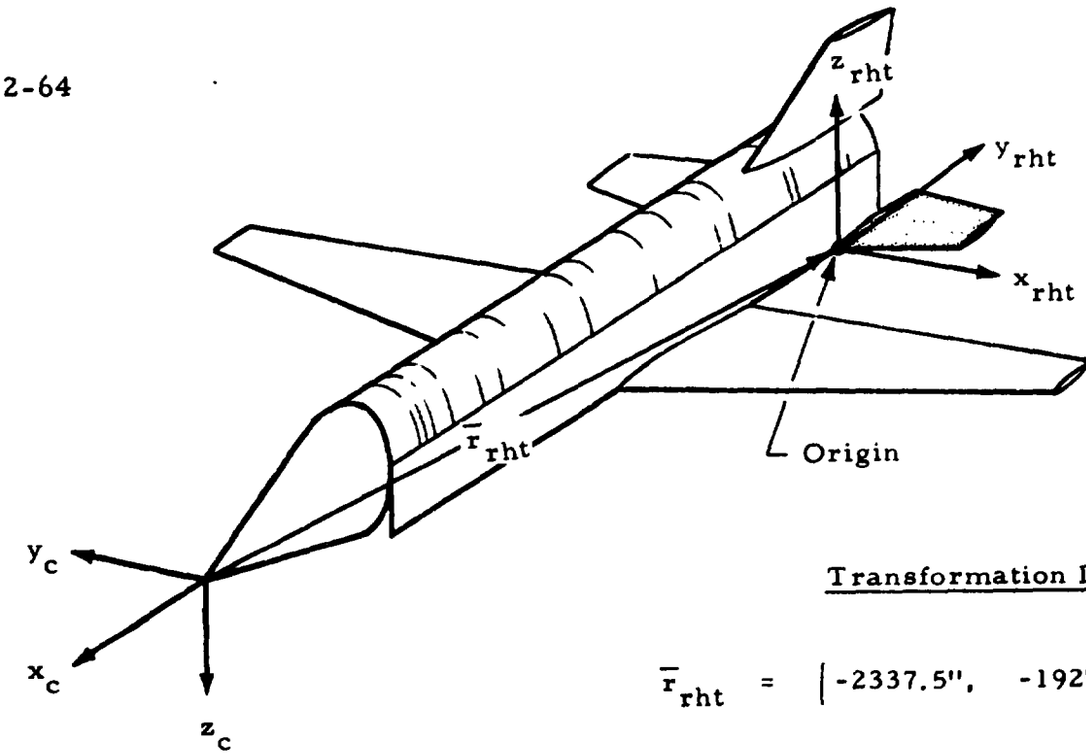

Transformation Information

$$\bar{r}_{rht} = \left| -2337.5",\ -192",\ 165" \right| \left\{ \begin{matrix} \bar{i} \\ \bar{j} \\ \bar{k} \end{matrix} \right\}_c$$

$$\left\{ \begin{matrix} \bar{i} \\ \bar{j} \\ \bar{k} \end{matrix} \right\}_{rht} = \begin{bmatrix} 0 & -1 & 0 \\ -1 & 0 & 0 \\ 0 & 0 & -1 \end{bmatrix} \left\{ \begin{matrix} \bar{i} \\ \bar{j} \\ \bar{k} \end{matrix} \right\}_c$$

Fig. 2-1j – Three-Dimensional Perspective of the Booster Right Horizontal Tail

VERTICAL TAIL SUBSHAPE

Subshape Information

Type: Airfoil NACA 0012-64

Sweep Angle = 45°

Root Chord = 526"

Taper = .456

S = 378"

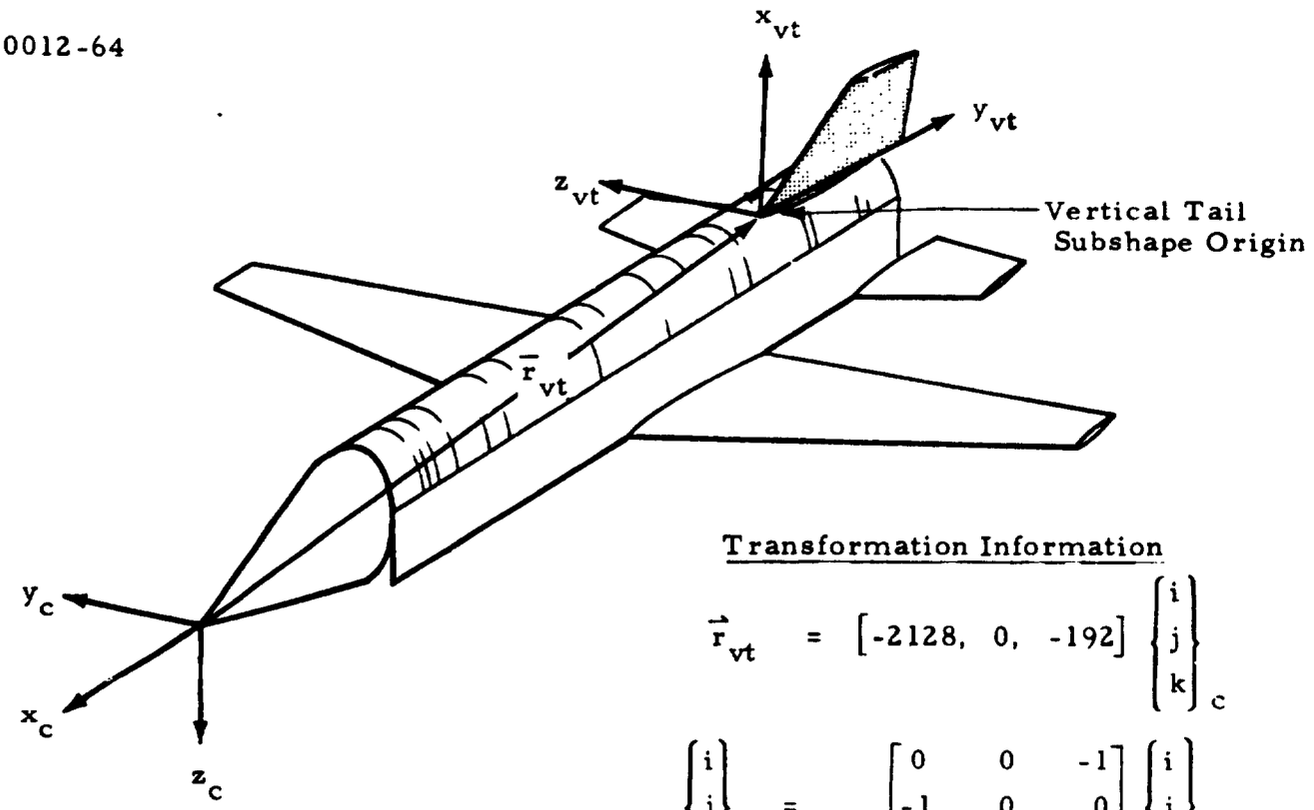

Transformation Information

$$\vec{r}_{vt} = \begin{bmatrix} -2128, & 0, & -192 \end{bmatrix} \begin{Bmatrix} i \\ j \\ k \end{Bmatrix}_c$$

$$\begin{Bmatrix} i \\ j \\ k \end{Bmatrix}_{vt} = \begin{bmatrix} 0 & 0 & -1 \\ -1 & 0 & 0 \\ 0 & 1 & 0 \end{bmatrix} \begin{Bmatrix} i \\ j \\ k \end{Bmatrix}_c$$

Fig. 2-1k – Three-Diminsional Perspective of the Booster Vertical Tail

FUSELAGE RIGHT SIDE SUBSHAPE

Subshape Information

Type: Flat Plate

Z = 1818", Y = 192"

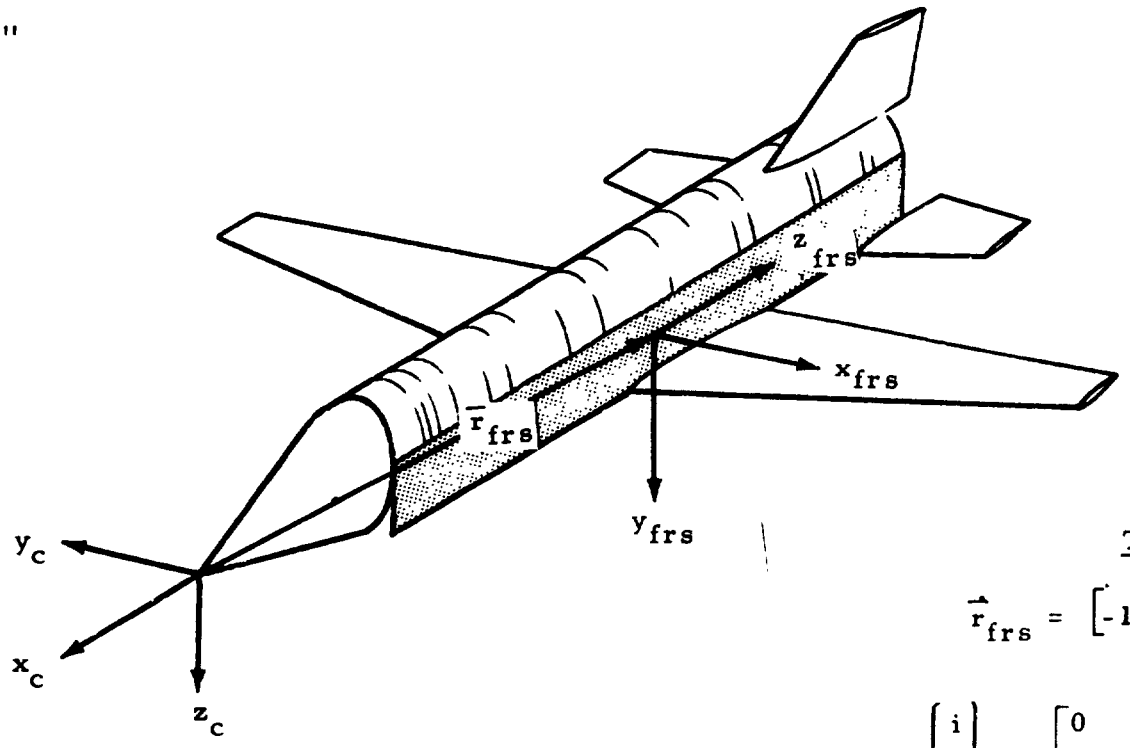

Transformation

$$\vec{r}_{frs} = \begin{bmatrix} -1669, & -192, & 96 \end{bmatrix} \begin{Bmatrix} i \\ j \\ k \end{Bmatrix}_c$$

$$\begin{Bmatrix} i \\ j \\ k \end{Bmatrix} = \begin{bmatrix} 0 & -1 & 0 \\ 0 & 0 & 1 \\ -1 & 0 & 0 \end{bmatrix} \begin{Bmatrix} i \\ j \\ k \end{Bmatrix}_c$$

Fig. 2-1ℓ – Three-Dimensional Perspective of the Subshape Used to Represent the Right Side of the Booster Fuselage

FUSELAGE LEFT SIDE SUBSHAPE

Subshape Information

Type: Flat Plate

Δz = 1818"

Δy = 192"

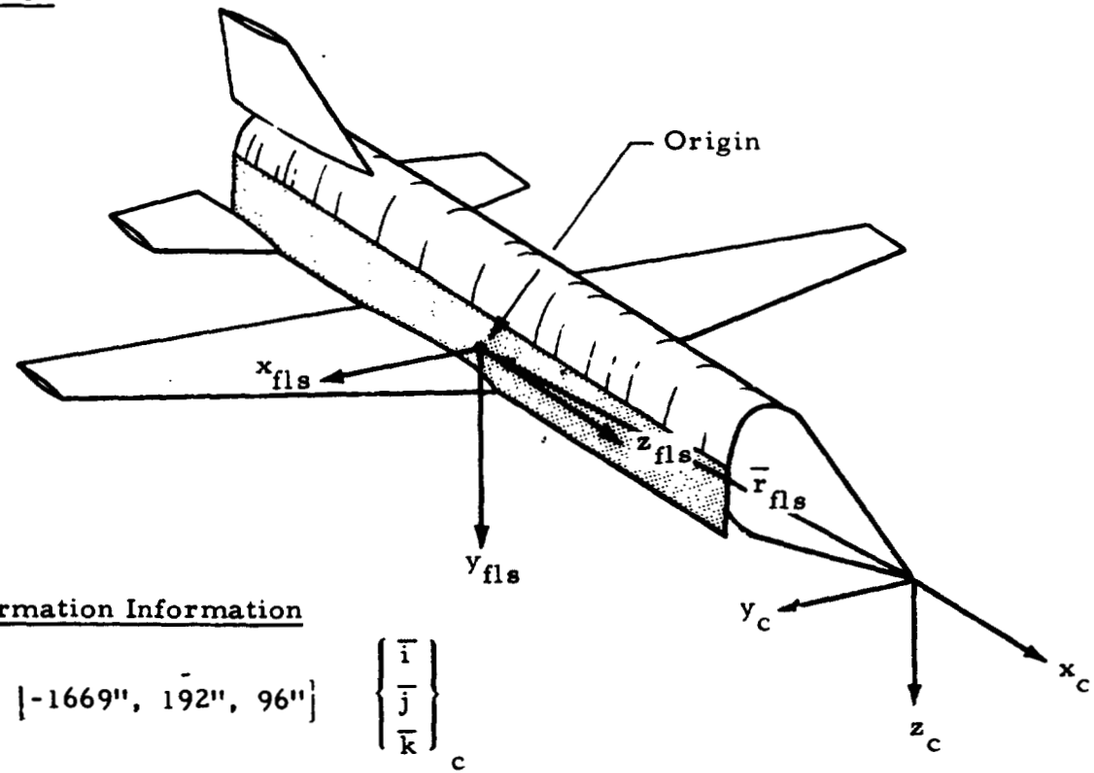

Transformation Information

$$\bar{r}_{fls} = \{-1669", 192", 96"\} \begin{Bmatrix} \bar{i} \\ \bar{j} \\ \bar{k} \end{Bmatrix}_c$$

$$\begin{Bmatrix} \bar{i} \\ \bar{j} \\ \bar{k} \end{Bmatrix}_{fls} = \begin{bmatrix} 0 & 1 & 0 \\ 0 & 0 & 1 \\ 1 & 0 & 0 \end{bmatrix} \begin{Bmatrix} \bar{i} \\ \bar{j} \\ \bar{k} \end{Bmatrix}_c$$

Fig. 2-1m – Three-Dimensional Perspective of the Subshape Used to Represent the Left Side of the Booster Fuselage

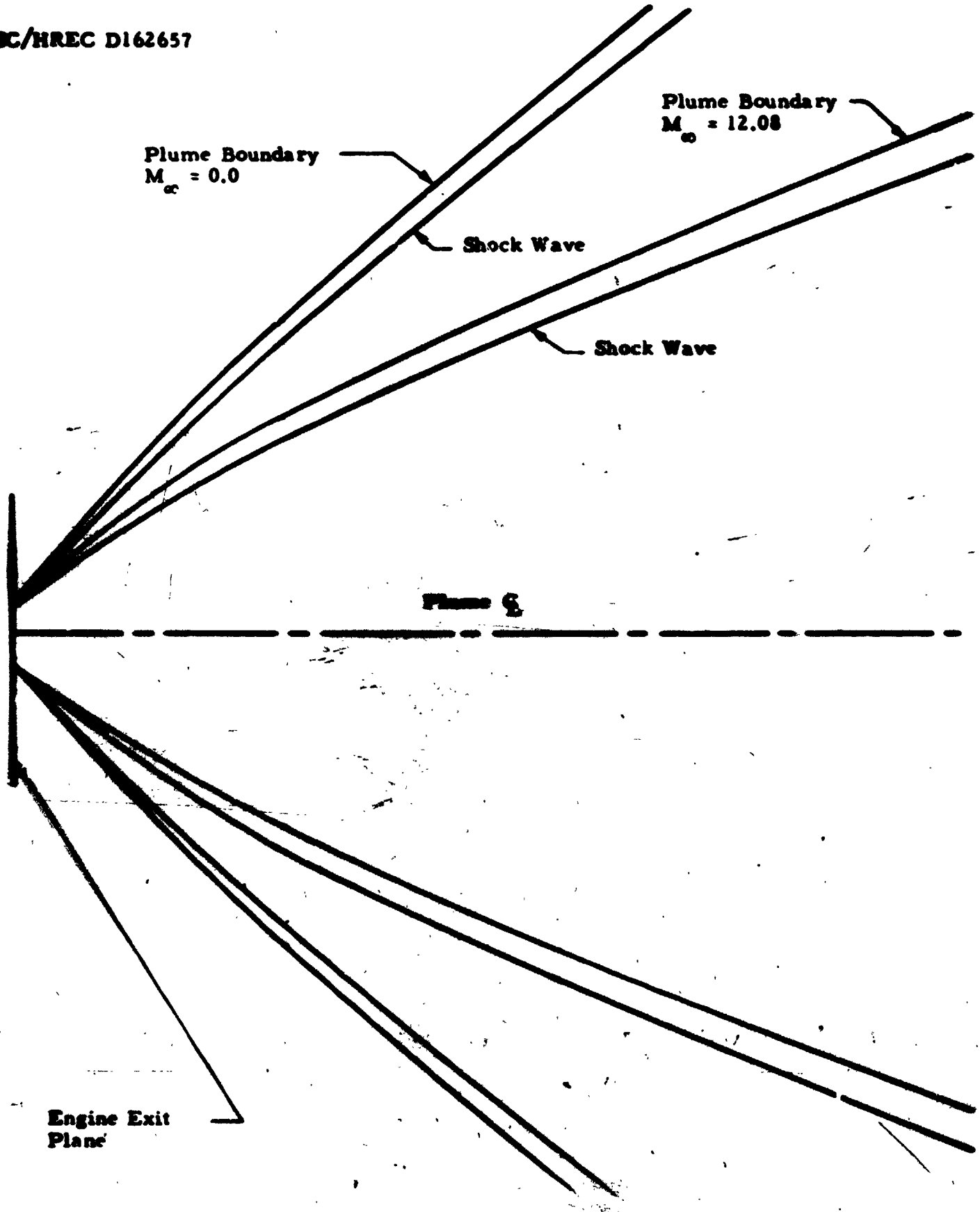

PRECEDING PAGE BLANK NOT FILMED

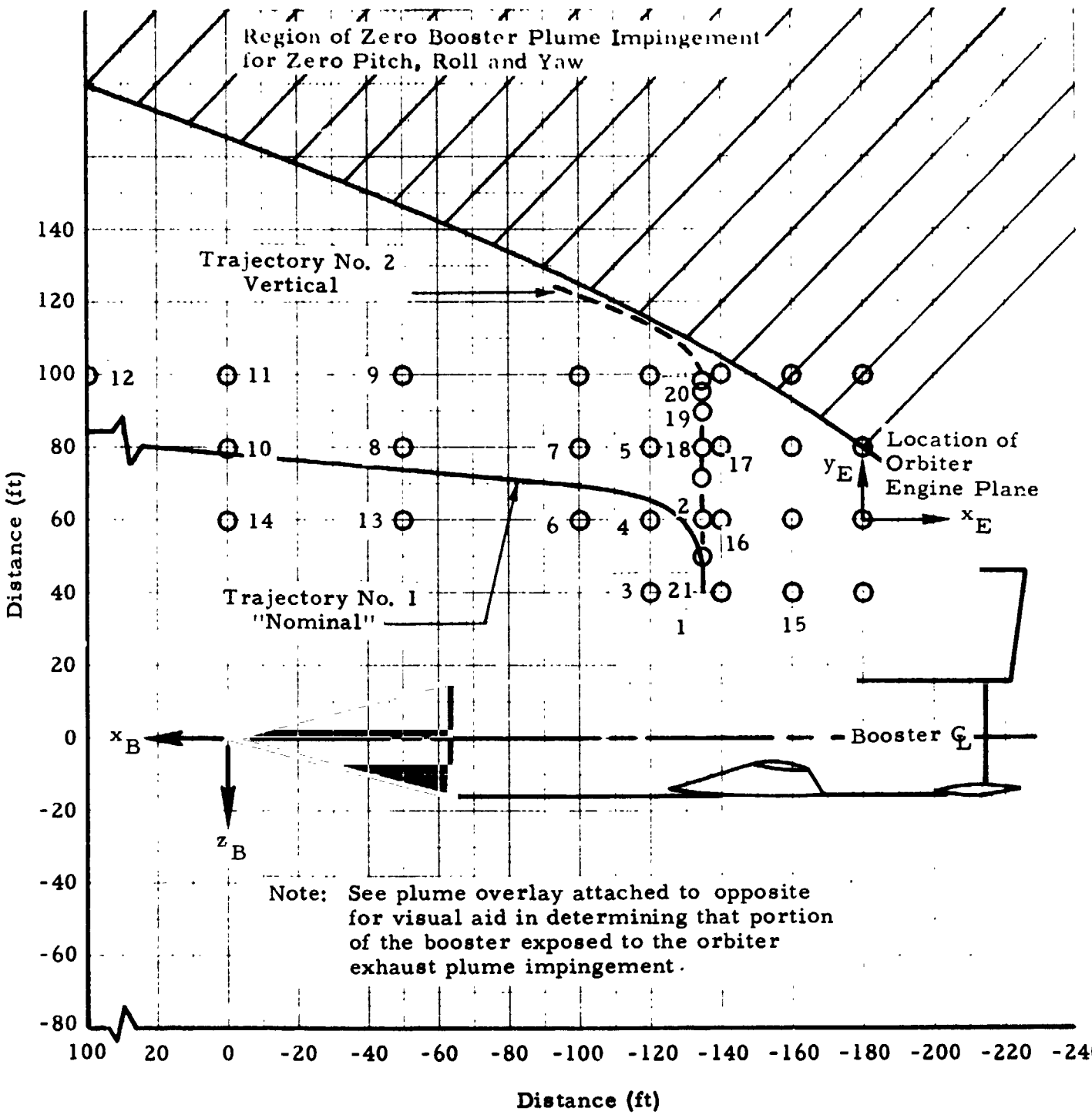

Fig. 2.1-n - Graphic Representation of Data Points Used to Calculate the Booster Plume Impingement Data with Separation Distance Between the Orbiter and Booster Vehicles

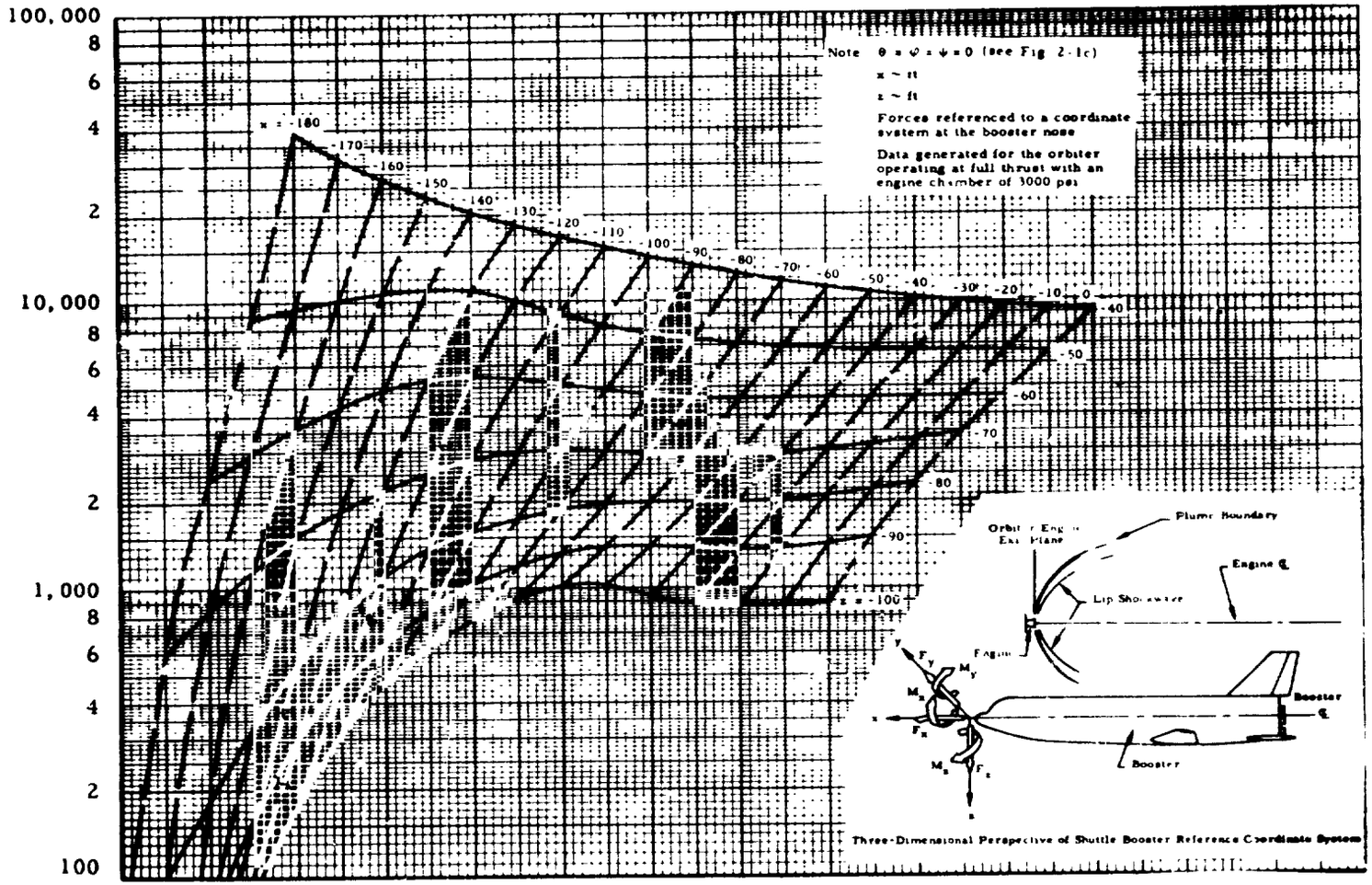

Fig. 2-2 -- Variation in the Booster Force Due to Orbiter Exhaust Plume Impingement with Orbiter Separation Distance from the Booster

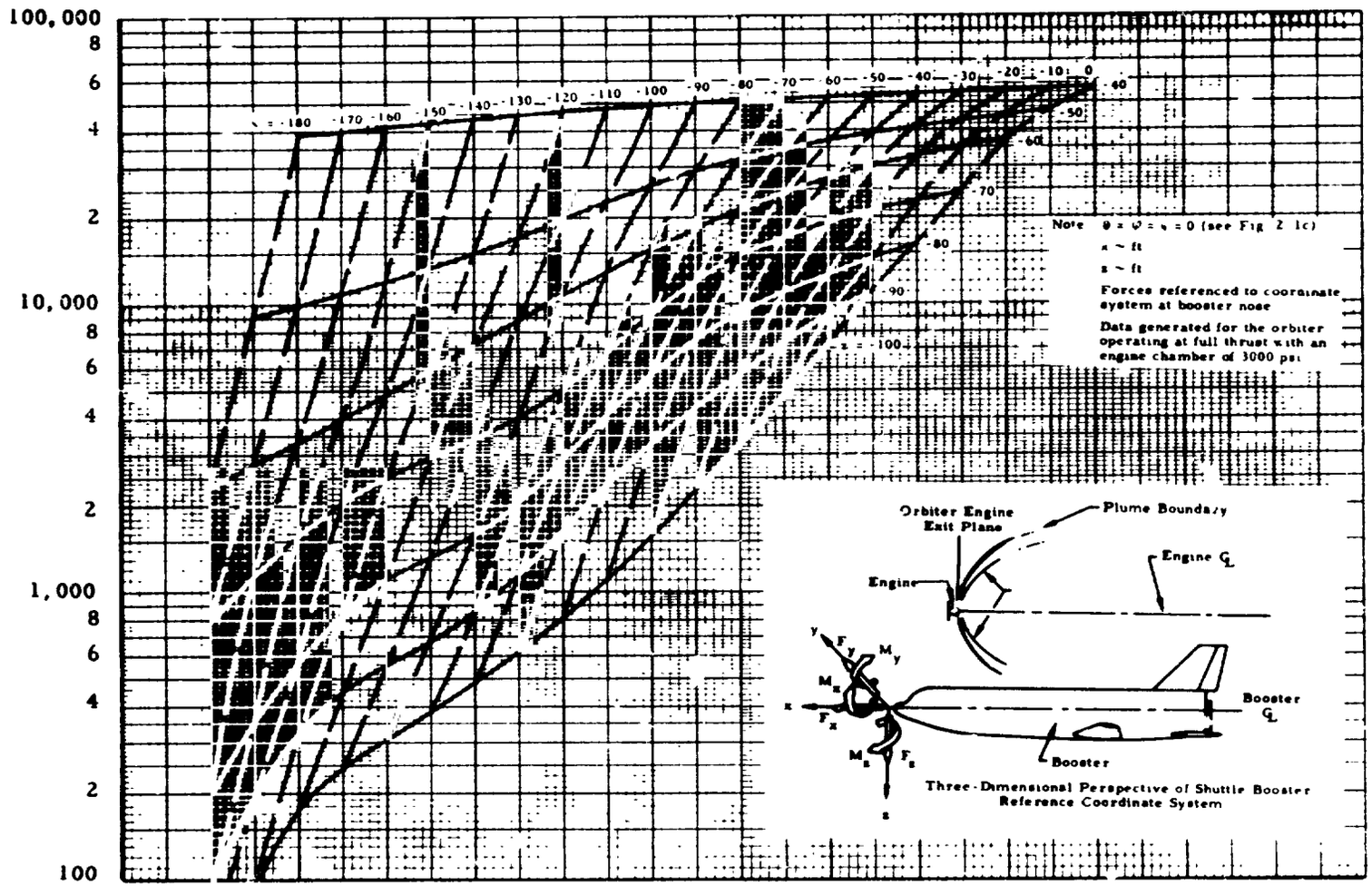

Fig. 2-3 Variation of the Booster Force Due to Orbiter Exhaust Plume Impingement with Orbiter Separation Distance from the Booster

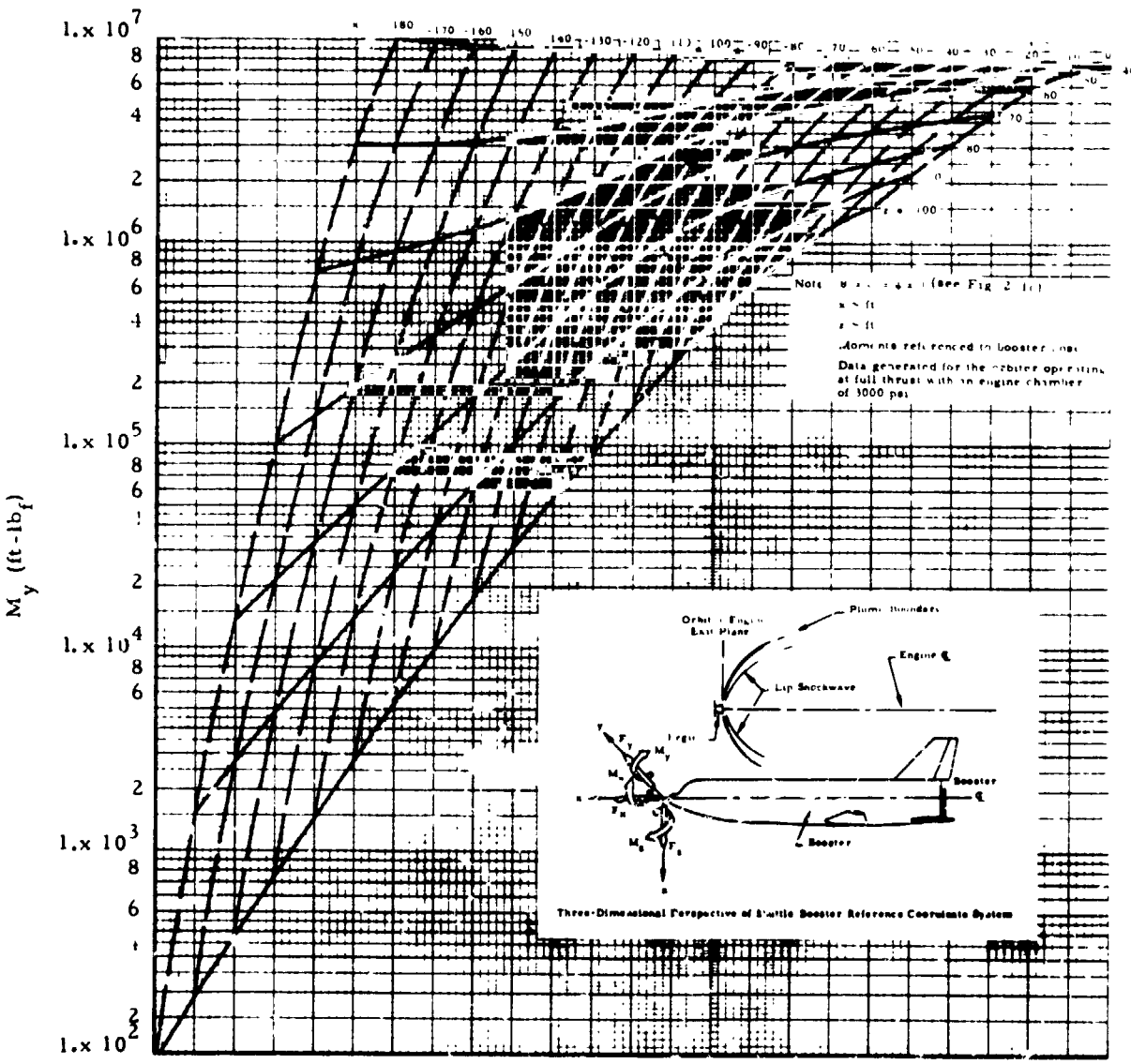

Fig. 2-4 – Variation of the Booster Moment due to the Orbiter Exhaust Plume Impingement with Orbiter Separation from the Booster

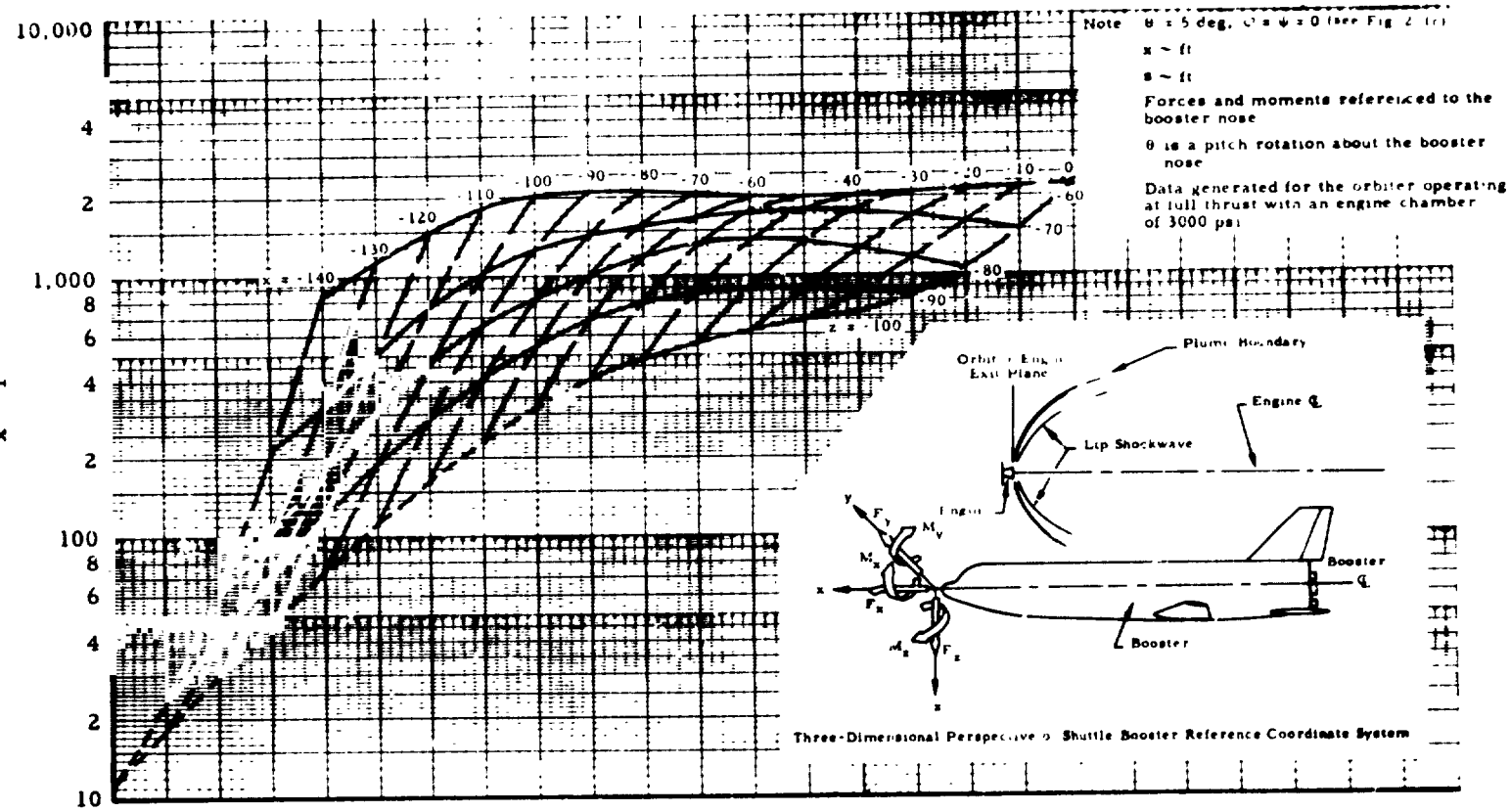

Fig. 2-5 – Variation of the Booster Plume Impingement Force with Orbiter Separation Distance from the Booster

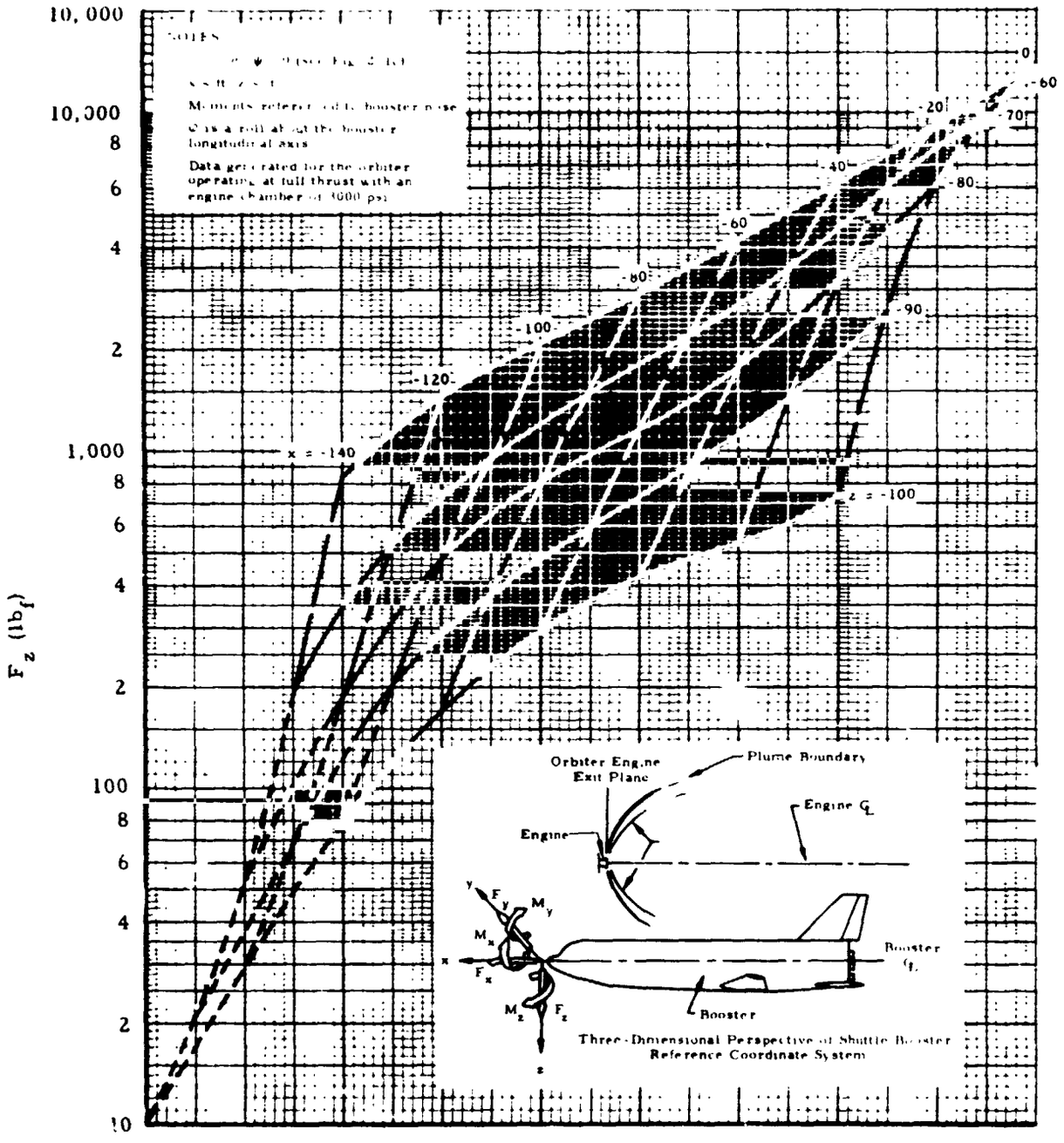

Fig. 2-6 – Variation of the Booster Force due to Orbiter Exhaust Plume Impingement with Orbiter Separation Distance from the Booster

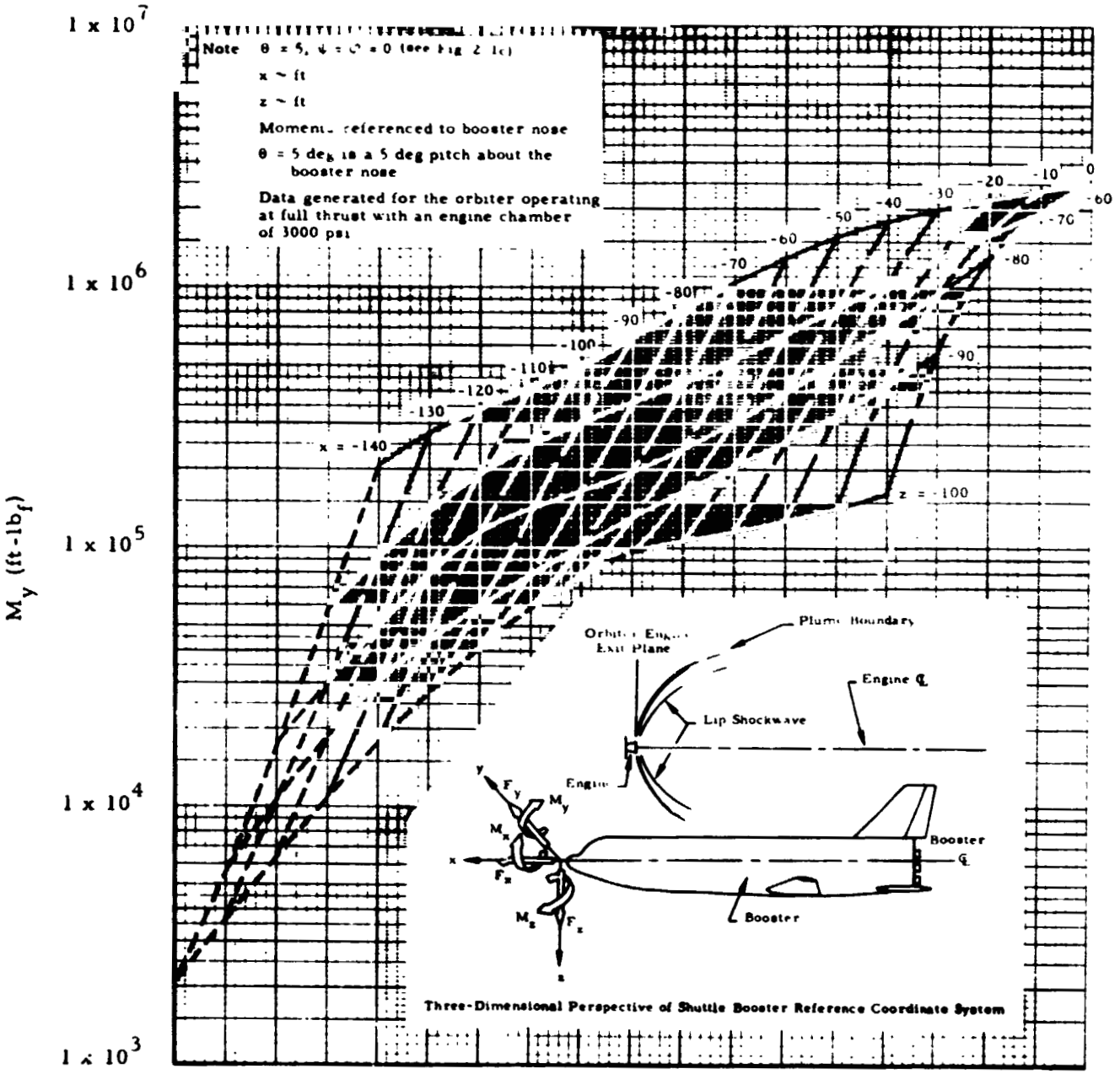

Fig. 2-7 – Variation of the Booster Moment, due to the Orbiter Exhaust Plume Impingement with Orbiter Separation Distance from the Booster

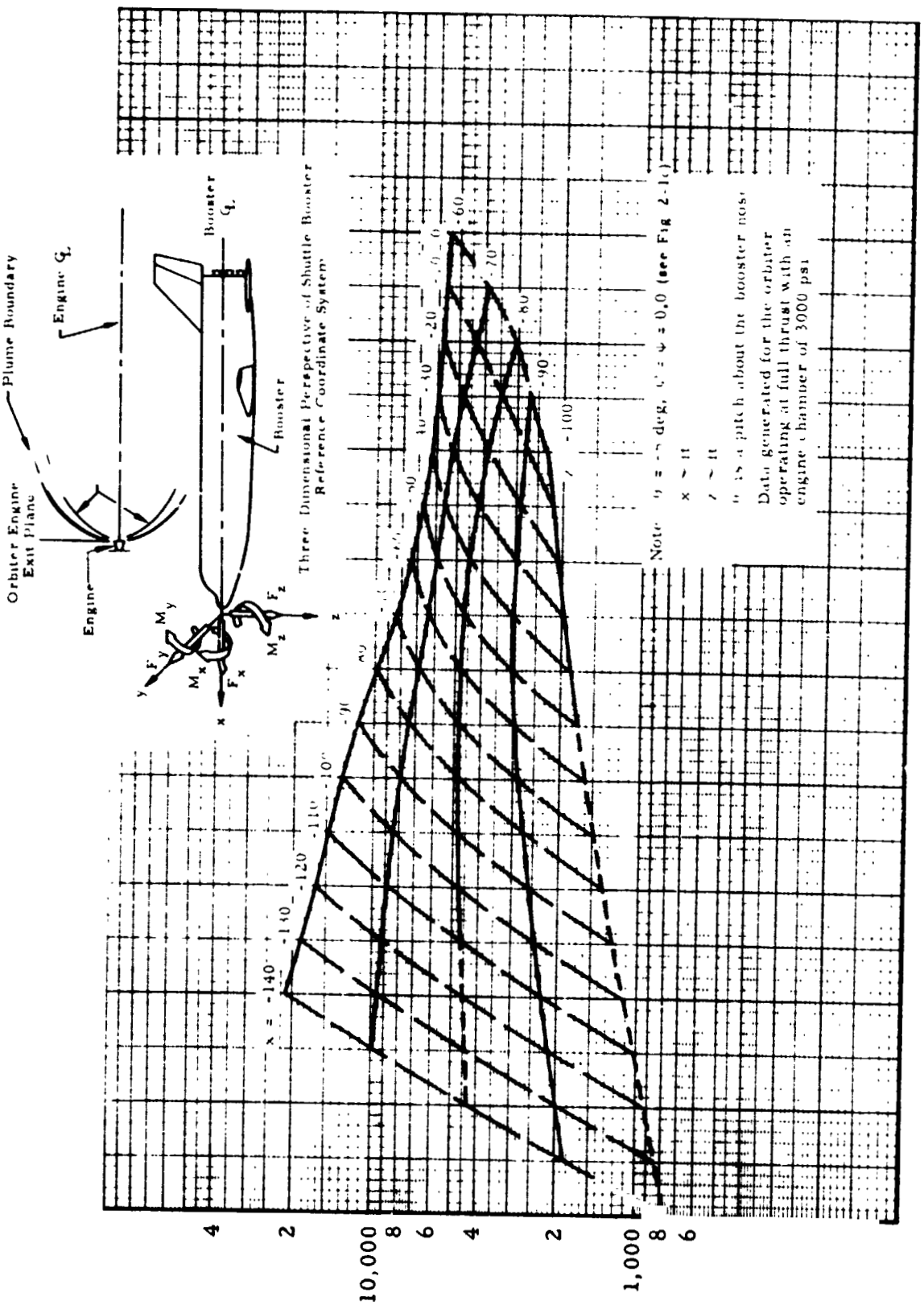

Fig. 2-8 – Variation of the Booster Plume Impingement Force with Orbiter Separation Distance from the Booster

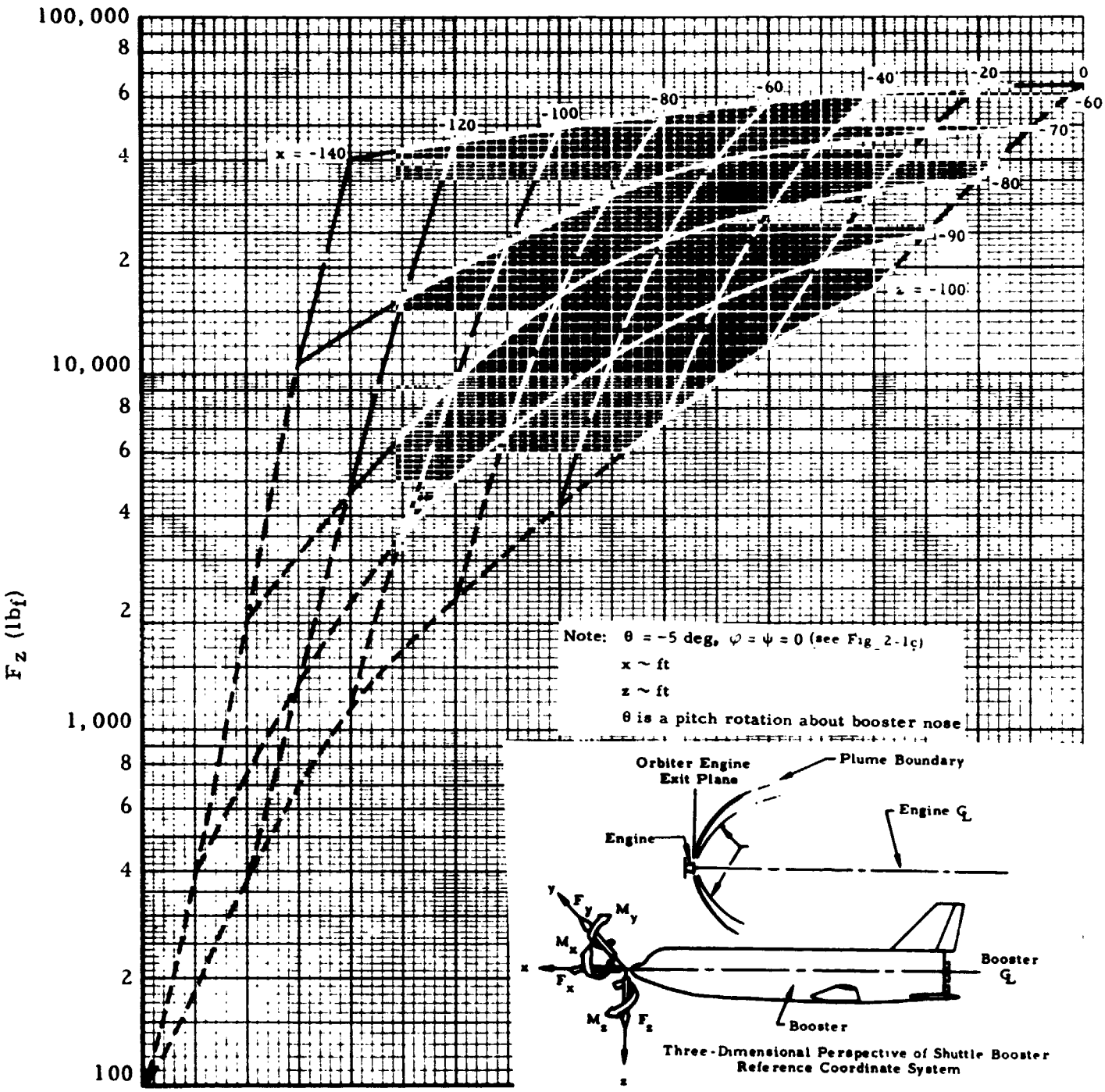

Fig. 2-9 — Variation of the Booster Plume Impingement Force with Orbiter Separation Distance from the Booster

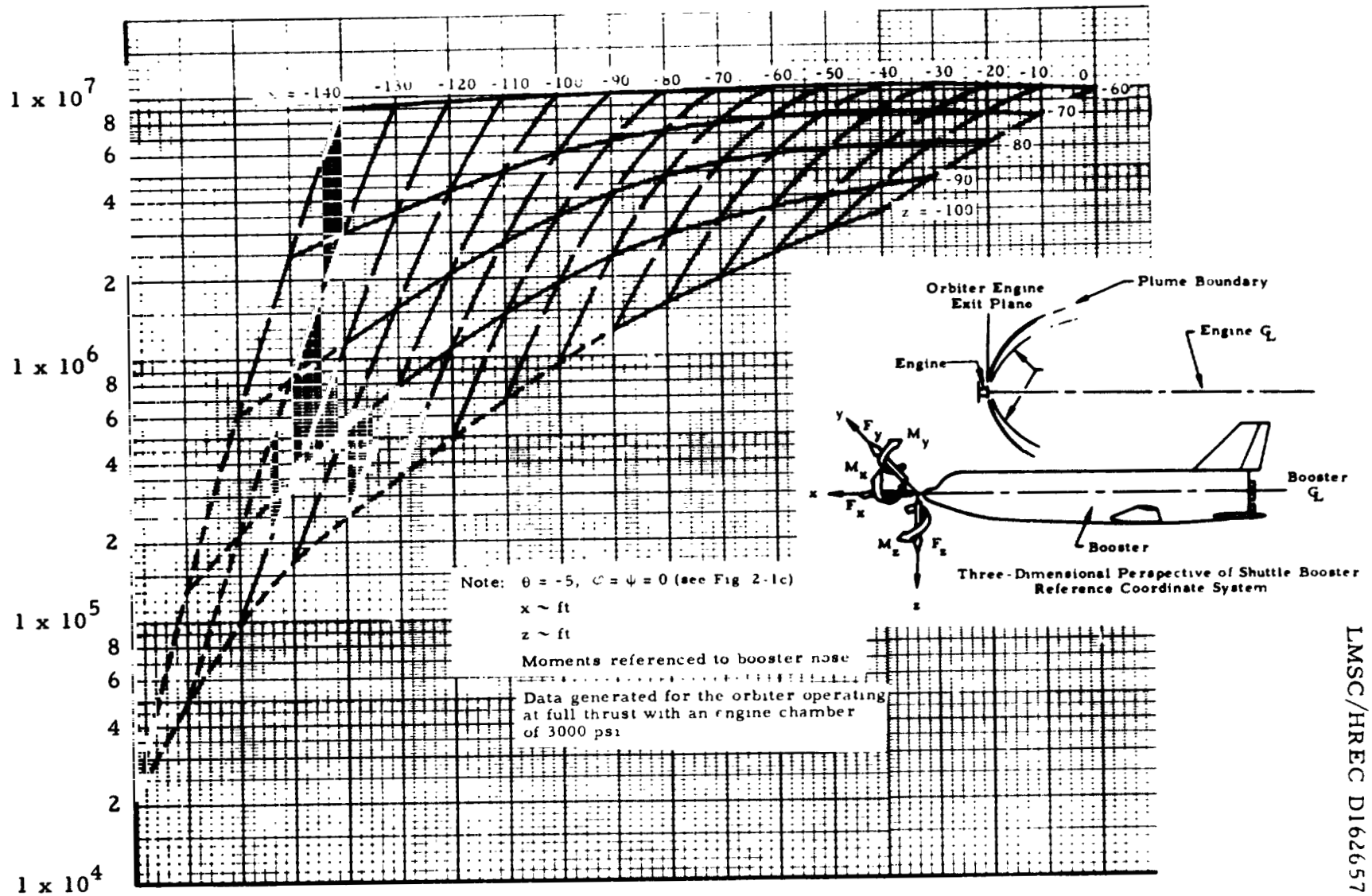

Fig. 2-10 – Variation of the Moment due to Booster Plume Impingement with Orbiter Separation Distance from the Booster

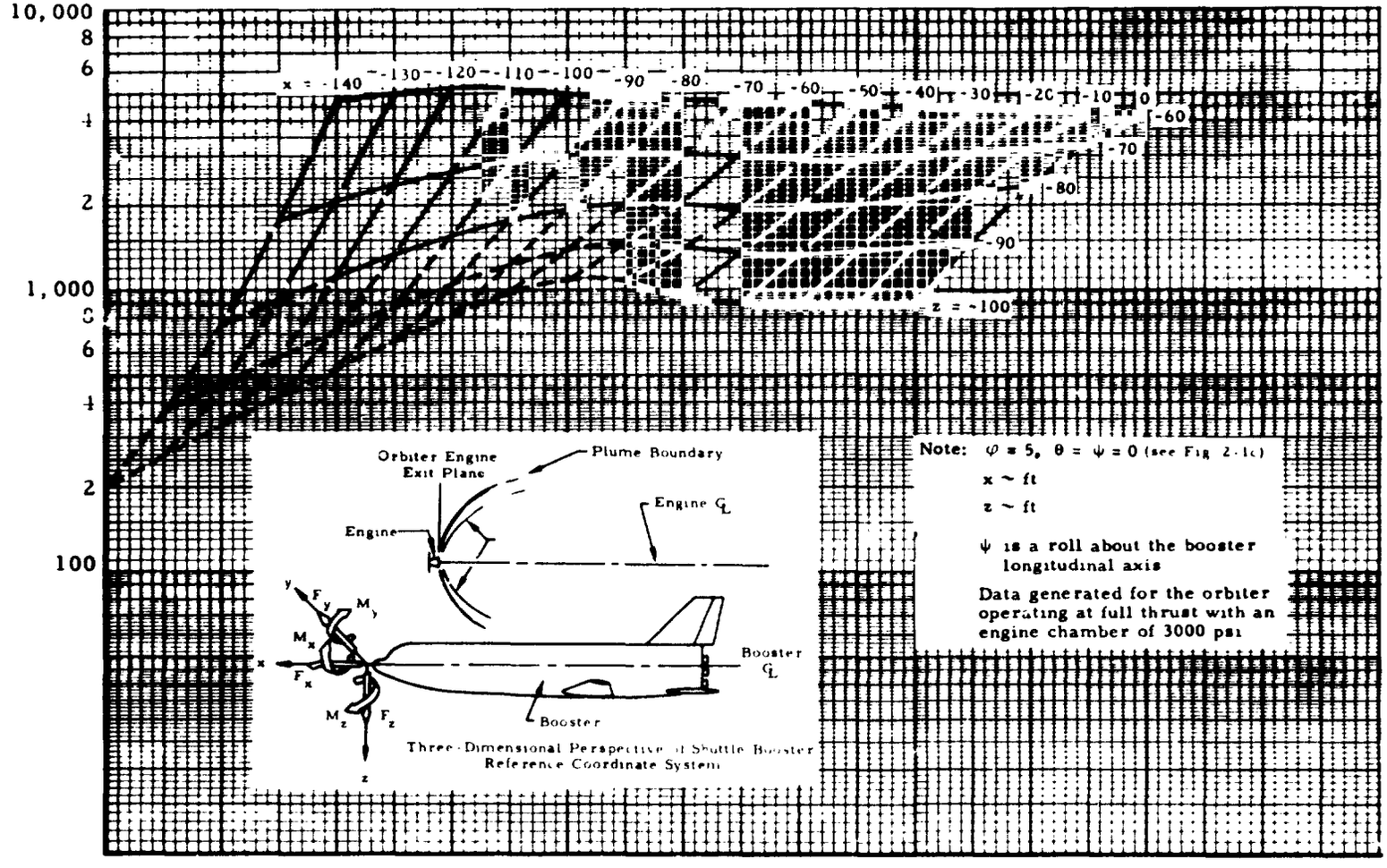

Fig. 2-11 – Variation of the Booster Plume Impingement Force with Orbiter Separation Distance from the Booster

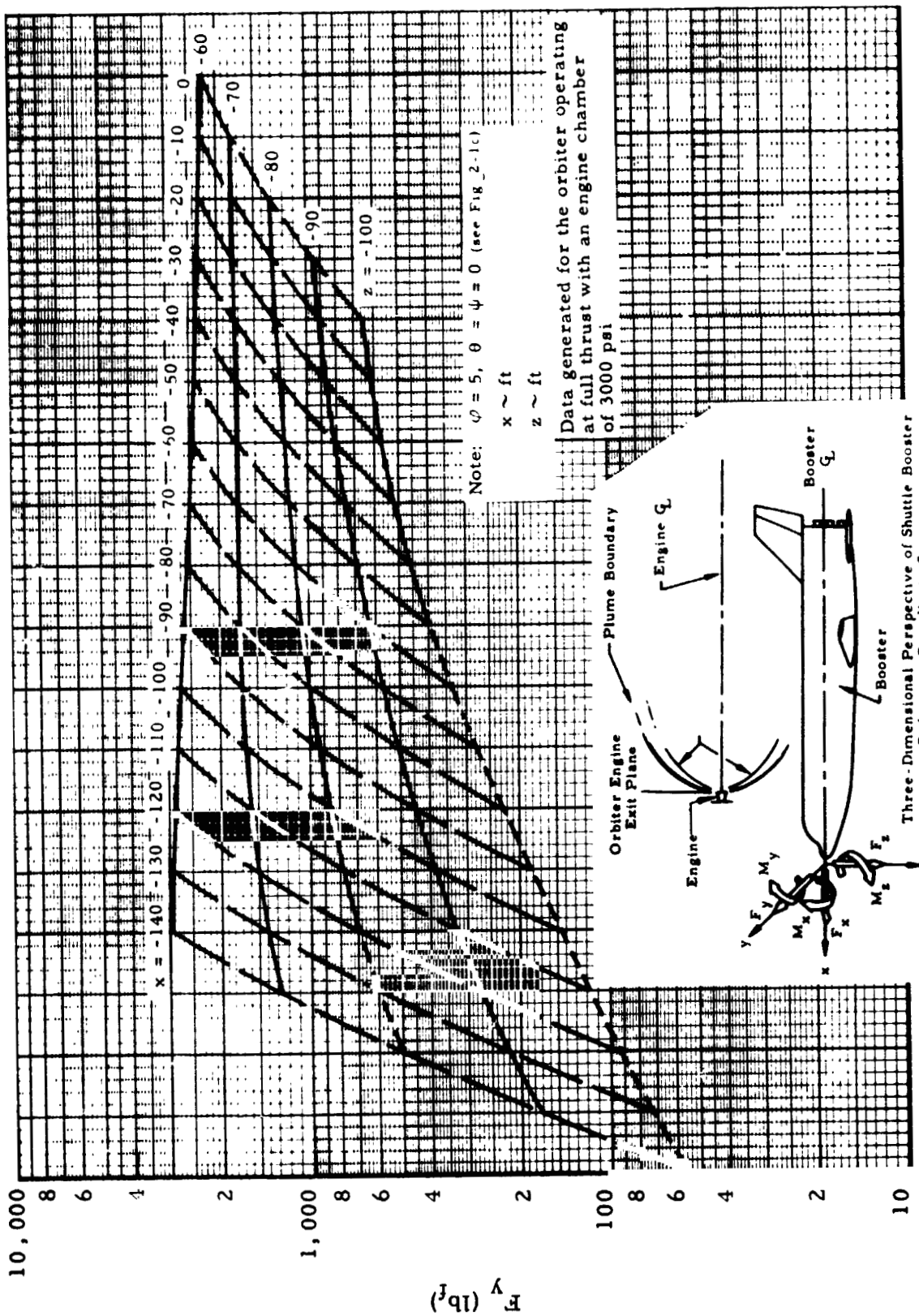

Fig. 2-12 — Variation of the Booster Plume Impingement Force with Separation Distance from the Booster

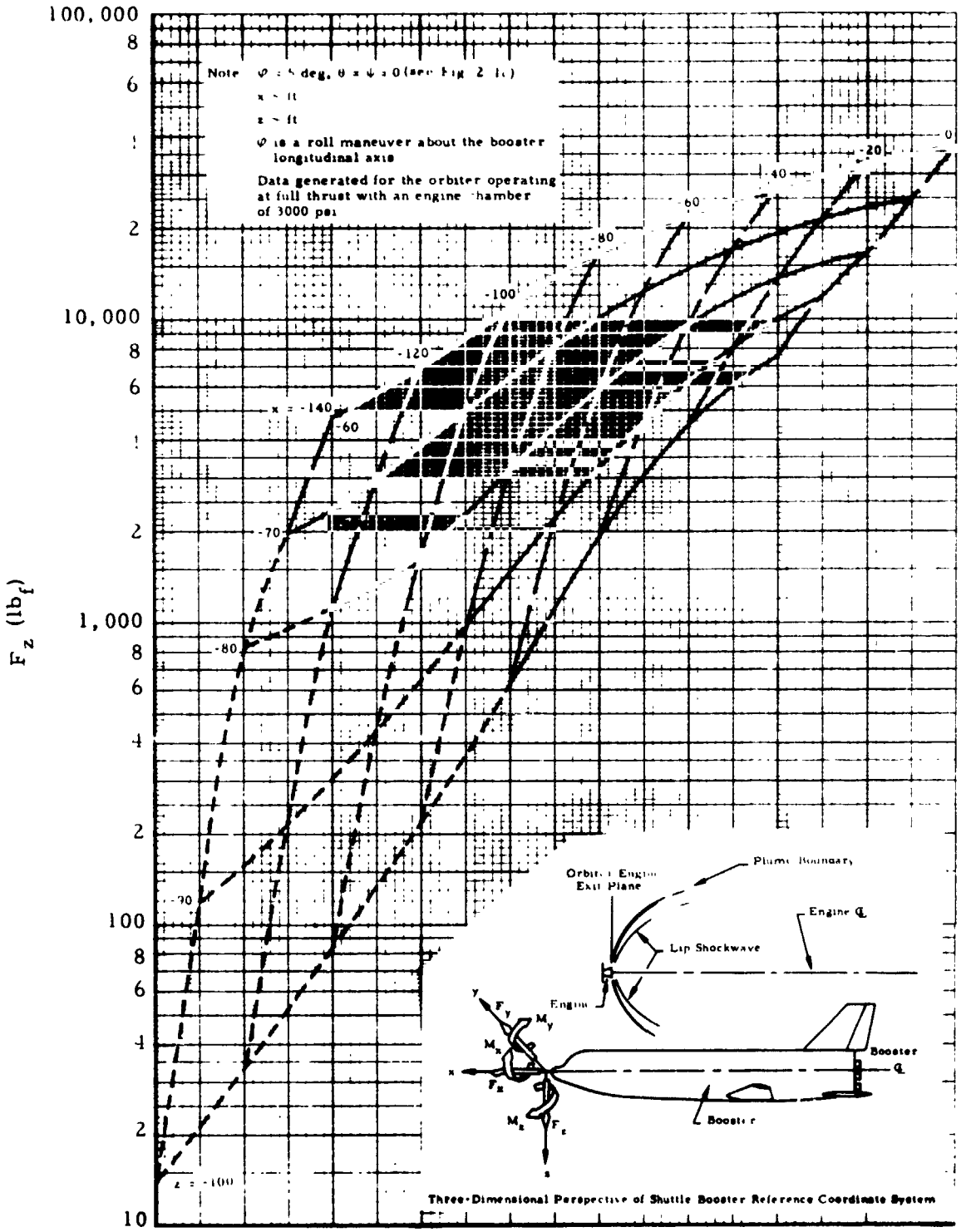

Fig. 2-13 – Variation in the Booster Force due to Orbiter Exhaust Plume Impingement with Orbiter Separation Distance from the Booster

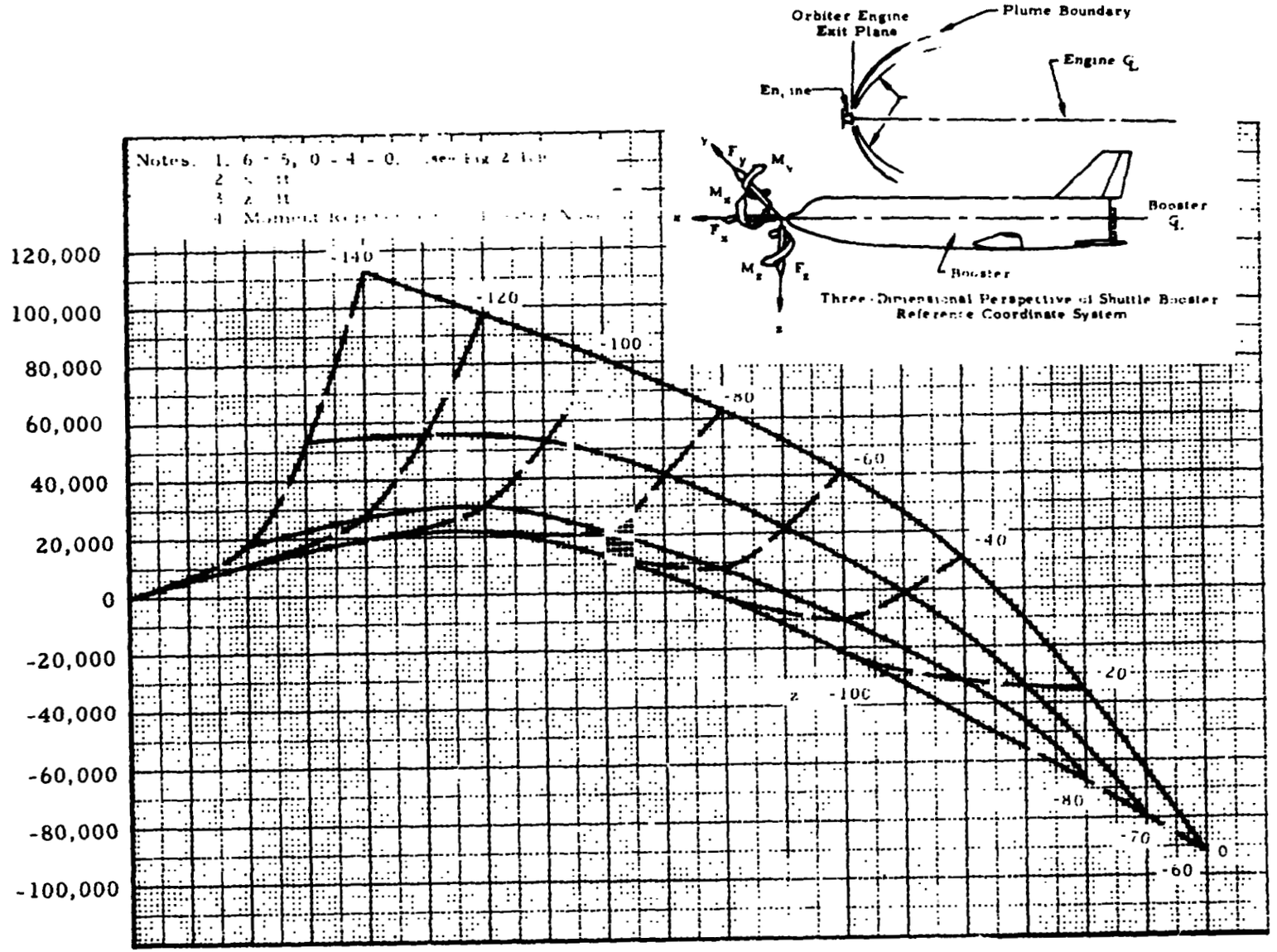

Fig. 2-14 — Variation of Booster Roll Moment due Orbiter Exhaust Plume Impingement with Orbiter Separation Distance from the Booster

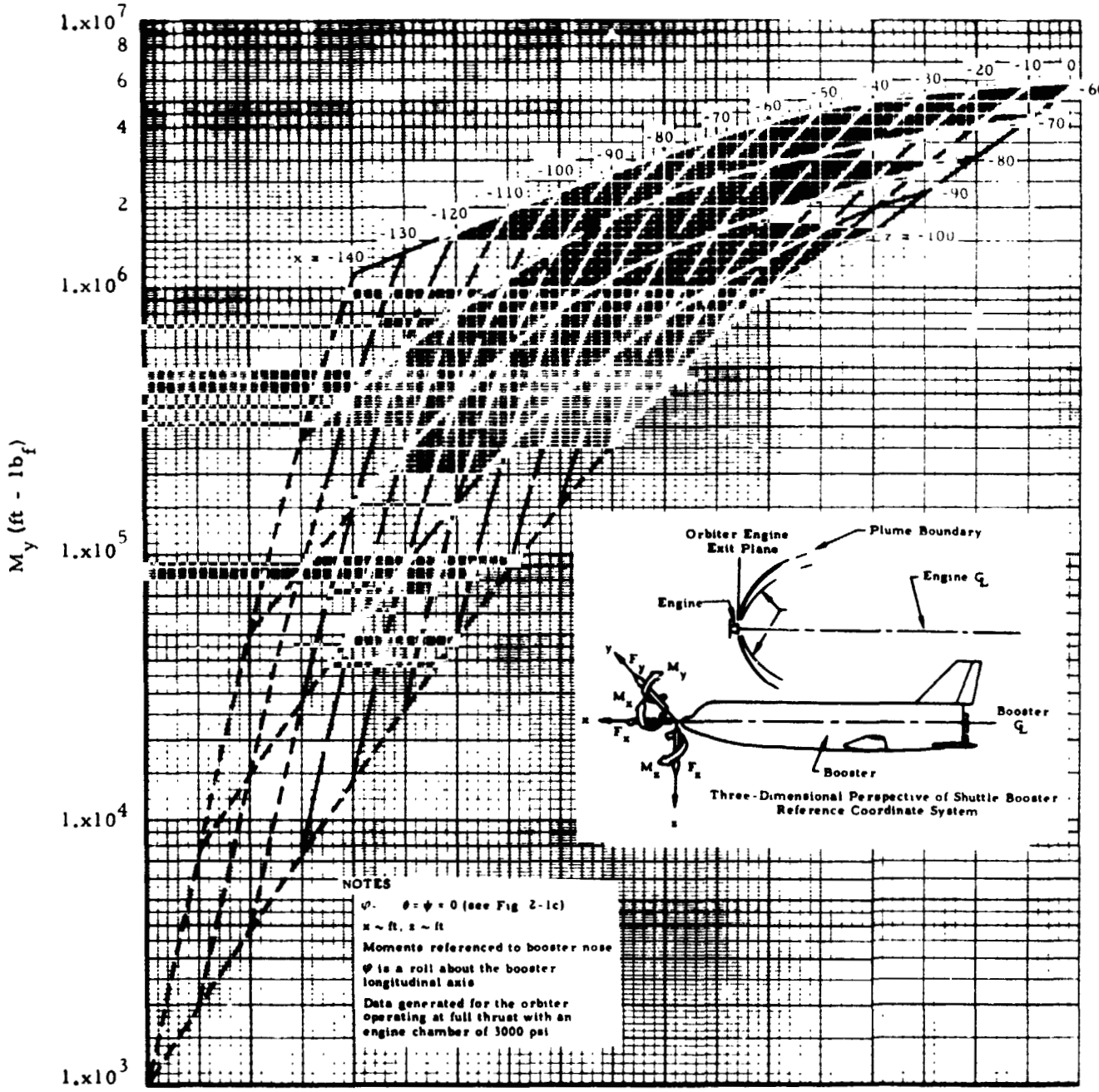

Fig. 2-15 – Variation of the Booster Moment due to Plume Impingement with Separation Distance of the Orbiter from the Booster

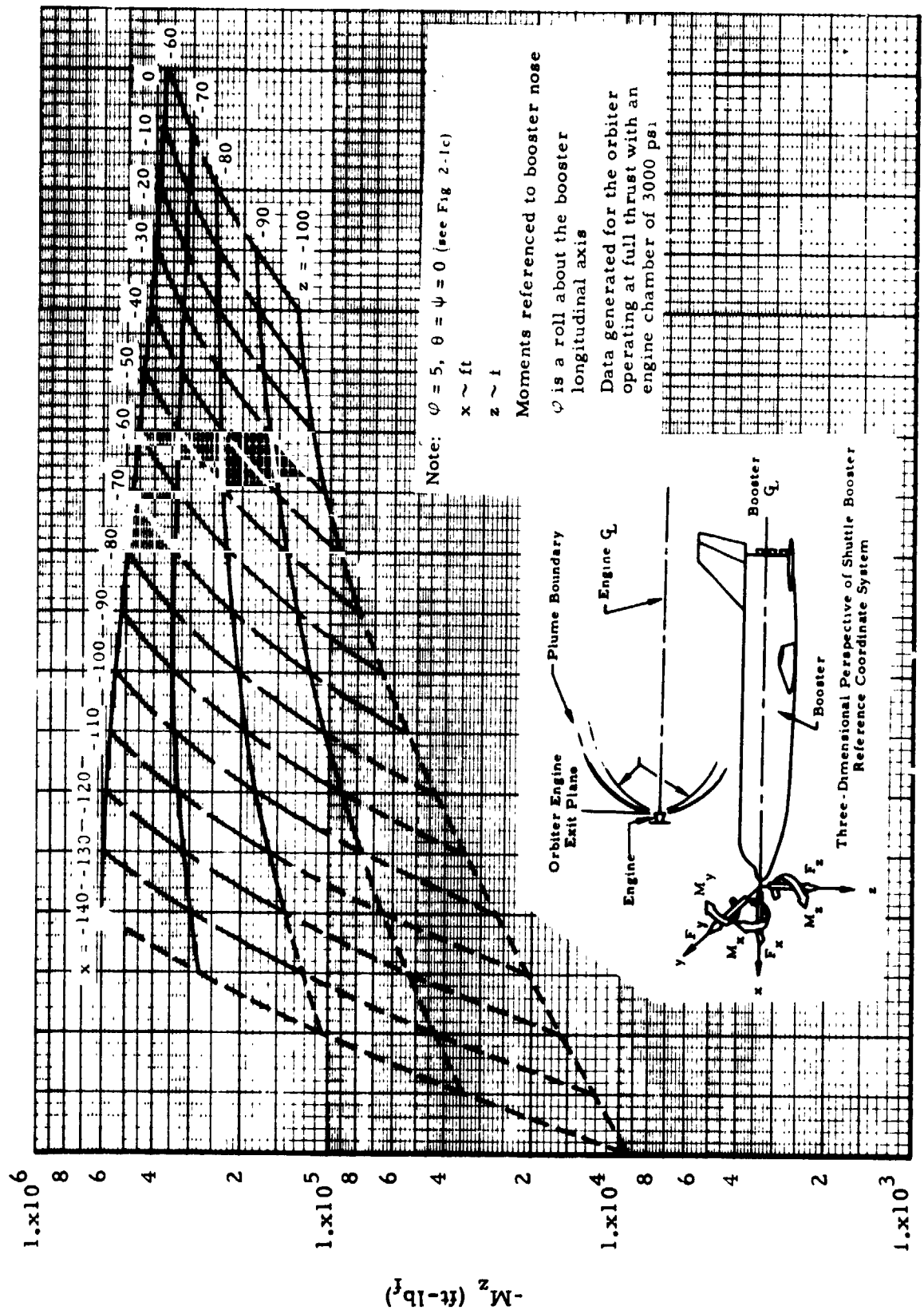

Fig. 2-16 — Variation of the Booster Plume Impingement Moment with the Orbiter Separation Distance from the Booster

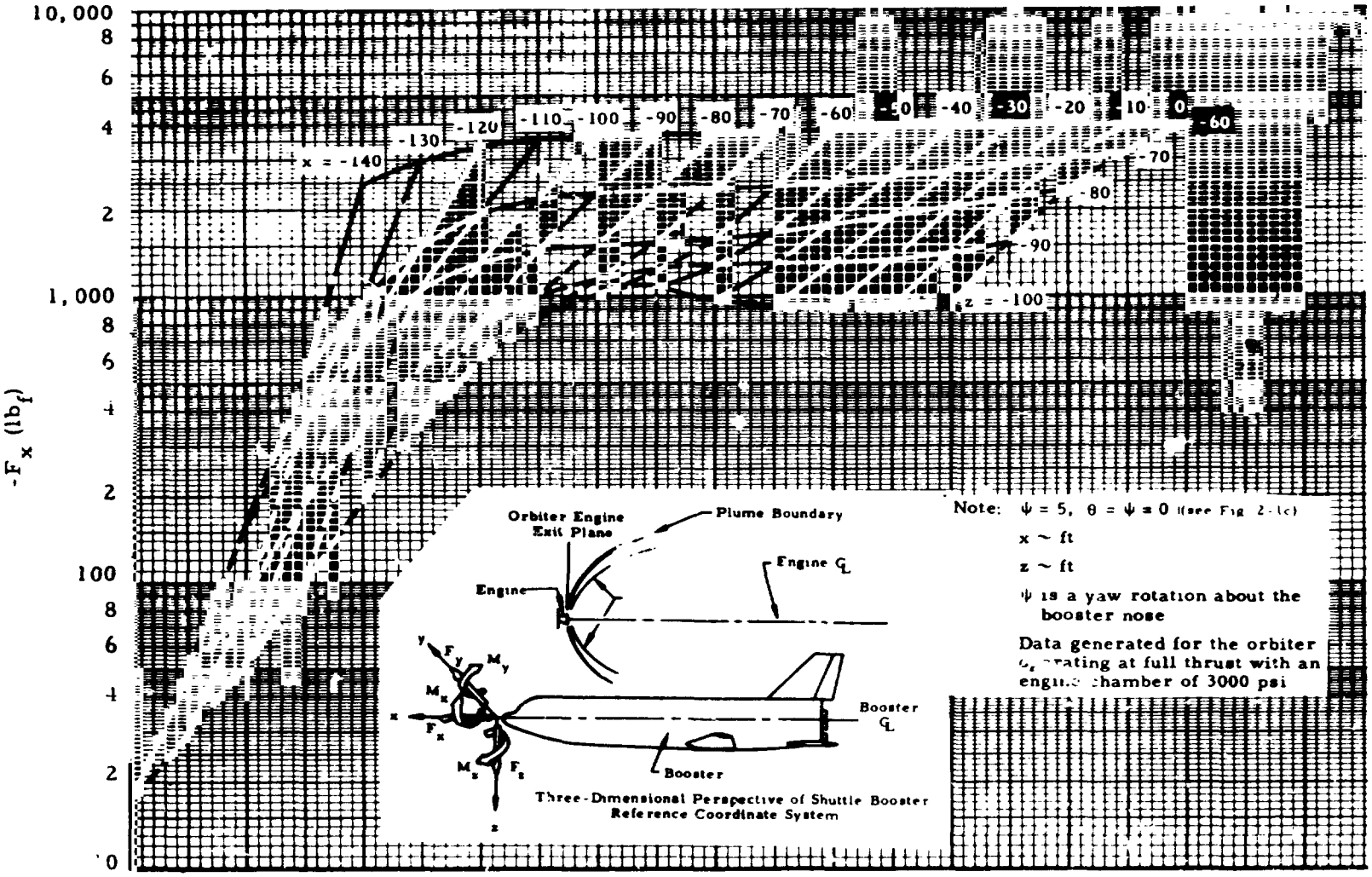

Fig. 2-17 – Variation of the Booster Plume Impingement Force with Separation Distance of the Orbiter from the Booster

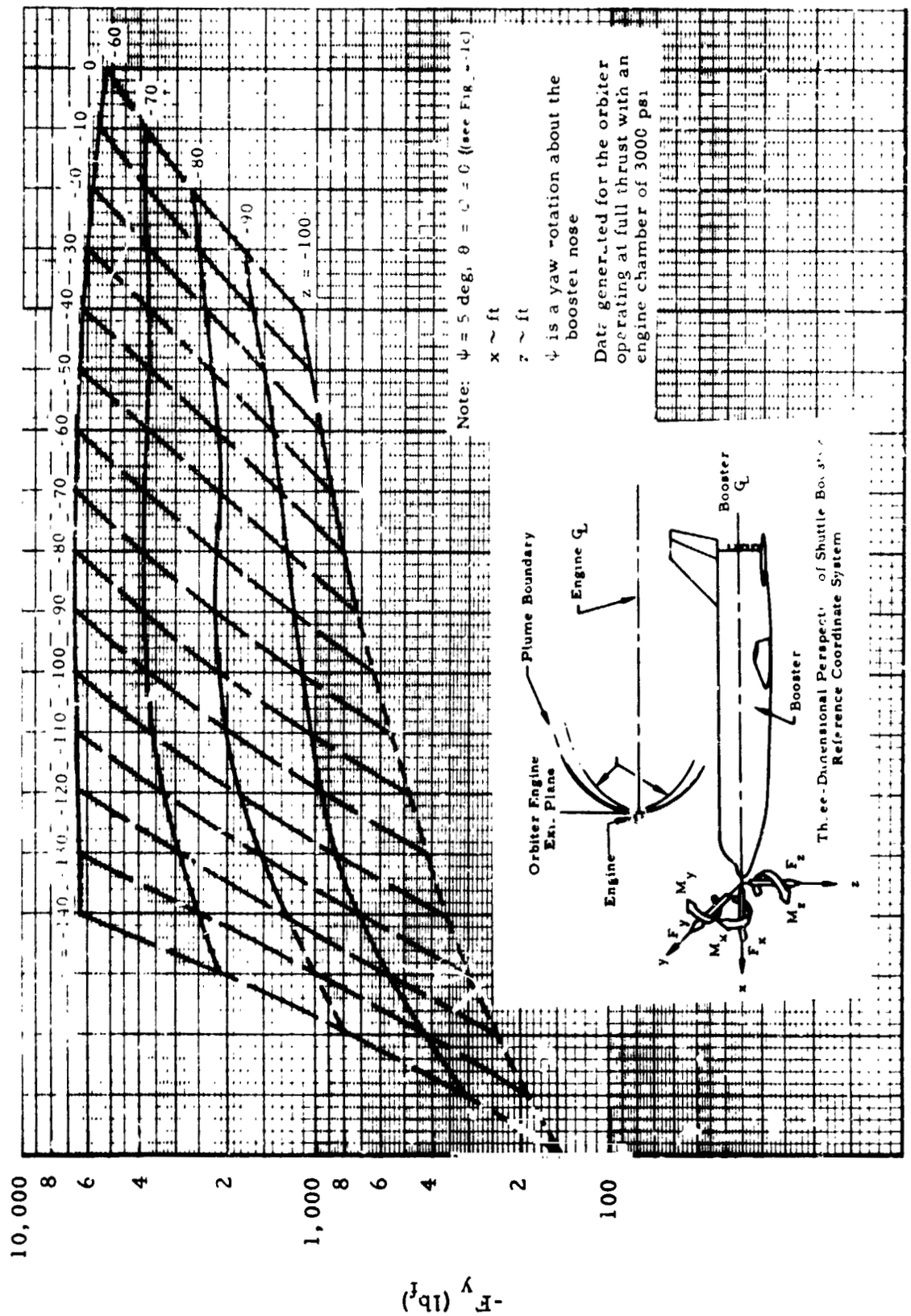

Fig. 2-18 — Variation of the Booster Plume Impingement Force with Orbiter Separation Distance from the Booster

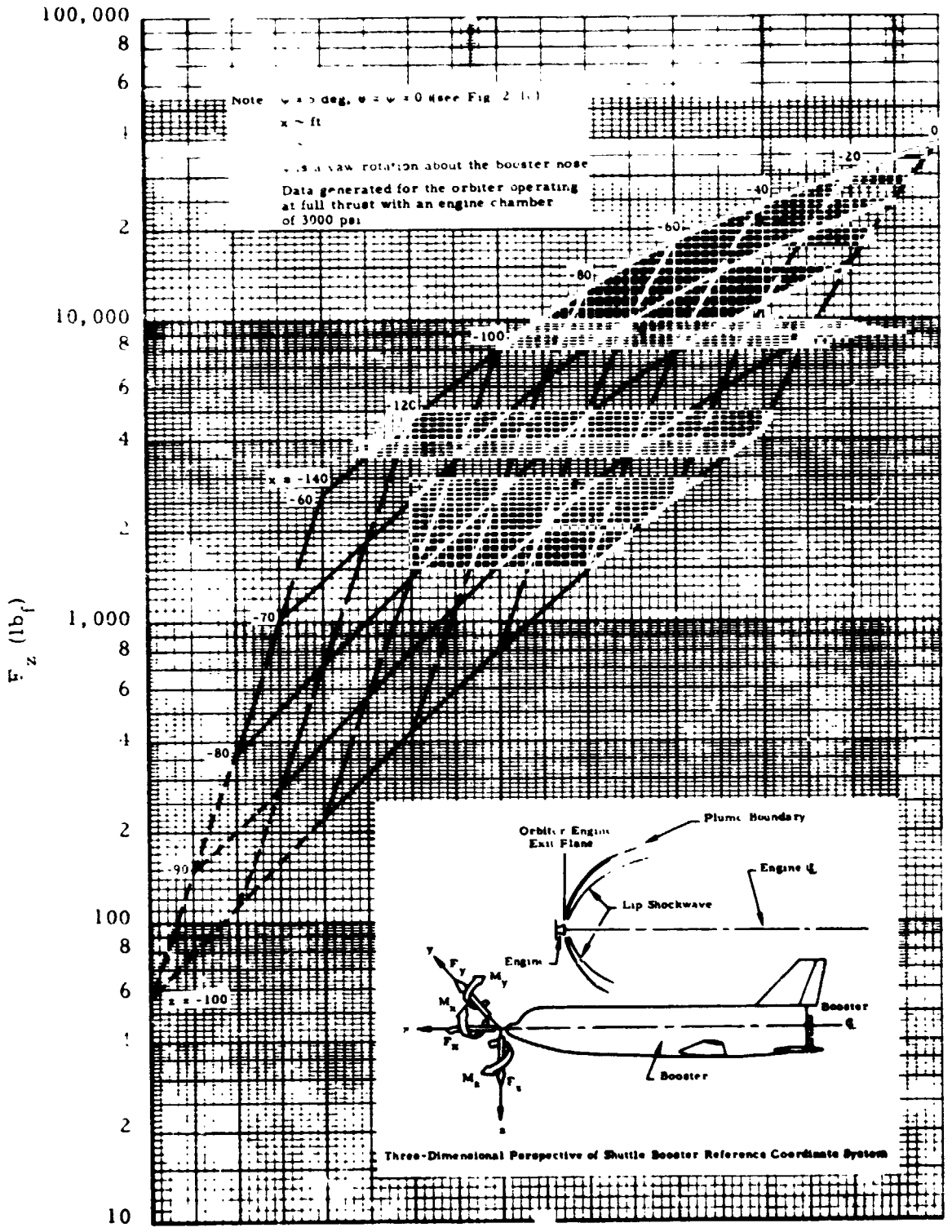

Fig. 2-19 – Variation in the Booster Force due to the Orbiter Exhaust Plume Impingement with Orbiter Separation Distance from the Booster

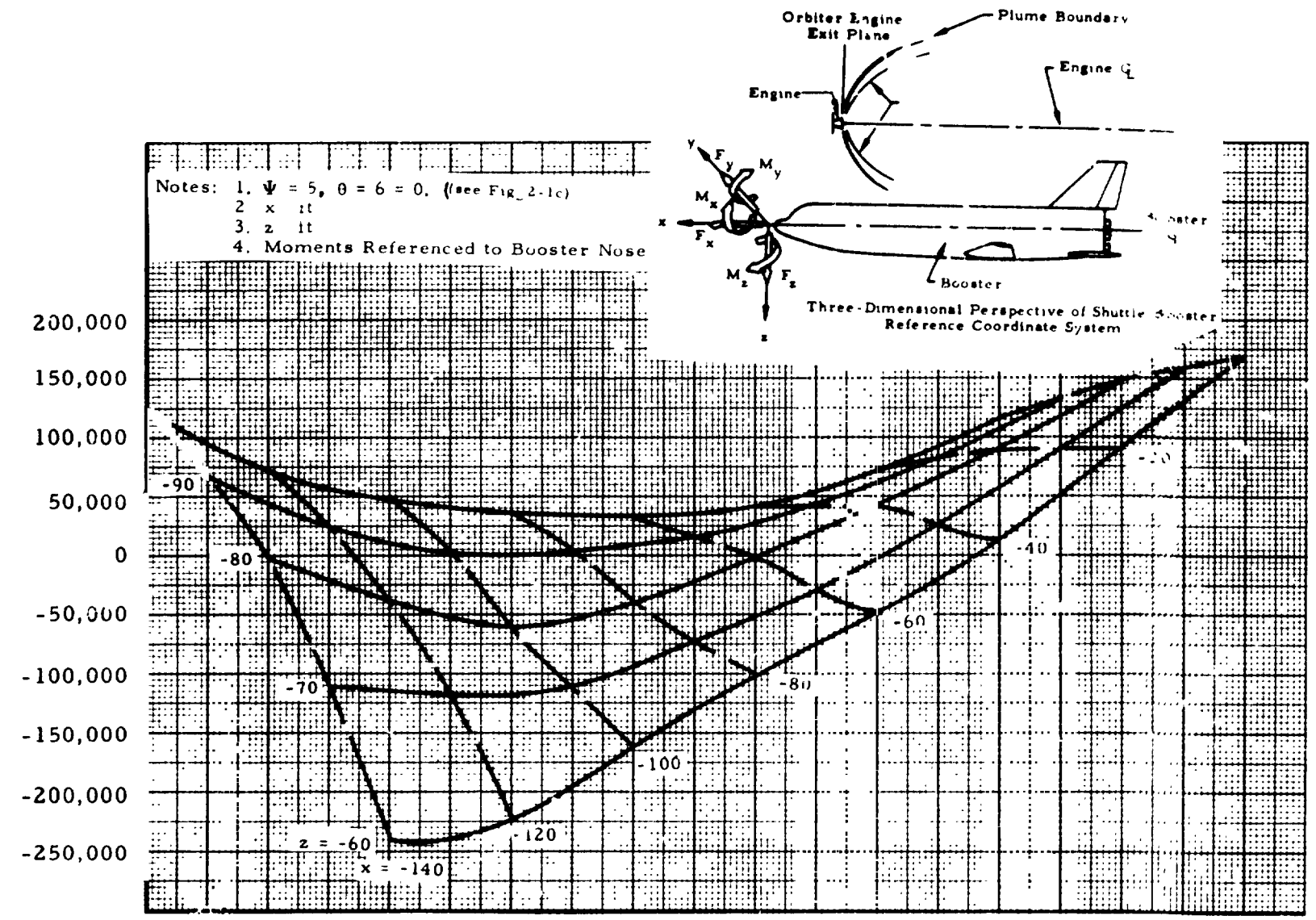

Fig. 2-20 — Variation of Booster Roll Moment Due to Orbit Exhaust Plume Impingement with Orbiter Separation Distance from the Booster

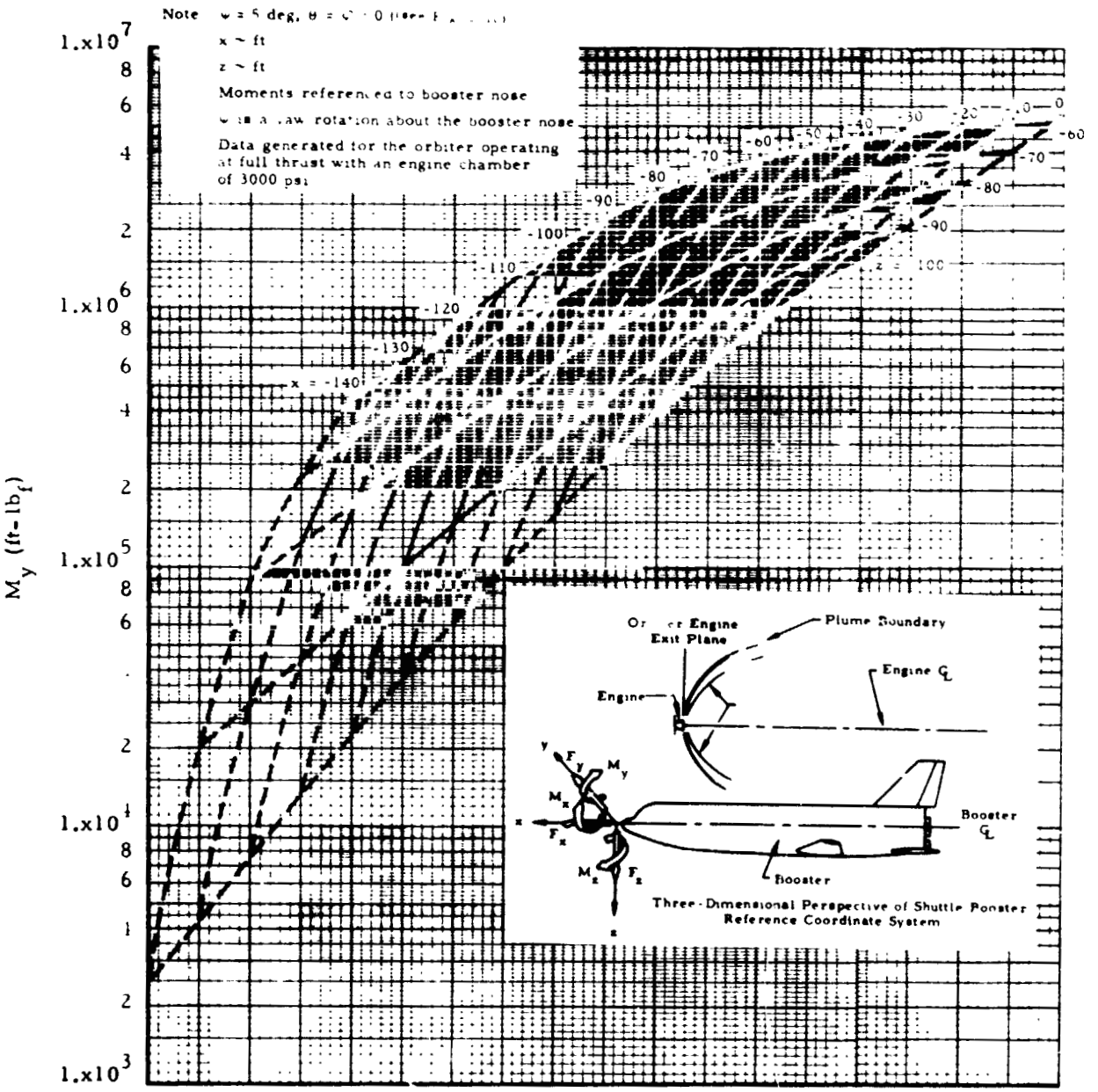

Fig. 2-21 – Variation in Booster Moment Due to Orbiter Plume Impingement (for a 5-deg. yaw about the Booster Nose) with Orbiter Separation Distance from the Booster

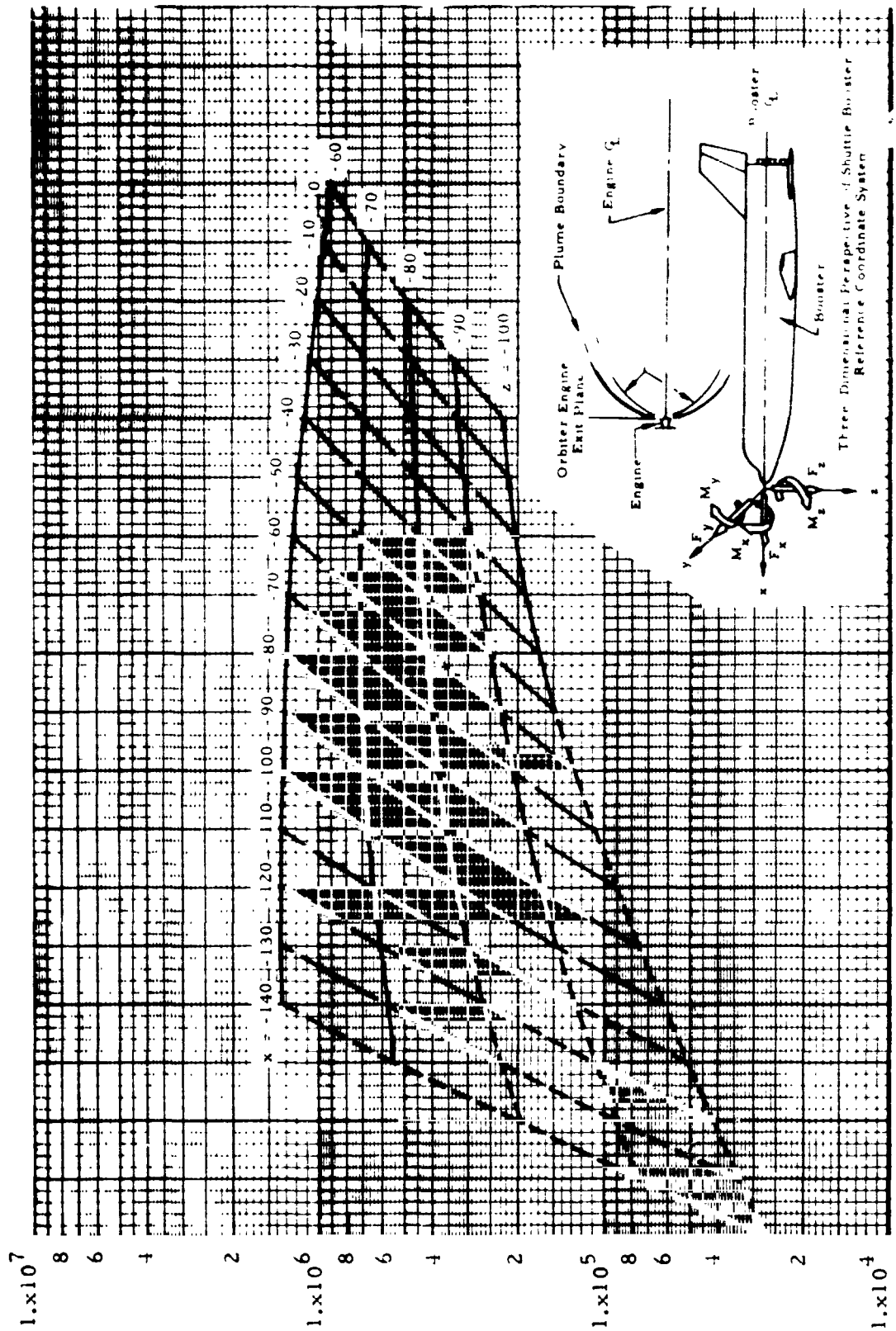

Fig. 2-22 – Variation of the Booster Plume Impingement Moment with the Orbiter Separation Distance from the Booster

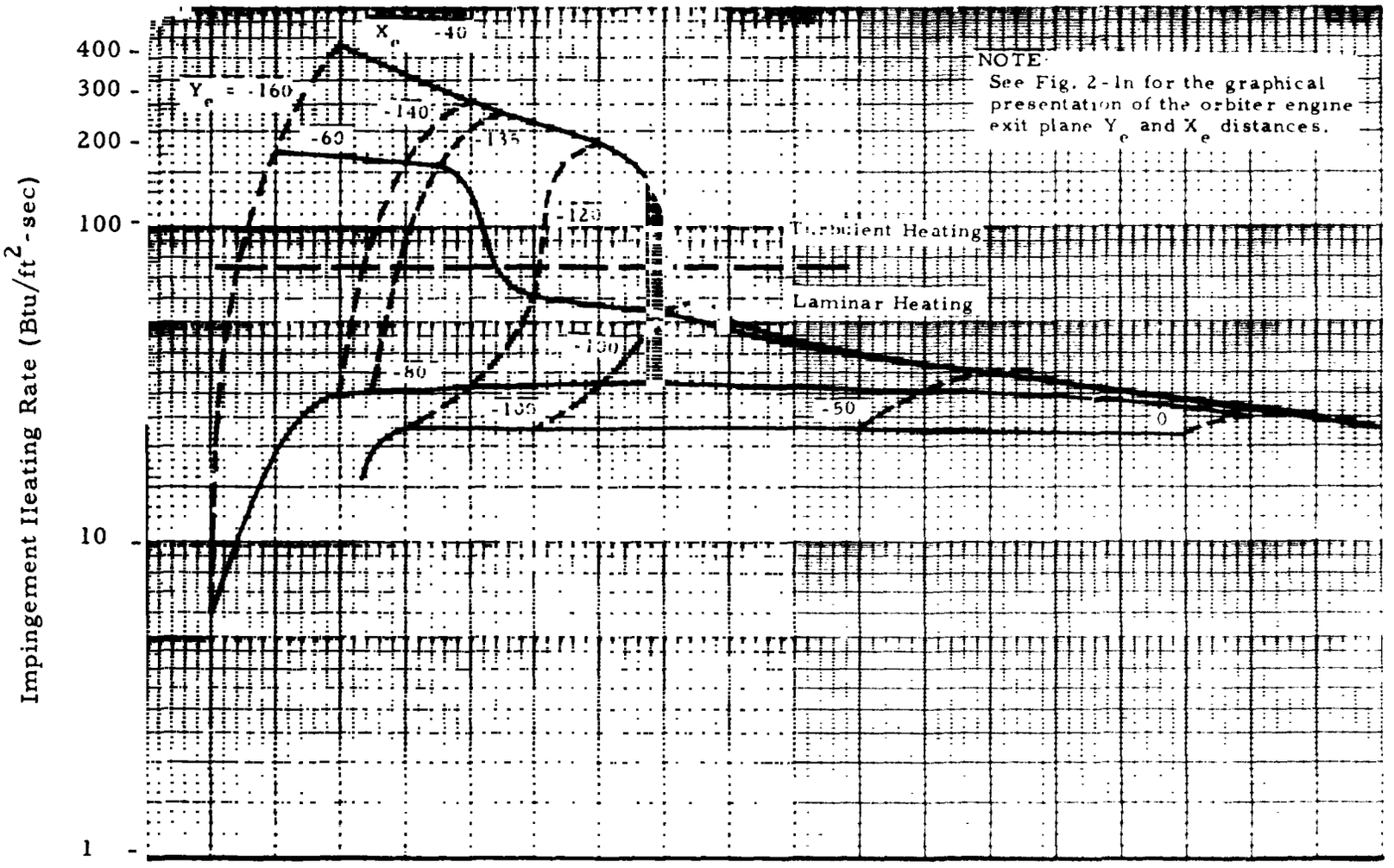

Fig. 2-24 - Variation of the Impingement Heating Rate to the Booster Vertical Tail at Point A as a Function of Orbiter Engine Exit Plane/ Booster Seperation Distance

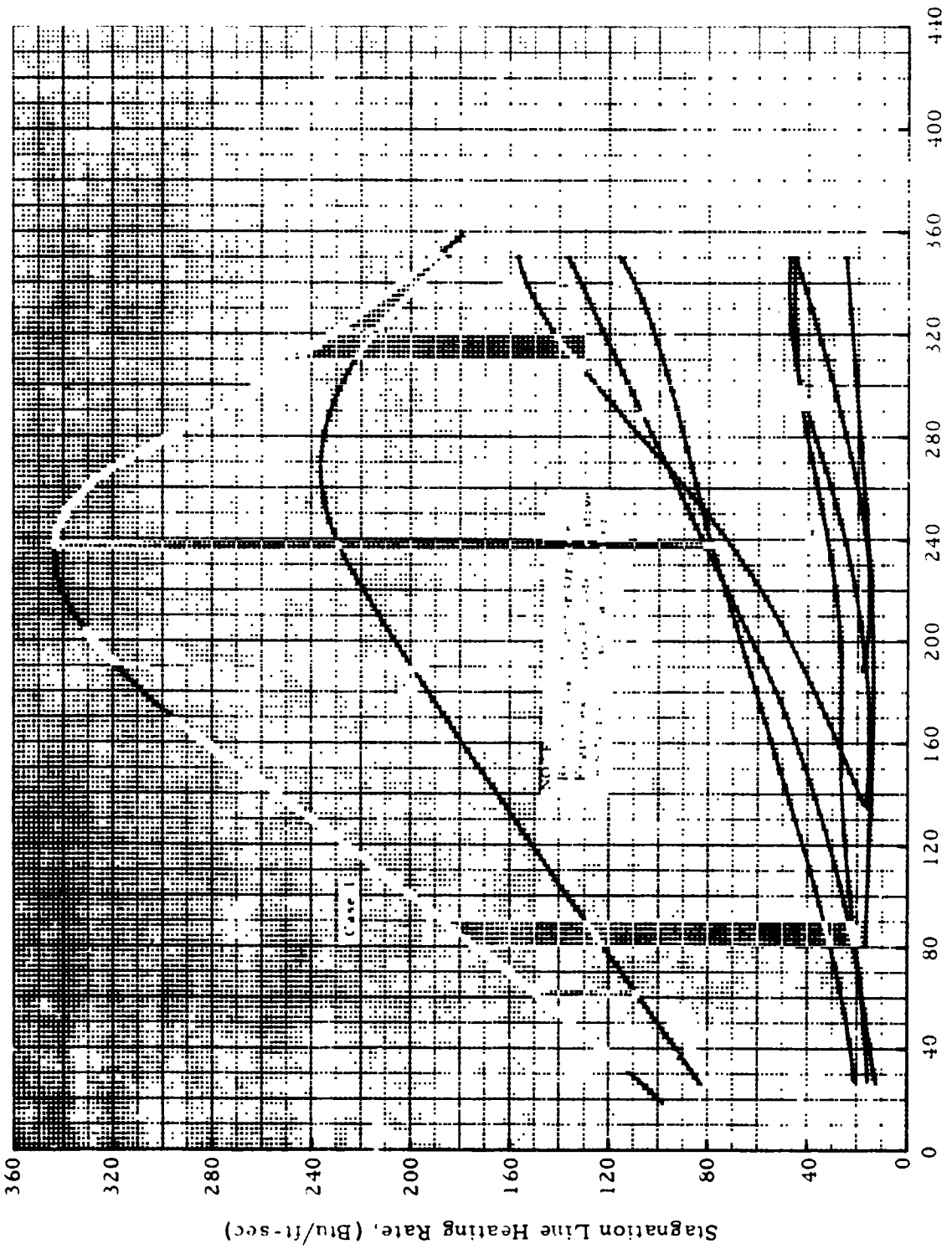

Fig. 2-25a - Variation of the Heating Rate Along the Stagnation Line on the Booster Vertical Tail

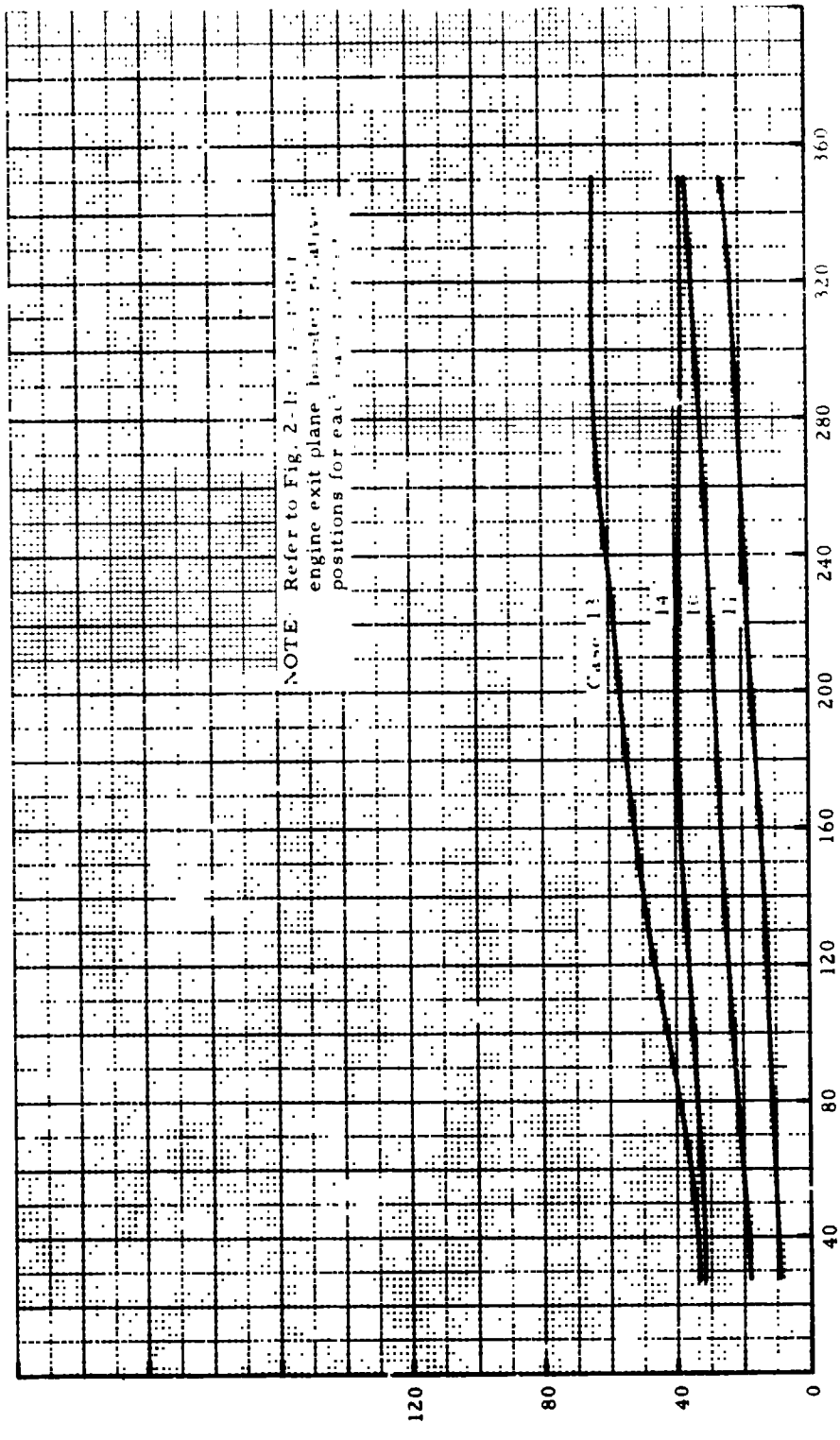

Fig. 2-25b – Variation of the Heating Rate Along the Stagnation Line on the Booster Vertical Tail

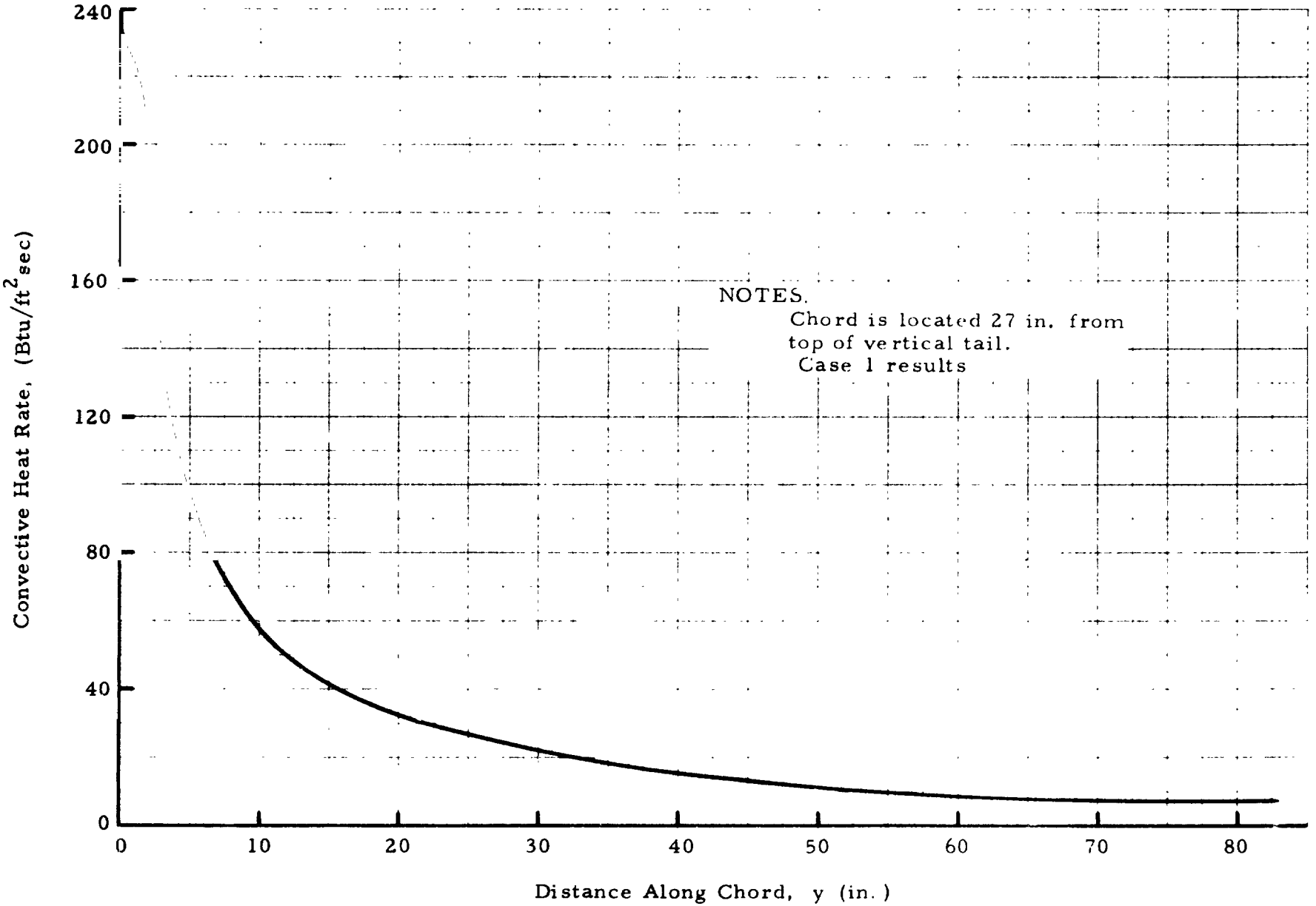

Fig. 2-26 – Variation of Heating Rate Along Chord on Vertical Tail for Case 1(Fig. 2-1n)

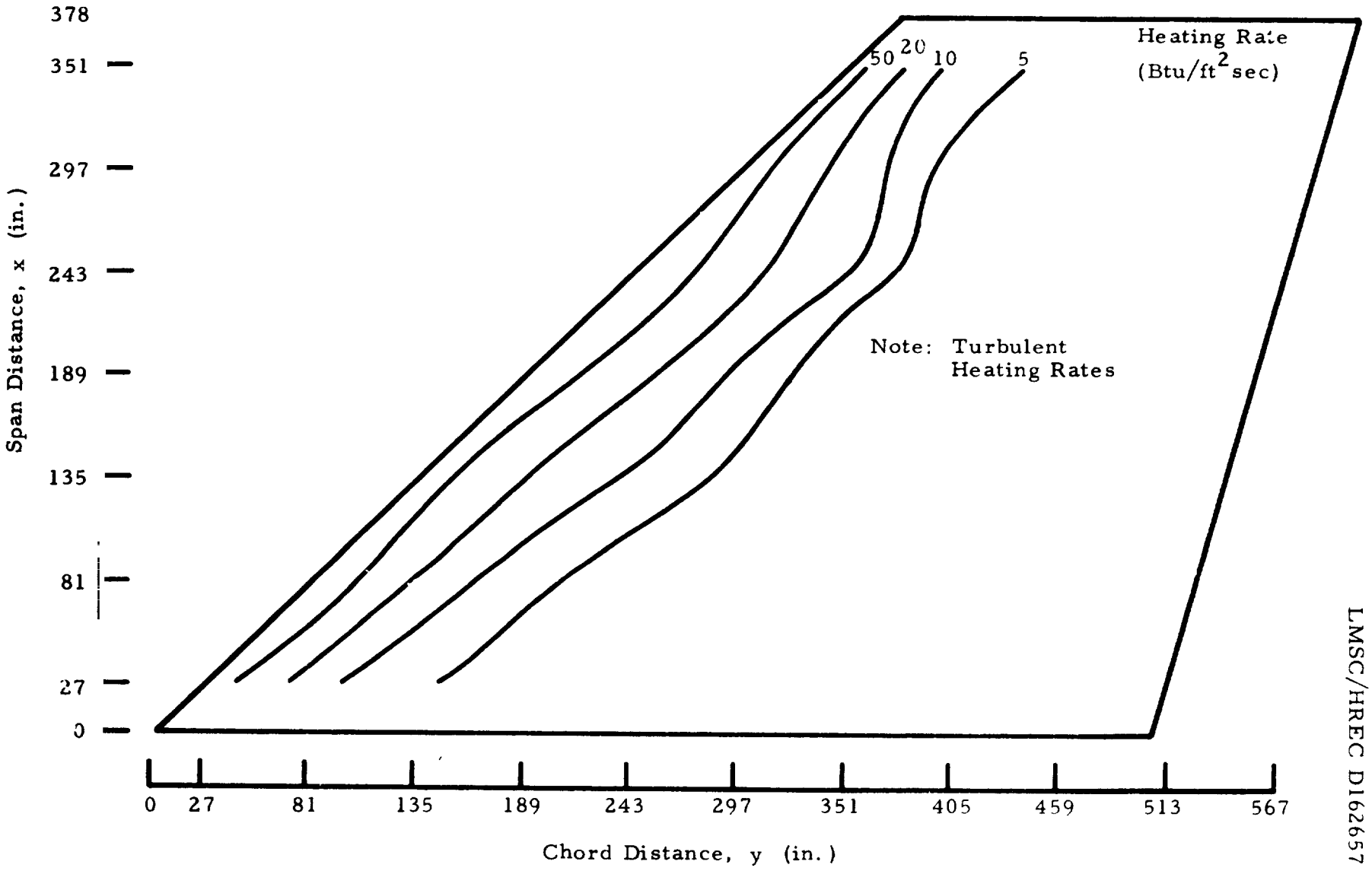

Fig. 2-27a – Heating Rate Contours on the Vertical Tail for Case 1 (Fig. 2-1n)

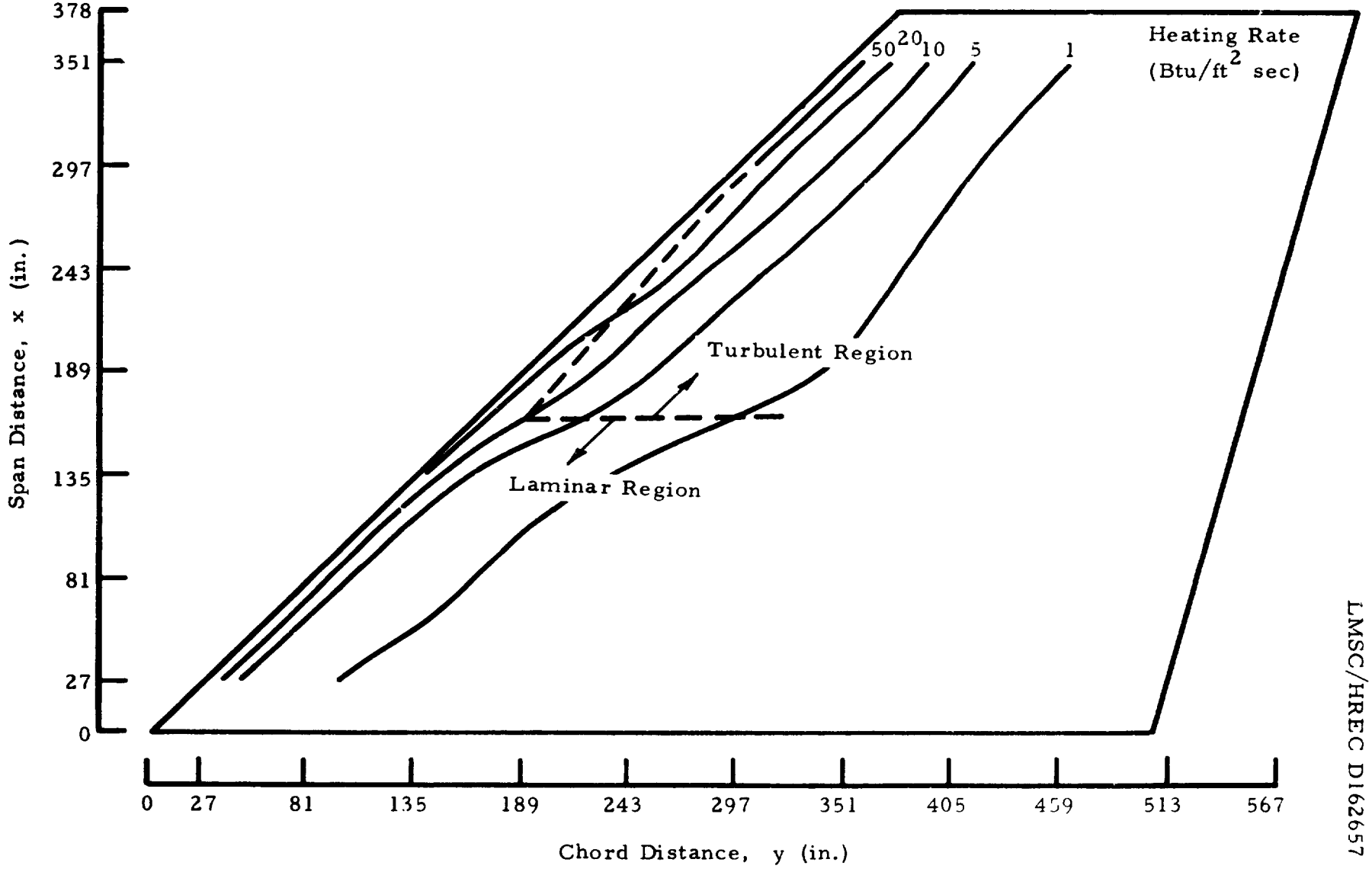

Fig. 2-27b – Heating Rate Contours on the Vertical Tail for Case 4 (Fig. 2-1n)

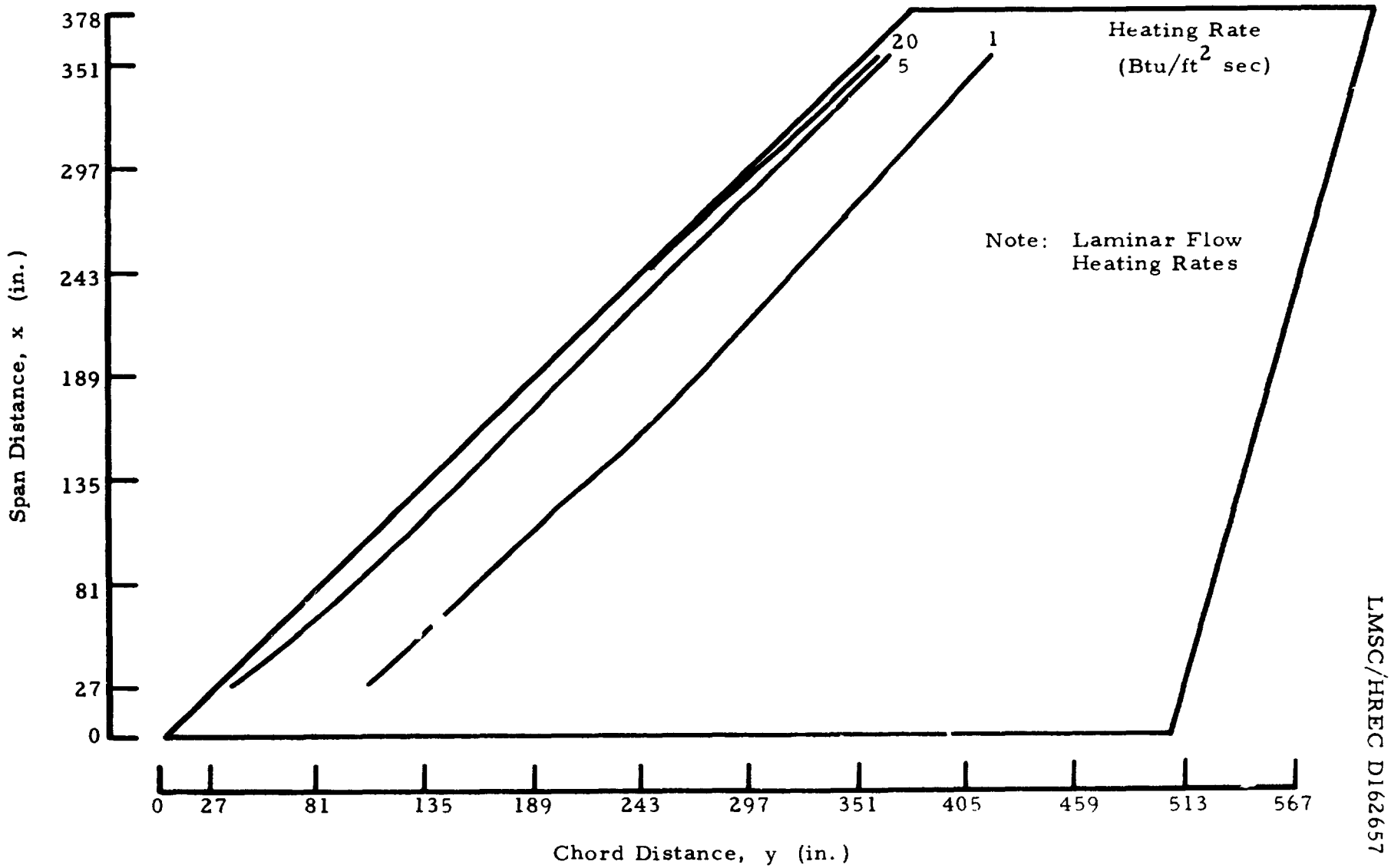

Fig. 2.27c – Heating Rate Contours on the Vertical Tail for Case 10 (Fig. 2-1n)

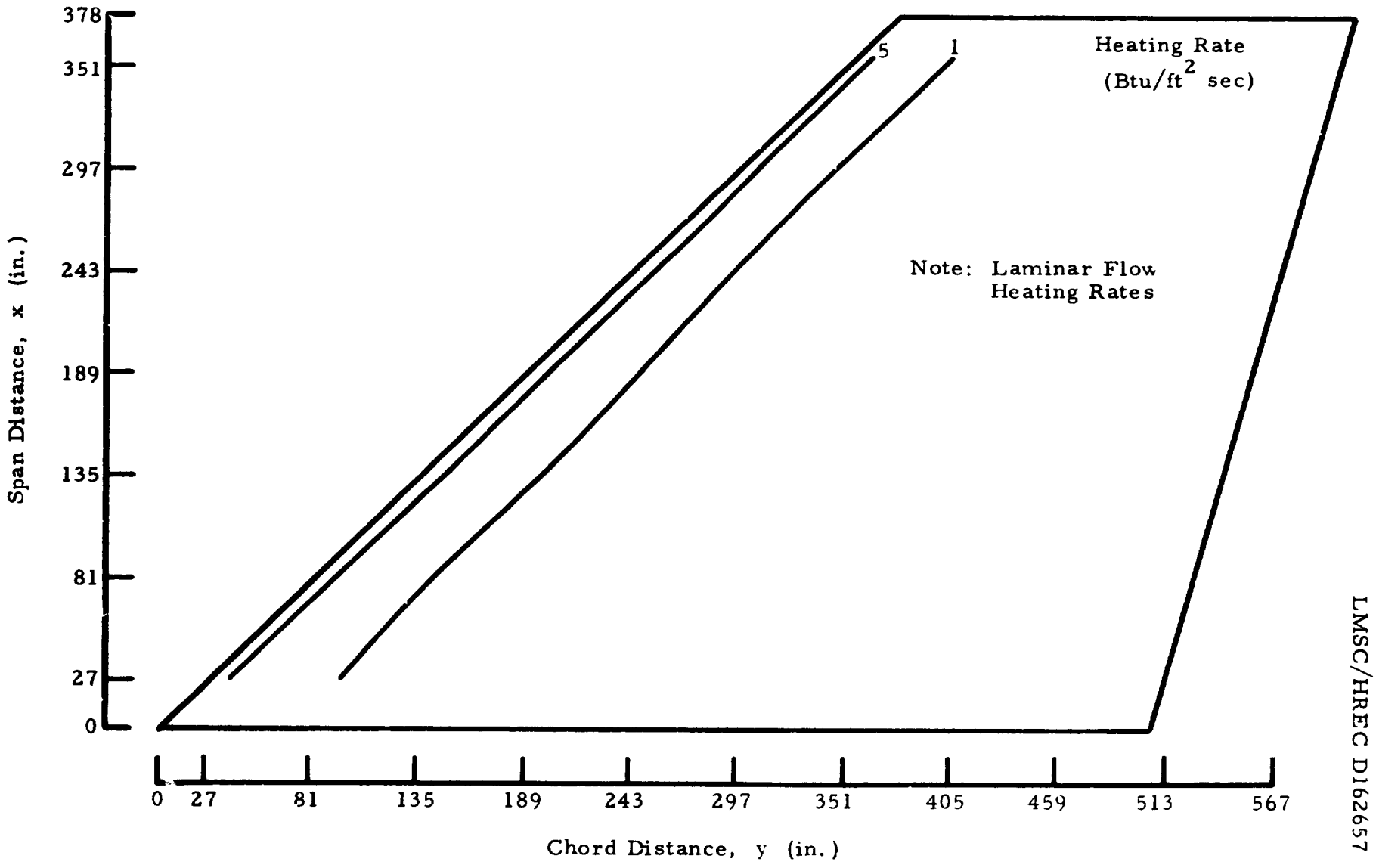

Fig. 2-27d – Heating Rate Contours on the Vertical Tail for Case 12 (Fig. 2-1n)

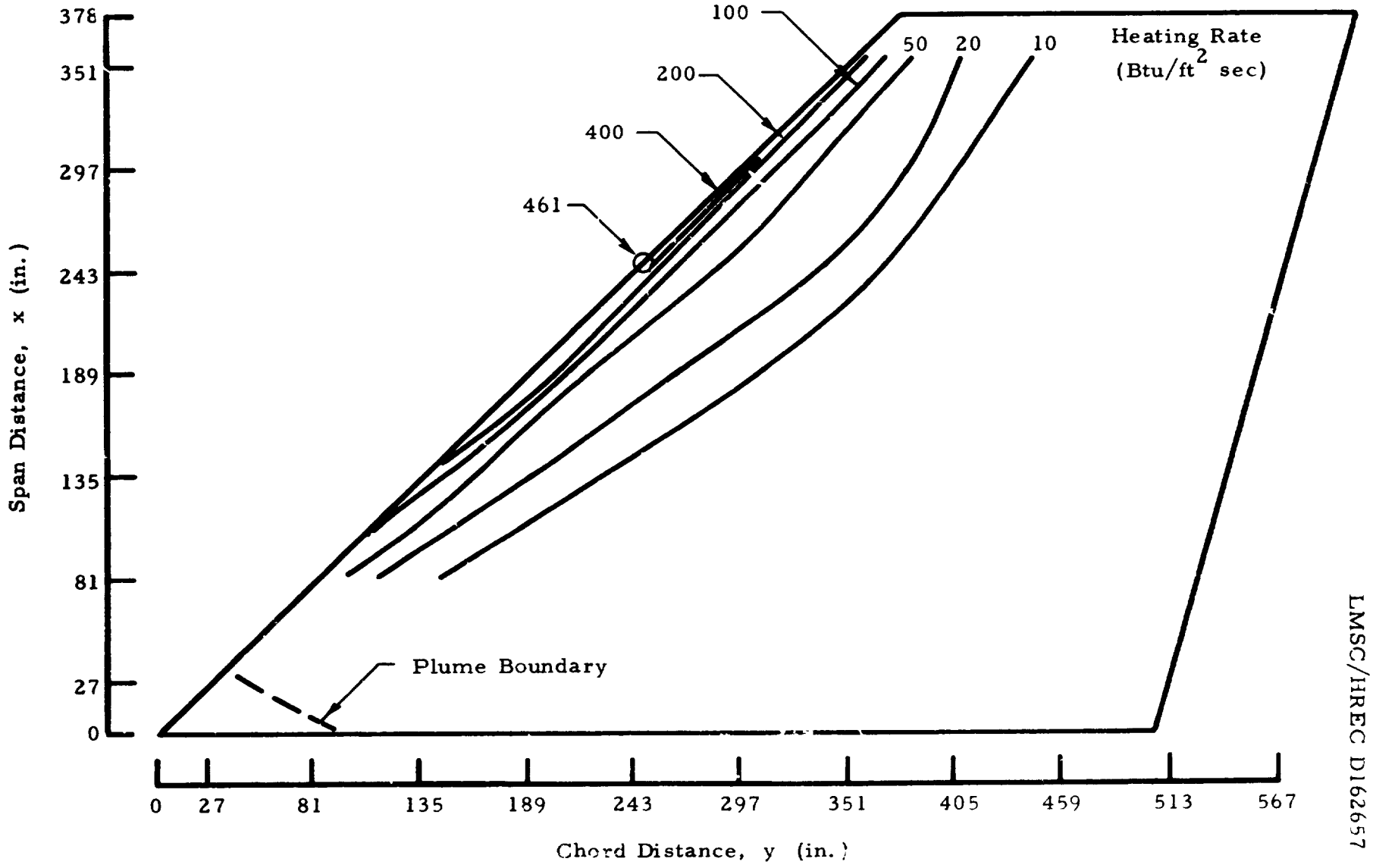

LMSC/HREC D162657

Fig. 2-27e – Heating Rate Contours on the Vertical Tail for Case 15 (Fig. 2-1n)

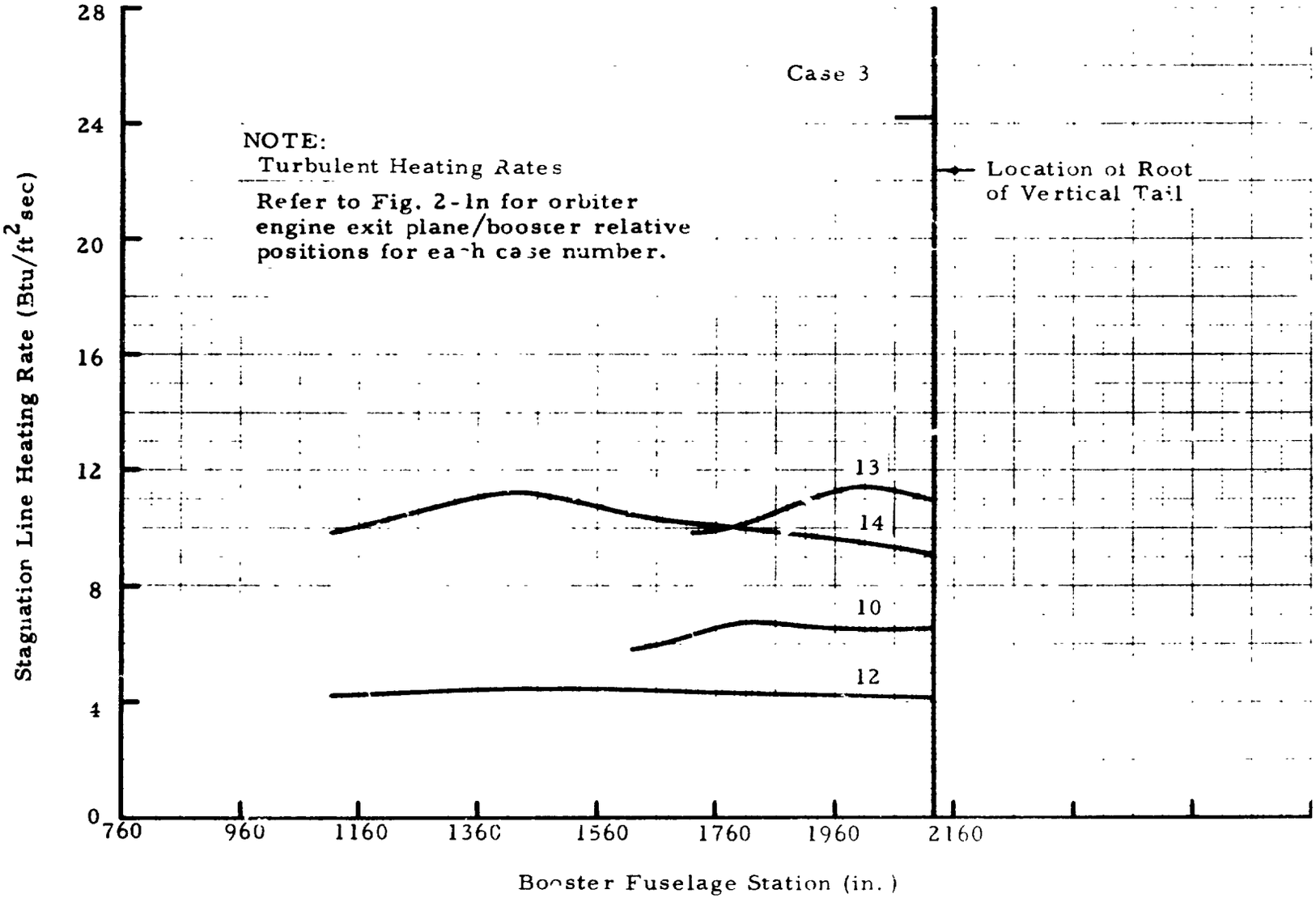

Fig. 2-28 — Variation of the Heating Rate Along the Stagnation Line on the Booster Fuselage

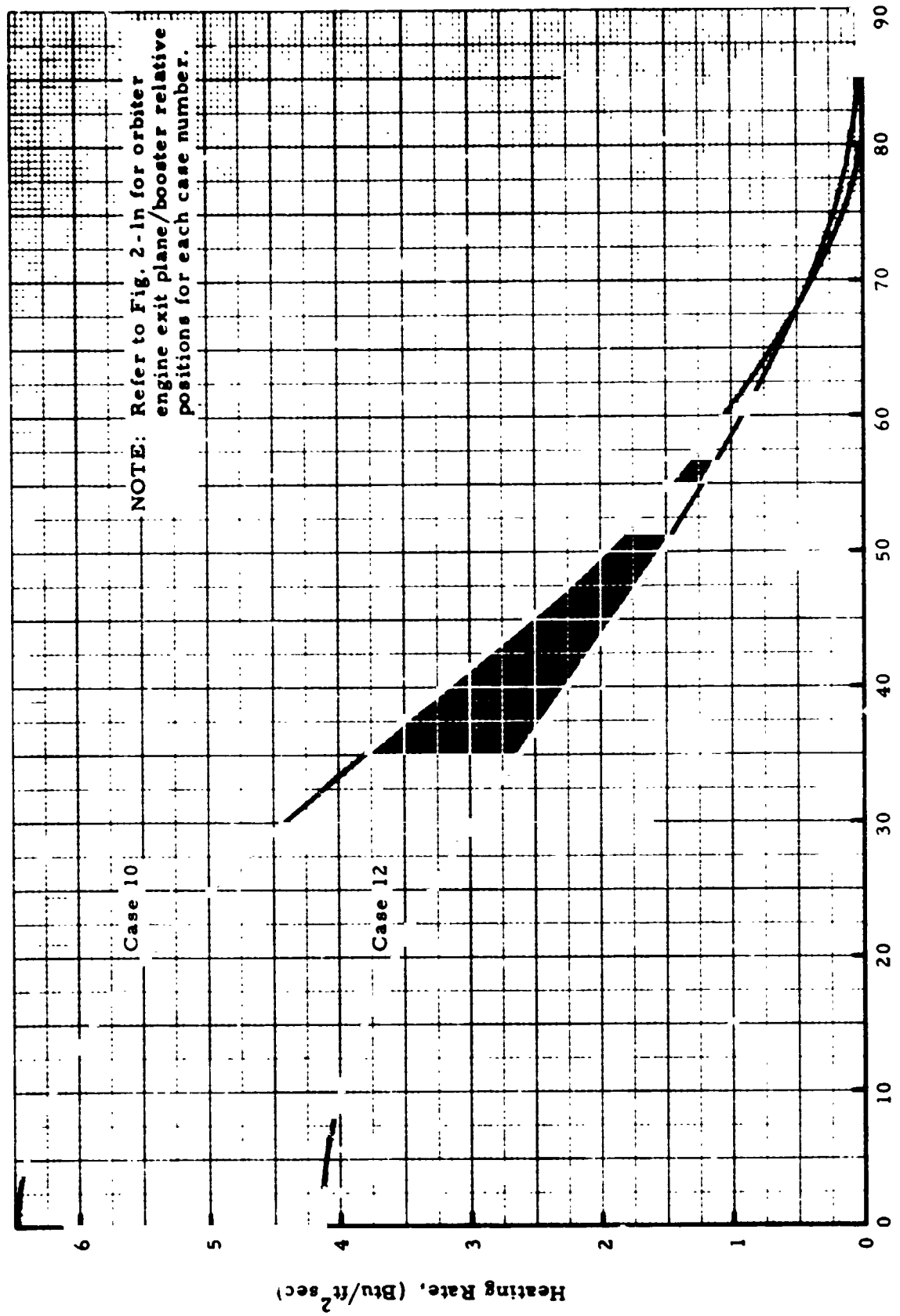

Fig. 2-29 – Variation of Fuselage Heating Rates off the Stagnation Line at a Point Immediately in Front of the Root of the Vertical Tail.

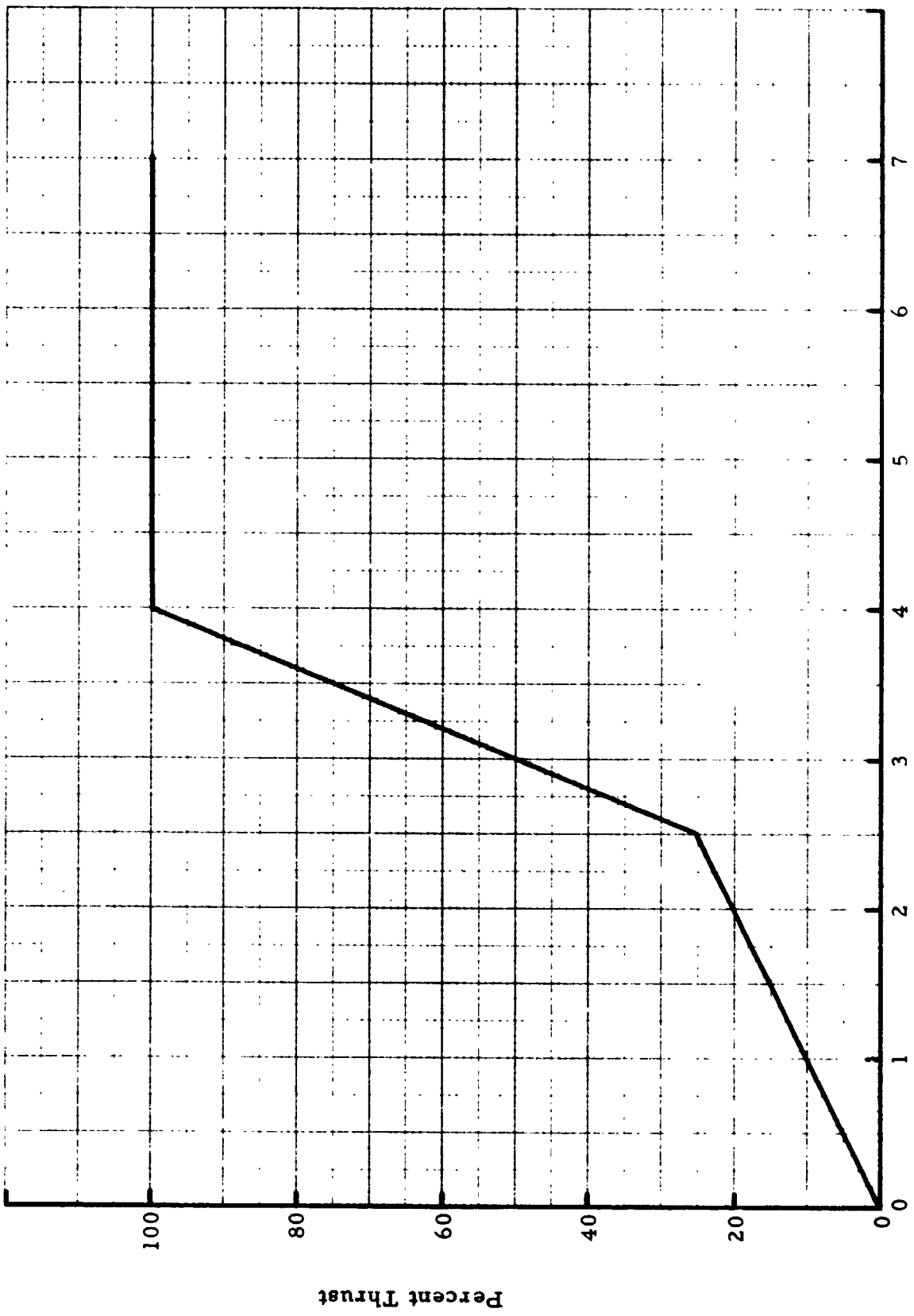

Fig. 2-30 — Orbiter Engine Thrust Buildup Curve

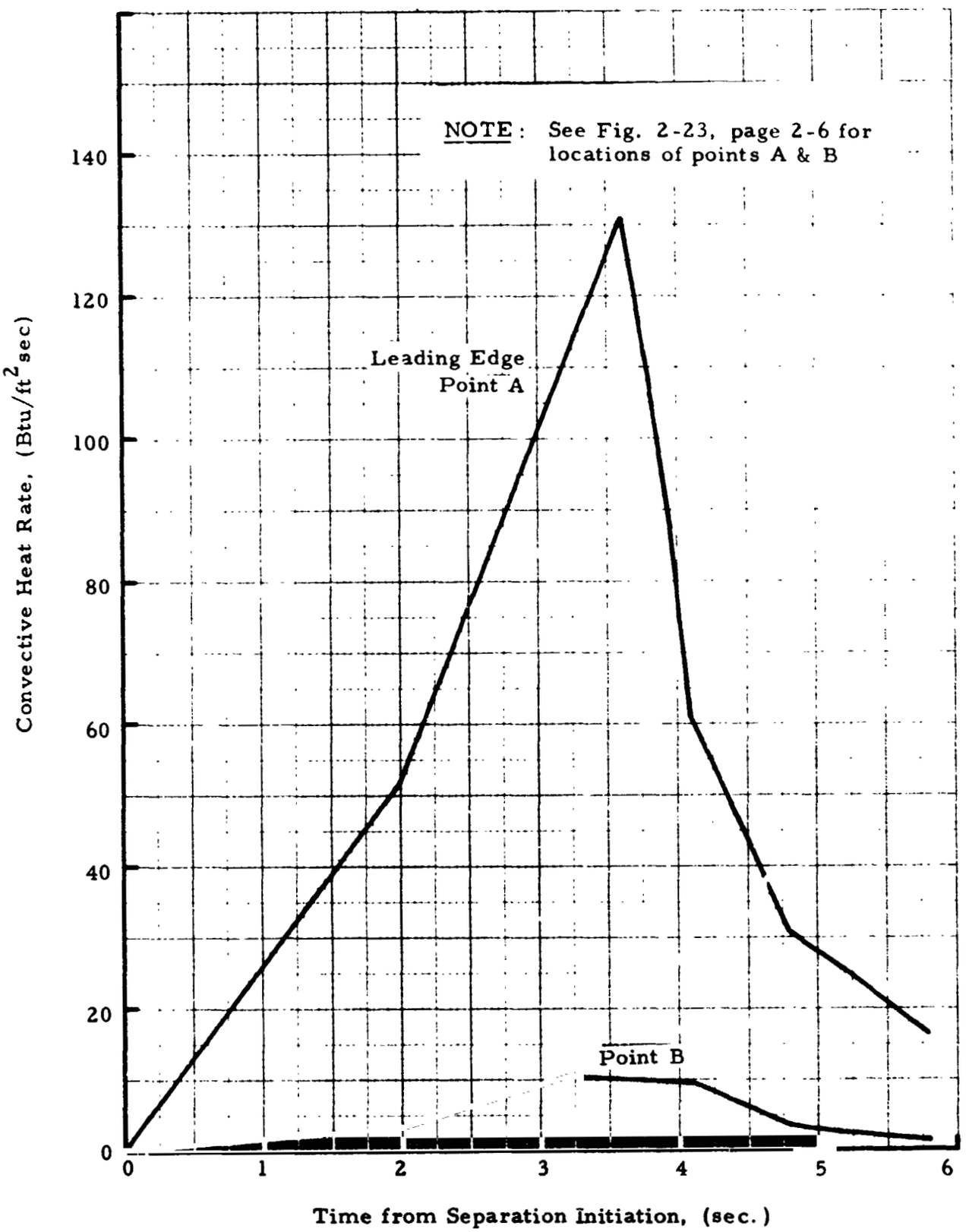

Fig. 2-31 – Heat Rate, Time History for the Vertical Tail for Separation Trajectory No. 1

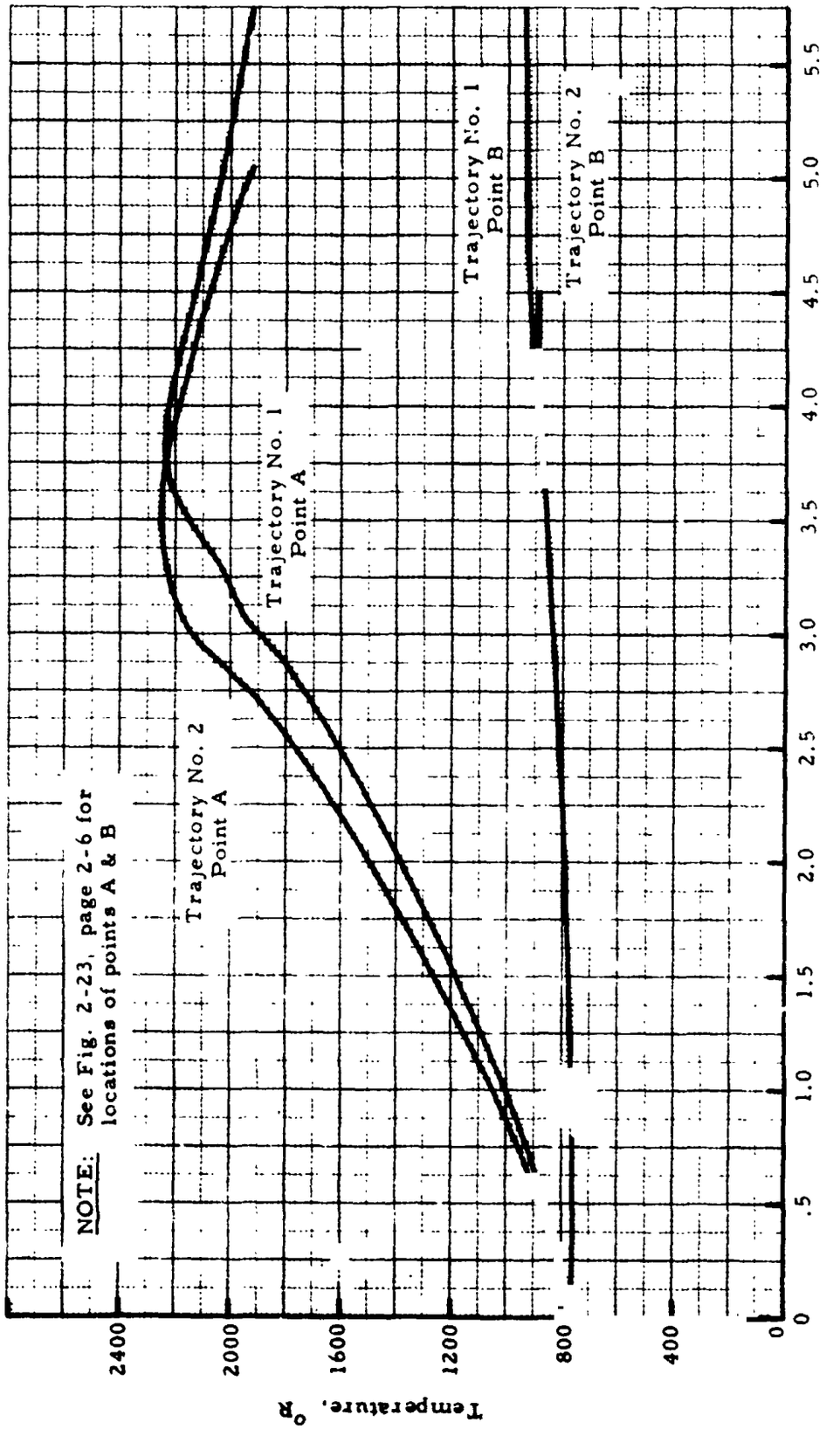

Fig. 2-32 – Surface Temperature, Time History for the Vertical Tail

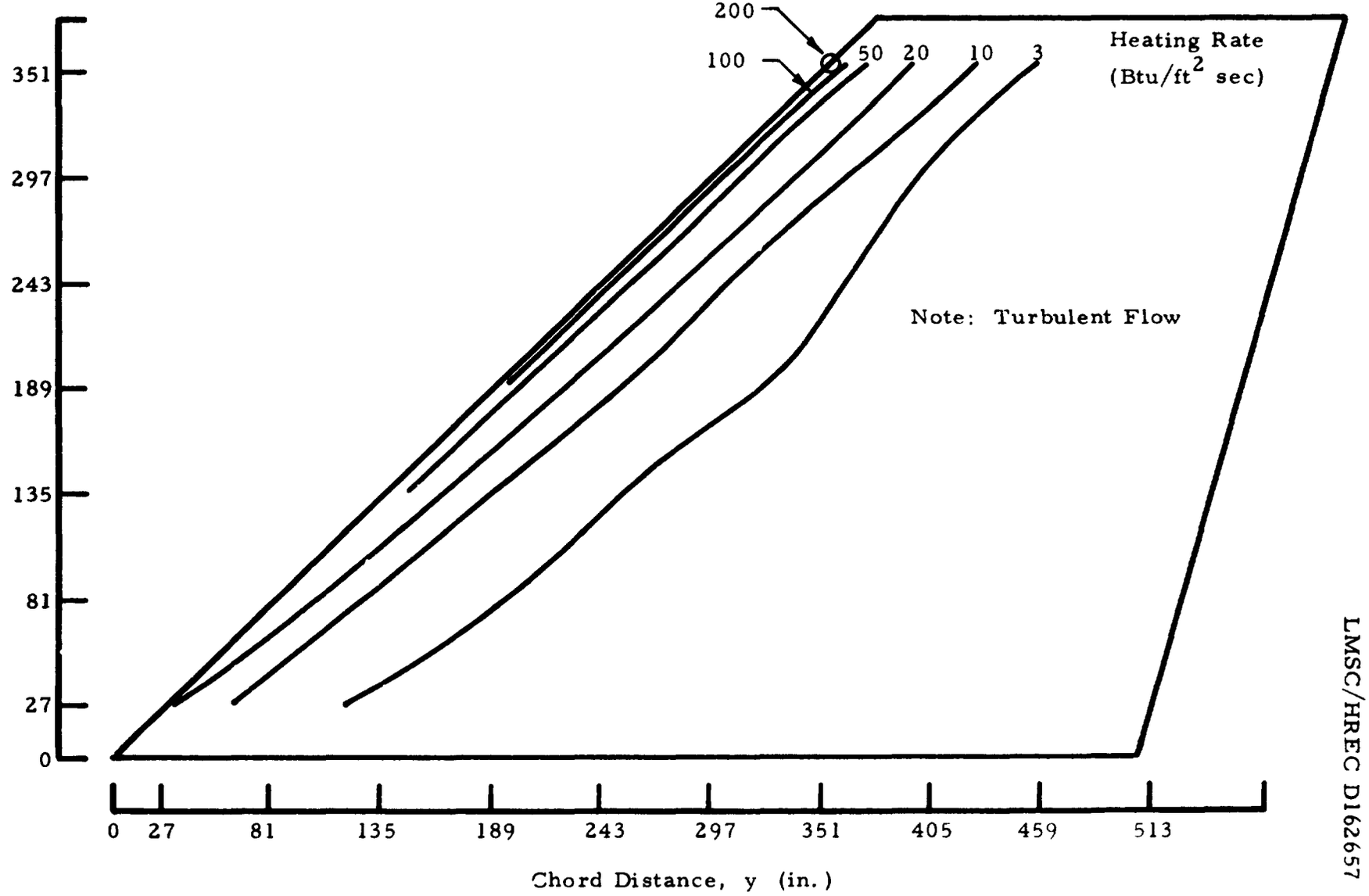

Fig. 2-33a – Heating Rate Contour Plots for the Vertical Tail for Case 16 (Fig. 2-1n)

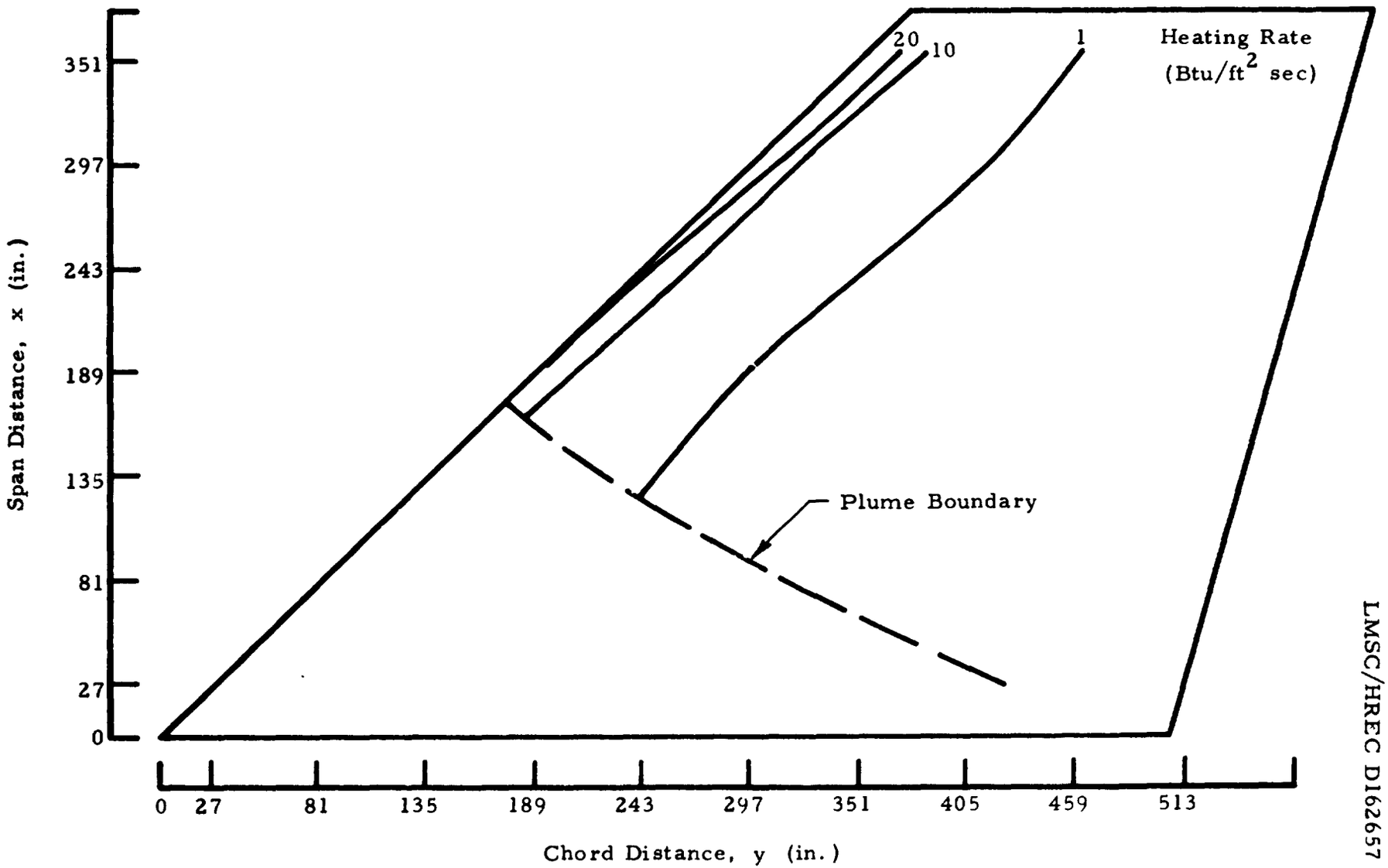

Fig. 2-33b – Heating Rate Contour Plats for the Vertical Tail for Case 17 (Fig. 2-1n)

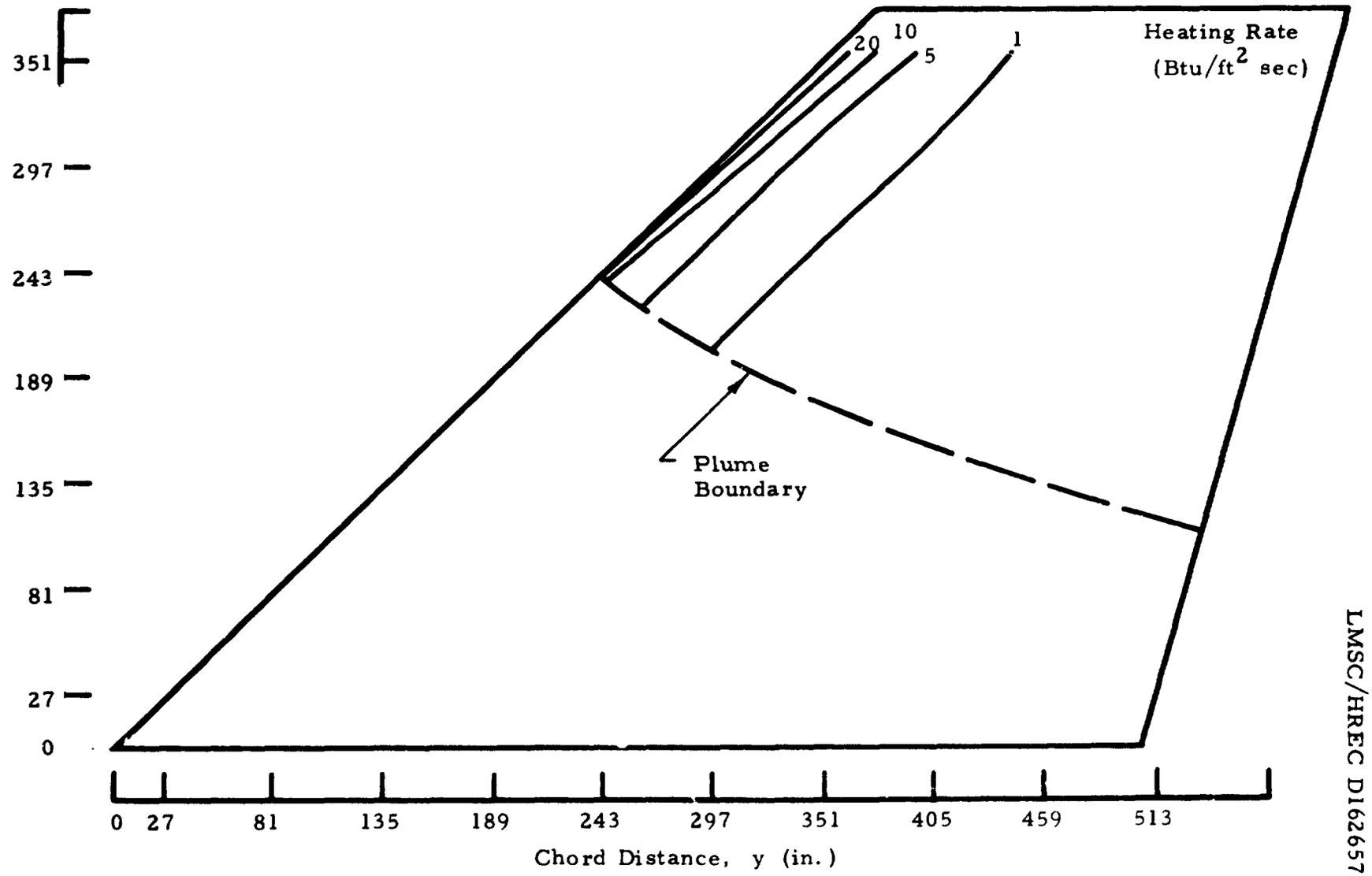

Fig. 2-33c – Heating Rate Contour Plats for the Vertical Tail for Case 18 (Fig. 2-1n)

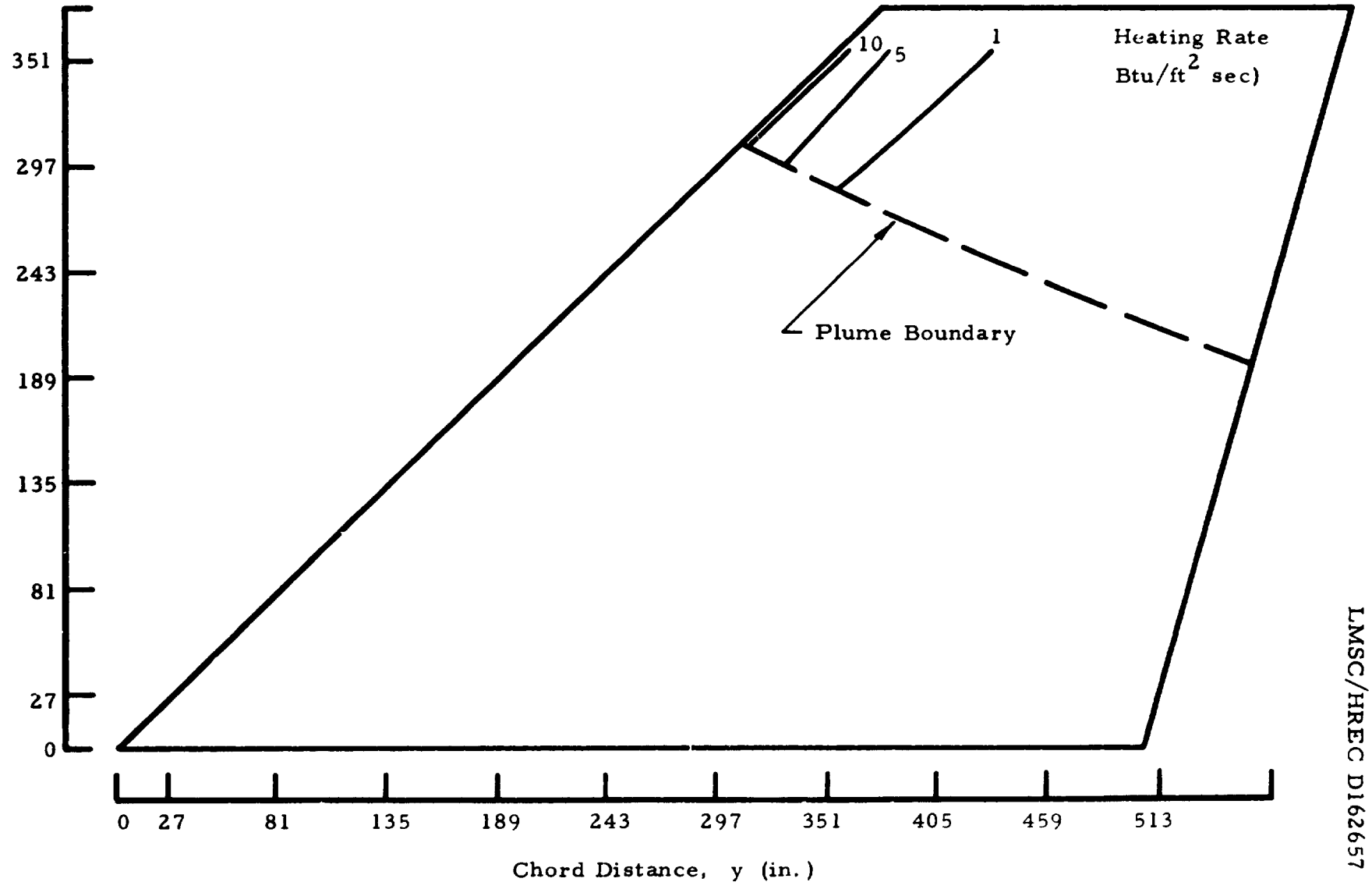

Fig. 2-33d – Heating Rate Contour Plats for the Vertical Tail for Case 19 (Fig. 2-1n)

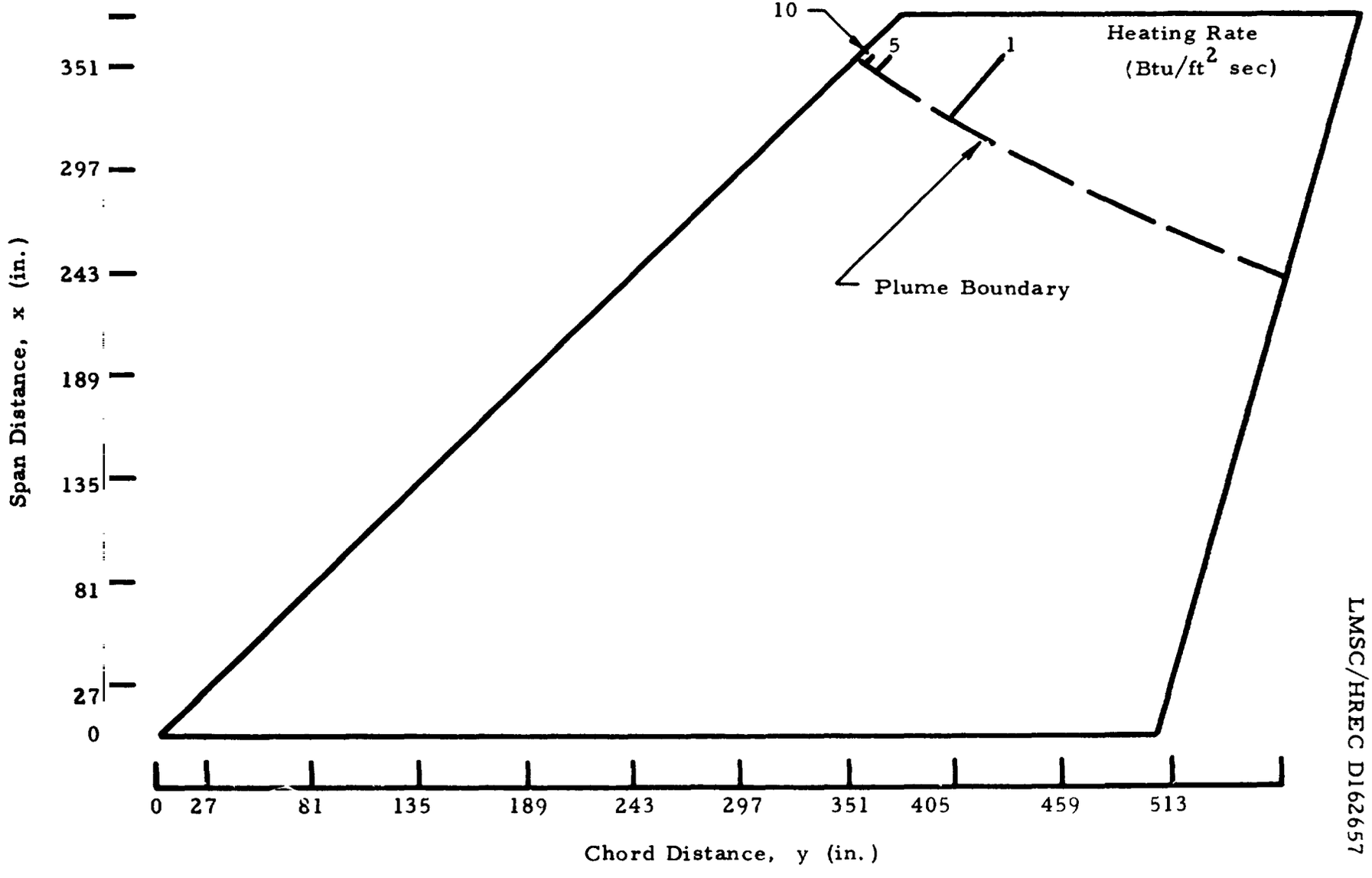

Fig. 2-33e – Heating Rate Contour Plats for the Vertical Tail for Case 20 (Fig. 2-1n)

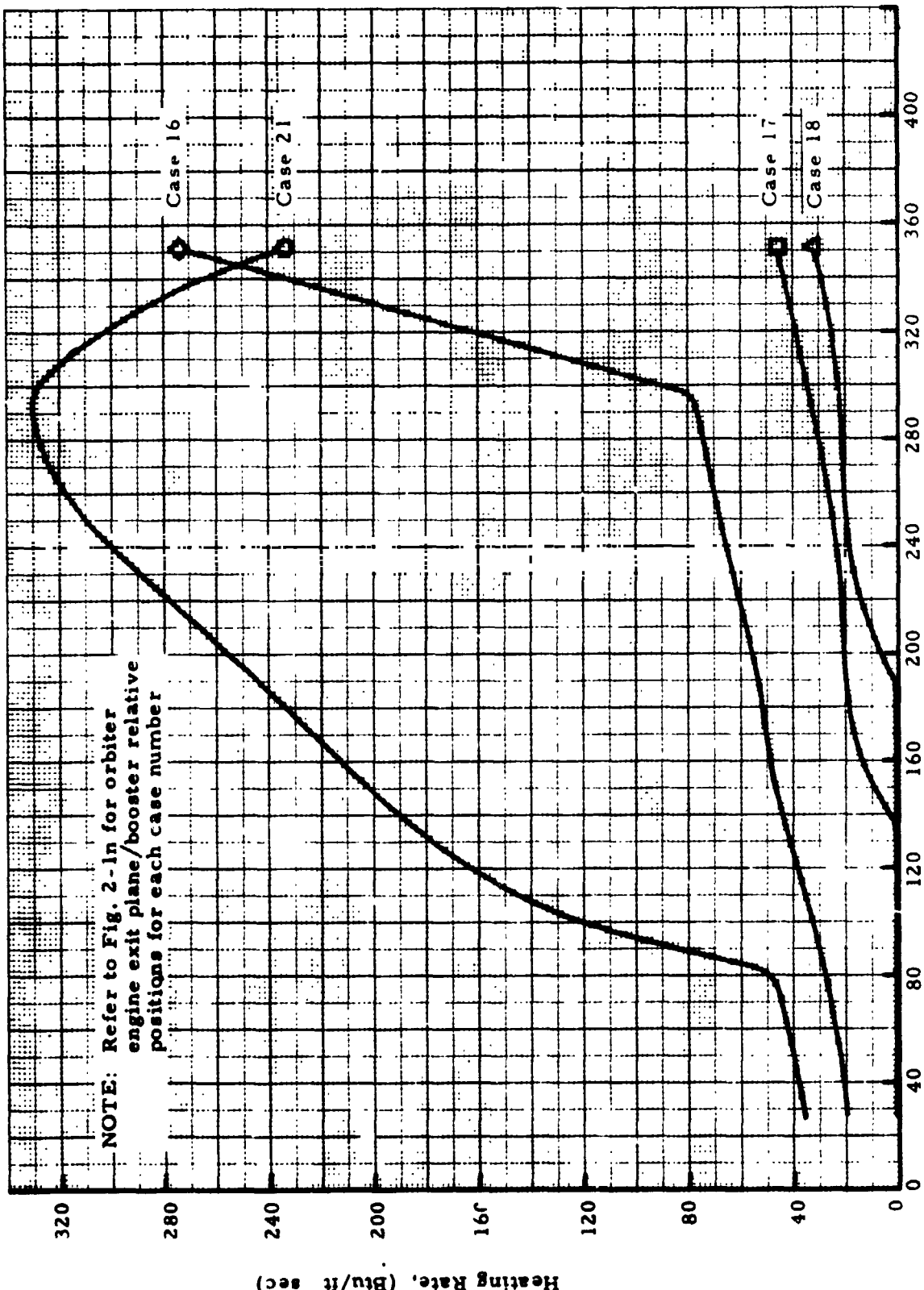

Fig. 2-34 — Variation of the Stagnation Line Heating Rate on the Vertical Tail for Cases 16, 17, 18 and 21

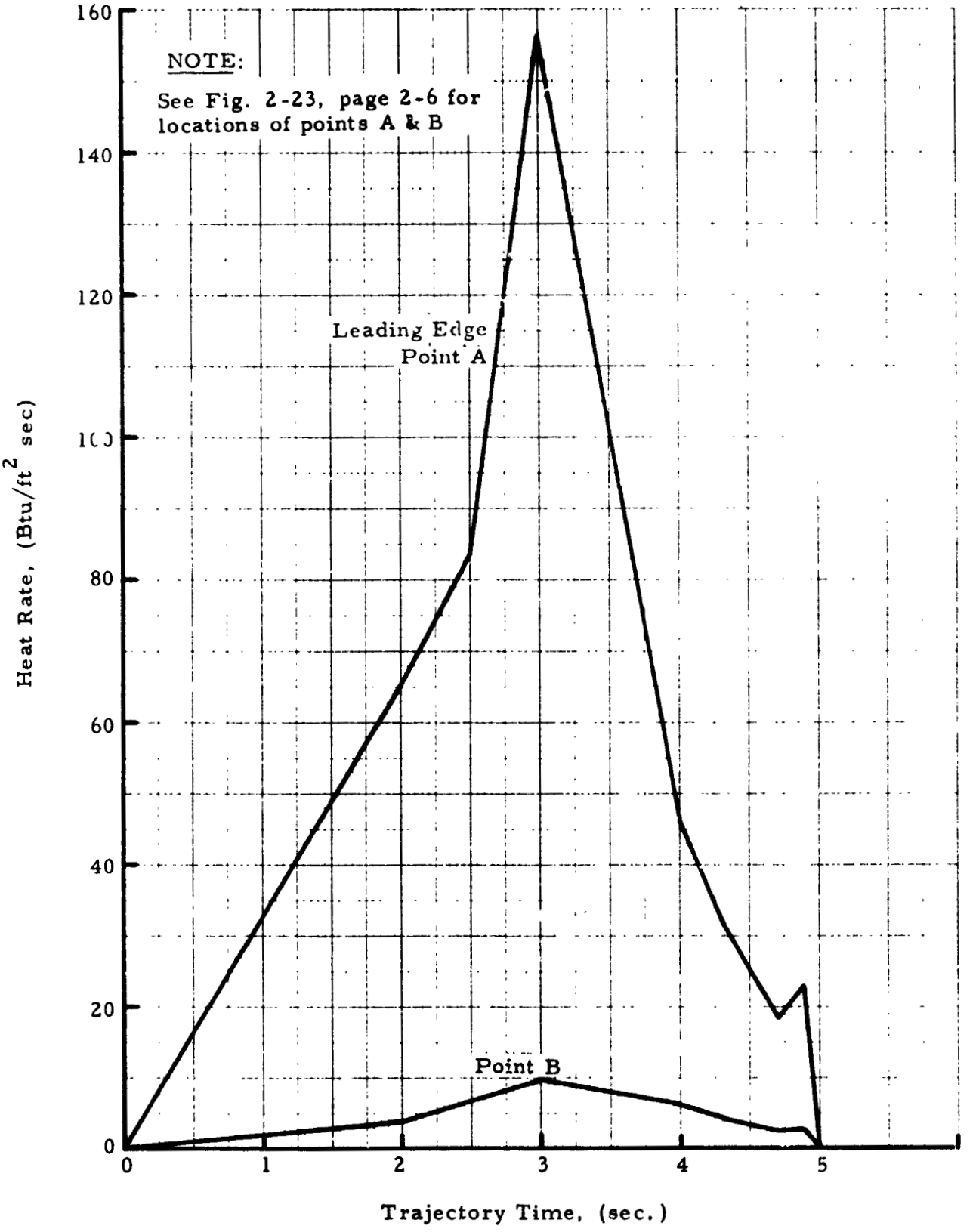

Fig. 2-35 — Heating Rate, Time History for the Vertical Tail for Separation Trajectory No. 2

Section 3
CONCLUSIONS

In this study, the plume impingement heating rates, surface temperatures, forces and moments incurred by the MSC booster during the staging maneuvers were calculated. Although this study was preliminary, the data presented in this report can be used to determine a staging separation trajectory which will result in acceptable impingement surface temperatures, forces and moments. The data include the effects of roll, pitch and yaw maneuvers for the booster and are presented in graphical form.

This study is considered preliminary because: (1) the basic exhaust plume used to simulate the multiple orbiter engine exhaust plume was preliminary in nature and reflects the simplifications and assumptions used to generate it, and (2) the localized effects of plume shock/bow shock interaction phenomena on heating rates were not treated.

Due to the multitude of plume shock/bow shock and fuselage bow shock/vertical tail bow shock interaction situations, it is advisable to first select a staging separation trajectory neglecting these interactions, and then look at these interactions in more detail to determine the optimum staging separation trajectory. Each interaction is a unique situation and must be analyzed separately.

In order to determine if a staging separation trajectory resulted in "acceptable" heating rates, it was necessary to perform a transient heat conduction analysis to determine if the booster skin temperature exceeded the maximum structural temperature limits. Using a simplified thrust buildup curve, the heating rate-time histories to selected points on the MSC vertical tail were used in a simple one-dimensional heat conduction program to calculate the surface temperature-time histories. These surface temperature-time histories were calculated for two separation trajectories. The maximum

calculated surface temperature at the leading edge of the vertical tail was 1800°F for both of the separation trajectories analyzed. The titanium skin on the sides of the vertical tail reached 480°F and 440°F for the two separation trajectories analyzed. The temperatures are below the maximum structural temperatures of 2700°F for the NASA-MSC carbon/carbon leading edge material and 600°F for the titanium skin on the side of the vertical tail.

The predicted forces and moments resulting from the orbiter main stage engine exhaust plume impingement on the booster give realistic data for use in preliminary studies concerning the staging sequence of the space shuttle vehicle. These data, though of a preliminary nature, are considered to predict closely the force and moment trends to be experienced by the booster due to orbiter exhaust plume impingement. A detailed analysis which includes the effects of the orbiter nozzle internal shock wave and the shock waves produced by the two engine plume interaction region will tend to redistribute the impingement flow properties locally. However, the integrated force values should remain substantially unchanged.

The present study disclosed several areas which could pose potential problems as a result of the orbiter exhaust engine plume impinging on the booster. These are:

1. A positive pitch rotation (rotation about the booster y axis; Fig. 2-1c) will tend to produce a booster pitching moment which acts in the same direction as the booster rotation if the plume impingement center of pressure is aft of the booster c.g. This could be somewhat critical during the initial phases of the staging sequence since in this case the impingement will always be aft of the booster c.g.

2. A yawing rotation of the booster about the Z axis (Fig. 3-1c) will produce an unstable effect in that the moment which will act on the booster in the yaw direction will augment the booster yaw motion.

Hence the booster would continue to rotate since the large vertical tail would become more fully exposed to the exhaust plume. A yawing rotation will also produce a roll moment acting on the vehicle which will be acting in the direction of vehicle roll. Hence, if the moments resulting from plume impingement were to become substantial, the vehicle would tend to tumble.

3. The deflection of the wing horizontal tail surface as a result of the plume impingement load distribution would result in larger loadings and hence increase the magnitude of the potential problem discussed above.

Areas which should be investigated in addition to the present analysis are: (1) the engine-out case for side-by-side mounted engines (since this would produce moments which will tend to rotate the vehicle about the roll and yaw axes); (2) effects of misalignment of the wings and tail surfaces with respect to the booster fuselage; and (3) misalignment of the orbiter main stage engine with respect to the gimbal plane.

Appendix A

ROCKET EXHAUST PLUME ANALYSIS

Appendix A

Representative plumes for the single and multiple nozzle Space Shuttle orbiter engines were generated for the analysis of Phase I of this study. The plume analysis considered the Rocketdyne version for the orbiter main stage engine (Table A.1).

A.1 THERMOCHEMISTRY ANALYSIS

The proposed Space Shuttle main propulsion engines employ the concept of staged combustion which is reflected in the gas thermochemical data (Table A.2). Thermochemical properties of the preburner combustion process were generated using the NASA-Lewis Chemical Equilibrium Composition (CEC) Computer Program.* The propellant used in the preburner analysis was: O_2 as the oxidizer and H_2 as the fuel with a mixture ratio of 6. An estimate of the change in total enthalphy of the preburner combustion gases across the hydrogen and oxygen turbines was obtained from turbine power and efficiency data. Thermochemical properties resulting from the main burner combustion process were then calculated using the preburner combustion products as the propellant and including the adjusted total enthalpy in the analysis. The data from this analysis was used in all the subsequent flowfield analyses and are presented in Table A.2.

A.2 PLUME FLOWFIELD ANALYSIS

Two plume flow fields for the orbiter engines were generated for use in the preliminary analysis. These were: (1) the engine operating at 283,000 feet

*McBride, Bonnie, and S. Gordon, "Preliminary Description of CEC, A Computer Program for Calculation of Chemical Equilibrium Compositions with Applications," NASA-Lewis Research Center, Cleveland, Ohio, May 1961.

with the vehicle Mach number effect on the plume shape considered, and (2) the engine exhausting into quiescent conditions at 283,000 feet. The latter plume (which is considerably larger in size than the former) will be used to establish an upper bound on the booster impingement data and will be included in the final report of the subject contract.

All plume calculations were performed assuming the engine to be operating at full thrust (engine chamber pressure = 3000 psia). The coordinates r, x were made non-dimensional with respect to the engine exit radius. Thus, the single and equivalent multiple nozzle flow fields are obtained by multiplying the field coordinates by the appropriate engine exit radius.

The plumes were generated using two method-of-characteristics computer programs.* The calculations were initiated at the nozzle exit plume with a start line based on a one-dimensional nozzle solution. Real gas effects were included in the nozzle solution with the flow angle distributed across the exit plane. Input data included: (1) nozzle area ratio of 200/1; (2) lip angle = 6.6 degrees and (3) the nozzle external flow condition M = 12.08 at an altitude of 283,000 feet.

Assumptions used in the calculations are: (1) the flow is inviscid and axially symmetric; (2) the flow is rotational; (3) the oxidizer-to-fuel ratio (O/F) is constant; and (4) the flow is non-continuum for Knudsen numbers greater than "1/collision number." A lip shockwave (See Figs. A-1 through A-12) was considered in the analysis. This shockwave is the result of the nozzle flow being underexpanded at the exit plane. The shockwave follows the plume boundary over the region of interest.

---

*Prozan, R. J., "Development of a Method-of-Characteristics Solution for the Supersonic Flow of an Ideal, Frozen or Equilibrium Reacting Gas/Mixture, LMSC/HREC D162220-III, May 1970.

Smith, S. D., and A. W. Ratliff, "User's Manual – Variable O/F Method-of-Characteristics Program for Nozzles and Plume Flow Analysis," LMSC/HREC D162220-I, May 1970.

At the nozzle exit plane, the primary constituents of the flow are H_2O (gas) and H_2(gas). The mixture percent composition is 75.6% H_2O and 24.4% H_2 (global molecular weight of 14.112 lb_m/lb_m-mole). Based on a consideration of the primary constituents, H_2O and H_2. The flow approaches a chemically frozen condition at a pressure of 0.4 atmospheres which corresponds to a Mach number of 4.2. For the engine used in the current study this condition would occur inside the nozzle. After the flow approaches the chemically frozen condition, the isentropic exponent, gamma, then becomes a function only of temperature. Because of the lack of thermochemical data at low temperatures, those regions of the flow field having Mach numbers greater than 3.392 were treated as an ideal gas at a molecular weight of 14.112 lb_m/lb_m-mole and an isentropic exponent of 1.3347.

Non-gaseous forms of the mixture constituents were not considered in the thermochemical calculations. The ability of the NASA-Lewis (CEC) Thermochemical program to handle liquids and solids is restricted by the lack of thermochemical data for non-gaseous species. Because condensed species might occur in the plume, vapor pressures for the composition were examined to determine where incipient condensation might exist. Conditions are not favorable for the condensation of H_2O or H_2 over the range of interest for the current problem. This is due to the high combustion pressure which results in a high static pressure in the plume which delays the on-set of condensation.

The flow fields for the respective plumes are described by the streamline distribution shown in Figs. A-1 and A-7. The mass flow associated with each streamline is indicated with the mass flow given as a percentage of the total mass flow in the plume. The plume flow fields are mapped by contour plots of Mach number, local static pressure, temperature, density, and pitot total pressure as shown on Figs. A-2 through A-6 and A-8 through 12, respectively.

Knudsen number calculations were made at various points in the plume flow field to determine if the flow were in the free molecular flow regime.

Temperature gradients indicate that the flow is well within the continuum flow regime.

To consider the effects of the engine ignition transients the local flow properties should be adjusted by the ratio of the chamber pressure at time, t, in the ignition sequence to the chamber pressure of 3000 psia at full thrust conditions.

Table A-1

OPERATING CHARACTERISTICS FOR THE ORBITER MAIN STAGE ENGINE

Engine Manufacturer: Rocketdyne

Preburner	Oxidizer: O_2	Engine Parameters
	Fuel: H_2	$A/A^* = 200/1$
		$O/F = 6.0$
		Effective equivalence ratio = 1.3227 (main burner)
		$P_c = 3000$ psia
		$\theta_{exit} = 6.6$ degrees
Mainburner	Oxidizer: O_2	
	Fuel: H_2, H_2O	

Table A-2

THERMOCHEMICAL DATA USED IN THE FLOW FIELD ANALYSIS

O/F	S	Real Gas Properties V	R	Gamma	T	P
6.0	($ft^2/sec^2/^oR$)	(ft/sec)	($ft/sec^2/^oR$)		(^oR)	(psf)
	.00000					
		.00000	.36525+04	.11486+01	.64926+04	.43192+06
		.50376+04	.36182+04	.11501+01	.60984+04	.24802+06
		.82982+04	.35673+04	.11598+01	.53730+04	.86405+05
		.97039+04	.35455+04	.11716+01	.48996+04	.43192+05
		.12694+05	.35239+04	.12174+01	.33822+04	.43192+04
		.13943	.35234+04	.12434+01	.25038+04	.86405+03
		.14347+05	.35234+04	.12562+01	.21798+04	.43192+03
		.15032+05	.35234+04	.12877+01	.15696+04	.86342+02
		.15289+05	.35234+04	.13020+01	.13230+04	.43171+02
		.15680+05	.35234+04	.13264+01	.90720+03	.86765+01
		.15823+05	.35234+04	.13347+01	.75600+03	.52324+01
	.21512+05					
		.00000	.38930+04	.11132+01	.53046+04	.14401+04
		.46618+04	.38367+04	.11115+01	.50976+04	.83845+03
		.78338+04	.37323+04	.11108+01	.47088+04	.28802+03
		.92154+04	.36728+04	.11133+01	.44640+04	.14390+03
		.12313+05	.35409+04	.11695+01	.35352+04	.14390+02
		.13676+05	.35239+04	.12334+01	.27018+04	.29627+01
		.14122+05	.35234+04	.12482+01	.23616+04	.14390+01
		.14906+05	.35234+04	.12812+01	.16866+04	.29627+00
		.15158+05	.35234+04	.12946+01	.14490+04	.14390+00
		.15587+05	.35234+04	.13210+01	.10008+04	.29627-01
		.15748+05	.35234+04	.13304+01	.83520+03	.14390-01

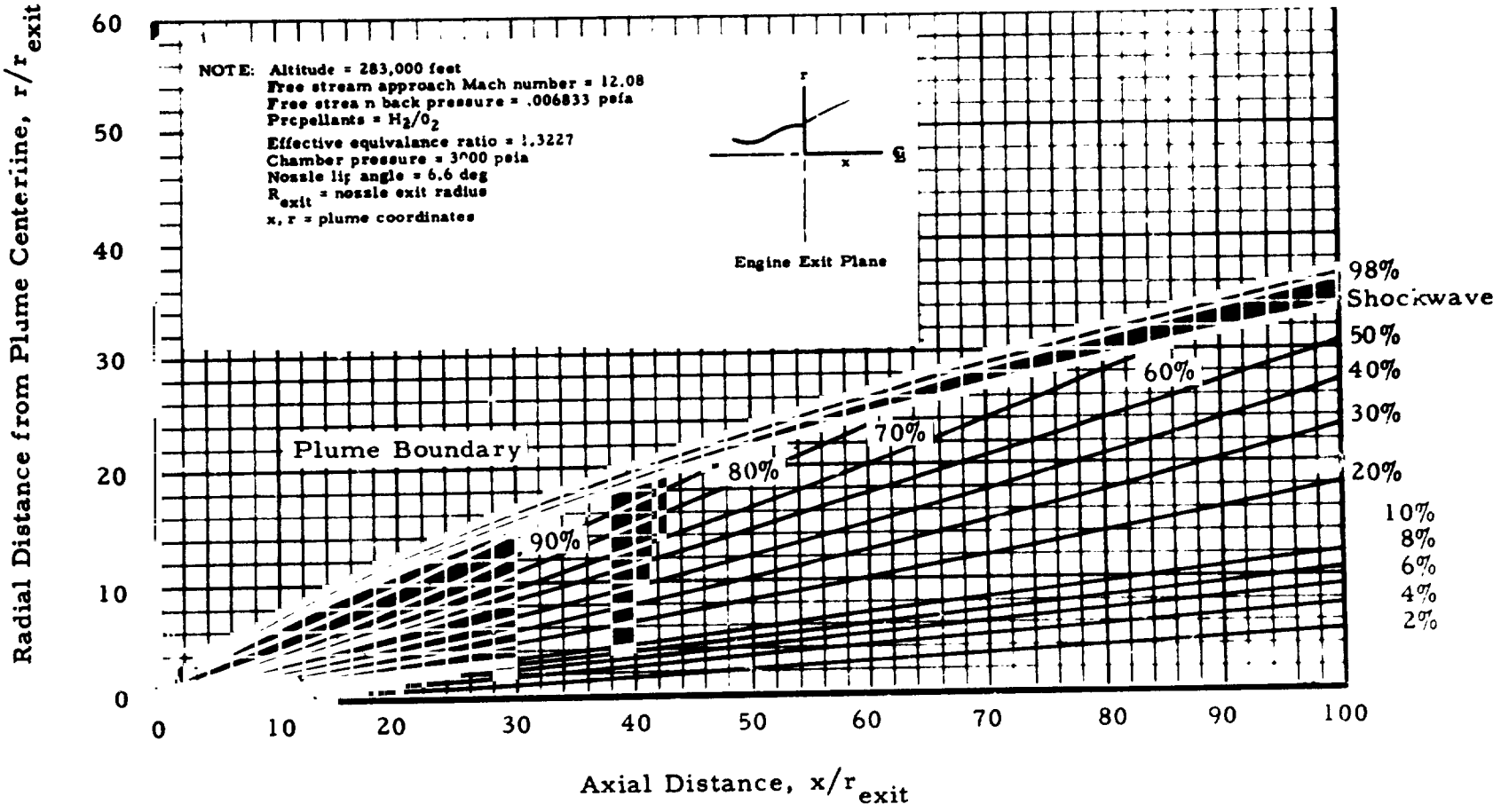

Fig. A-1 - Distribution of Mass Flow Rate in the Orbiter Main Stage Engine Plume with Hypersonic Plume External Flow Conditions

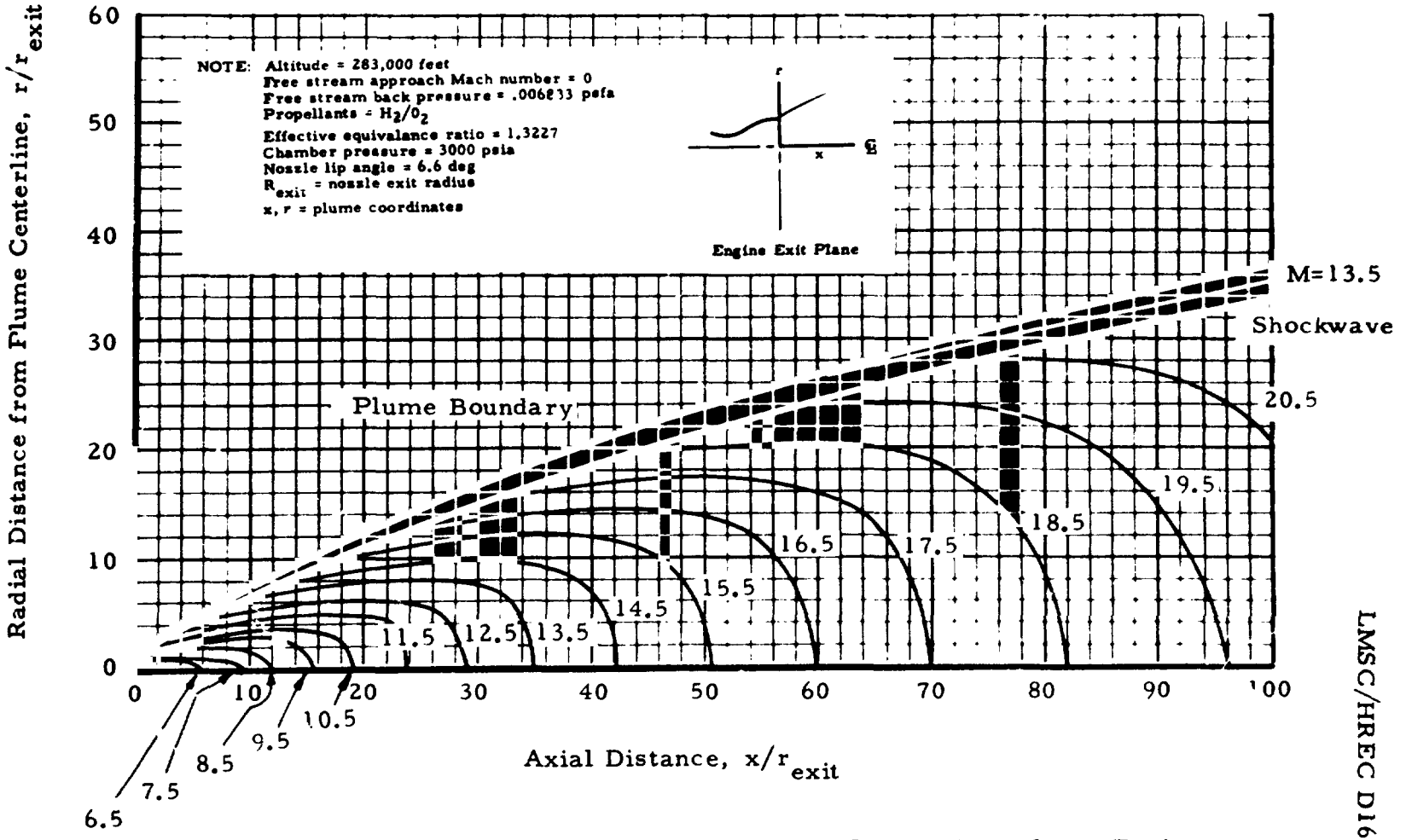

Fig. A-2 - Local Mach Number Contour Map for the Orbiter Main Stage Engine Plume with Hypersonic Plume External Plume Flow Conditions

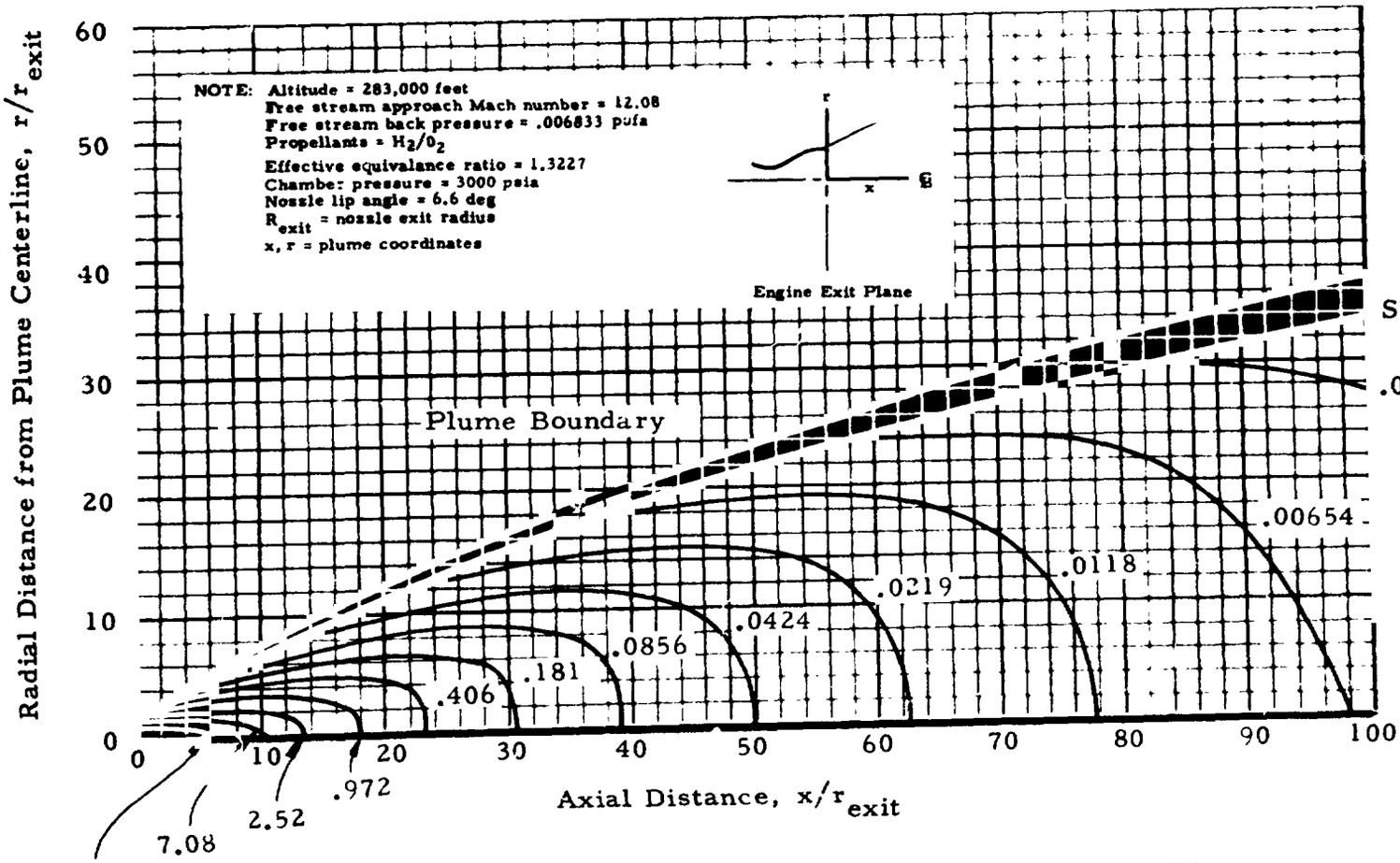

Fig. A-3 - Static Pressure Contour Map for the Orbiter Main Engine Plume with Hypersonic Plume External Flow Conditions

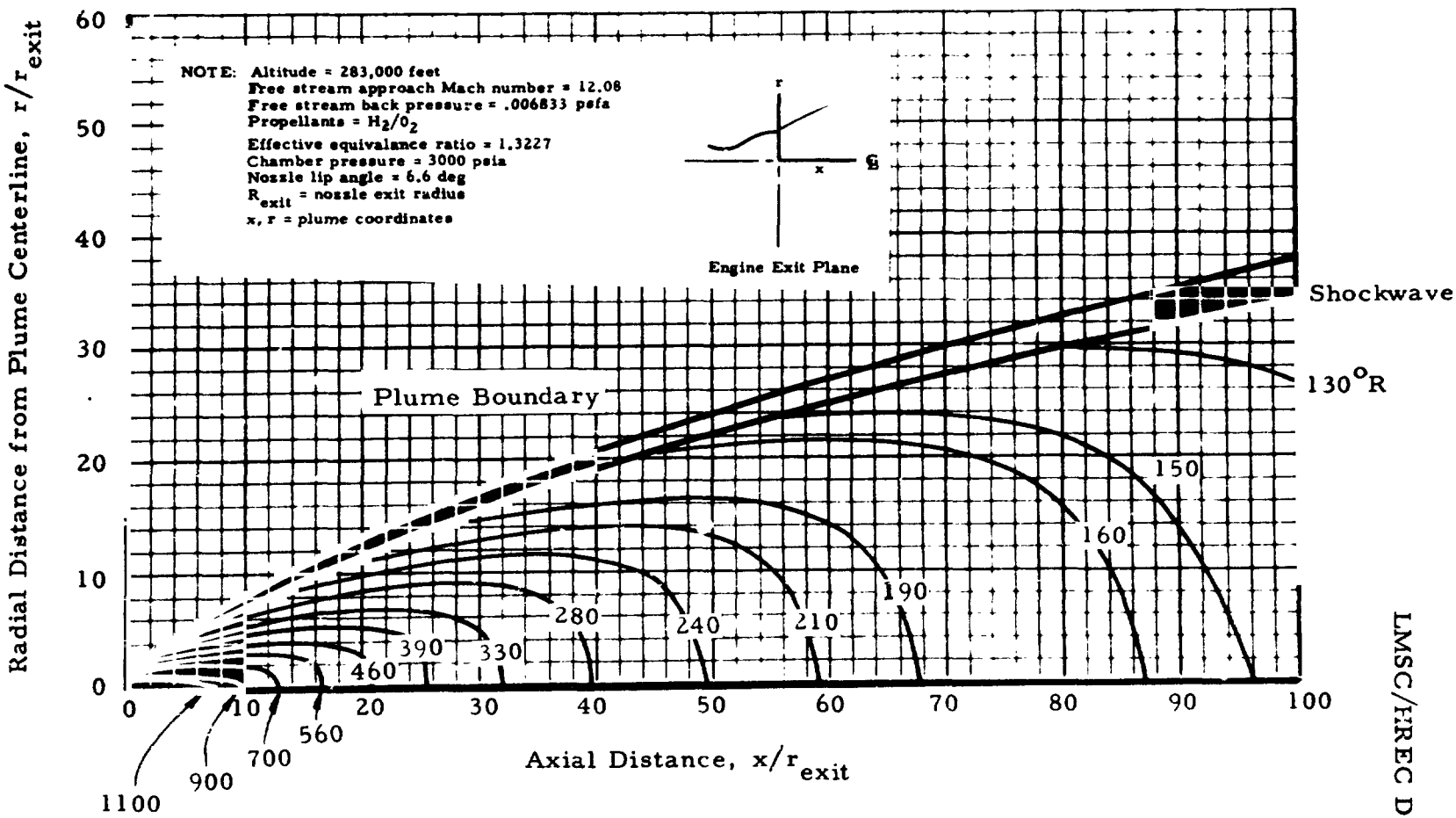

Fig. A-4 - Static Temperature Contour Map of the Orbiter Main Stage Engine Exhaust Plume with Hypersonic Plume External Flow Conditions

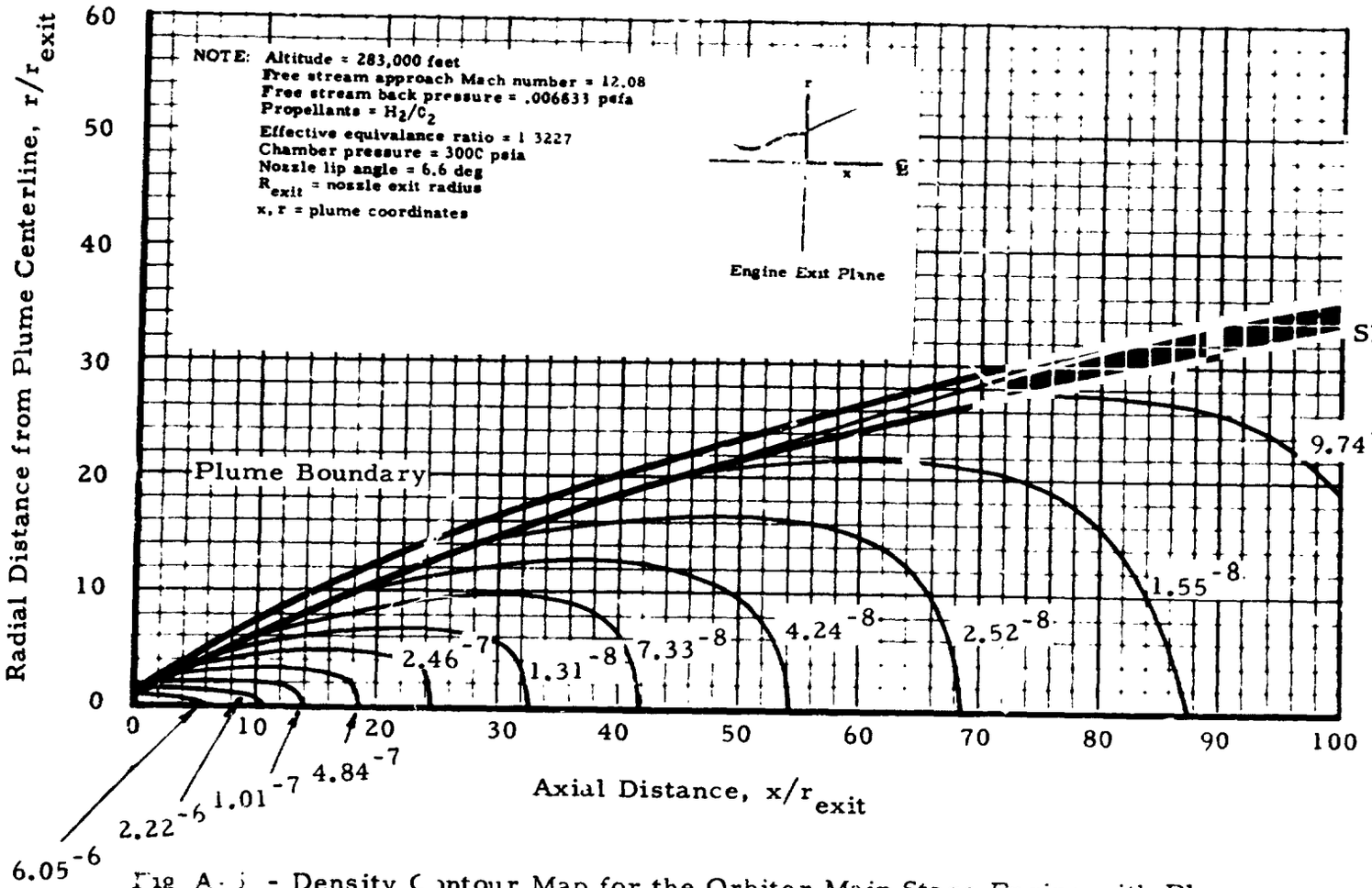

Fig A-3 - Density Contour Map for the Orbiter Main Stage Engine with Plume Hypersonic Plume External Flow Conditions

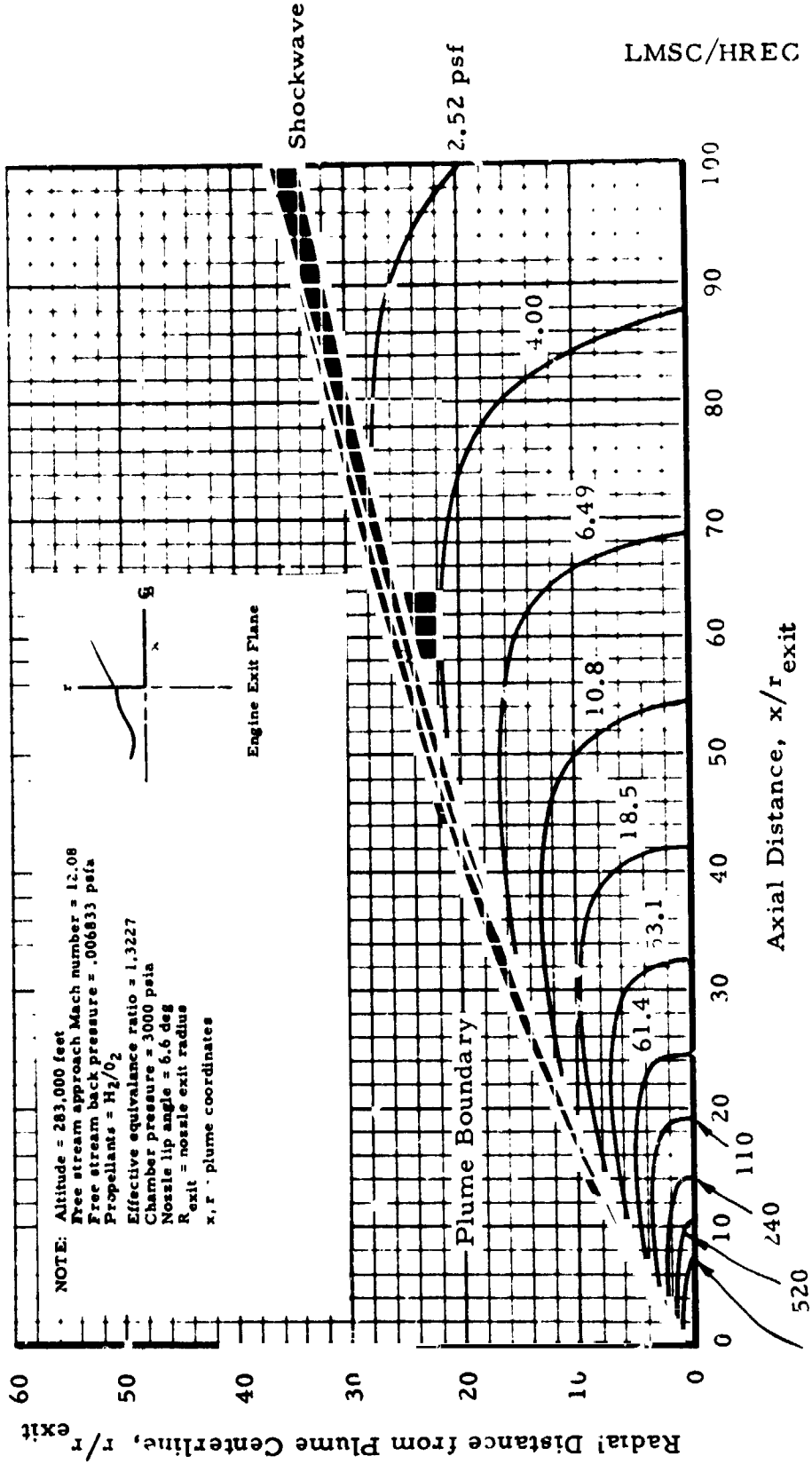

Fig. A-6 - Pitot Total Pressure Contour Map of the Orbiter Main Stage Engine Exhaust Plume with Hypersonic Plume External Flow Conditions

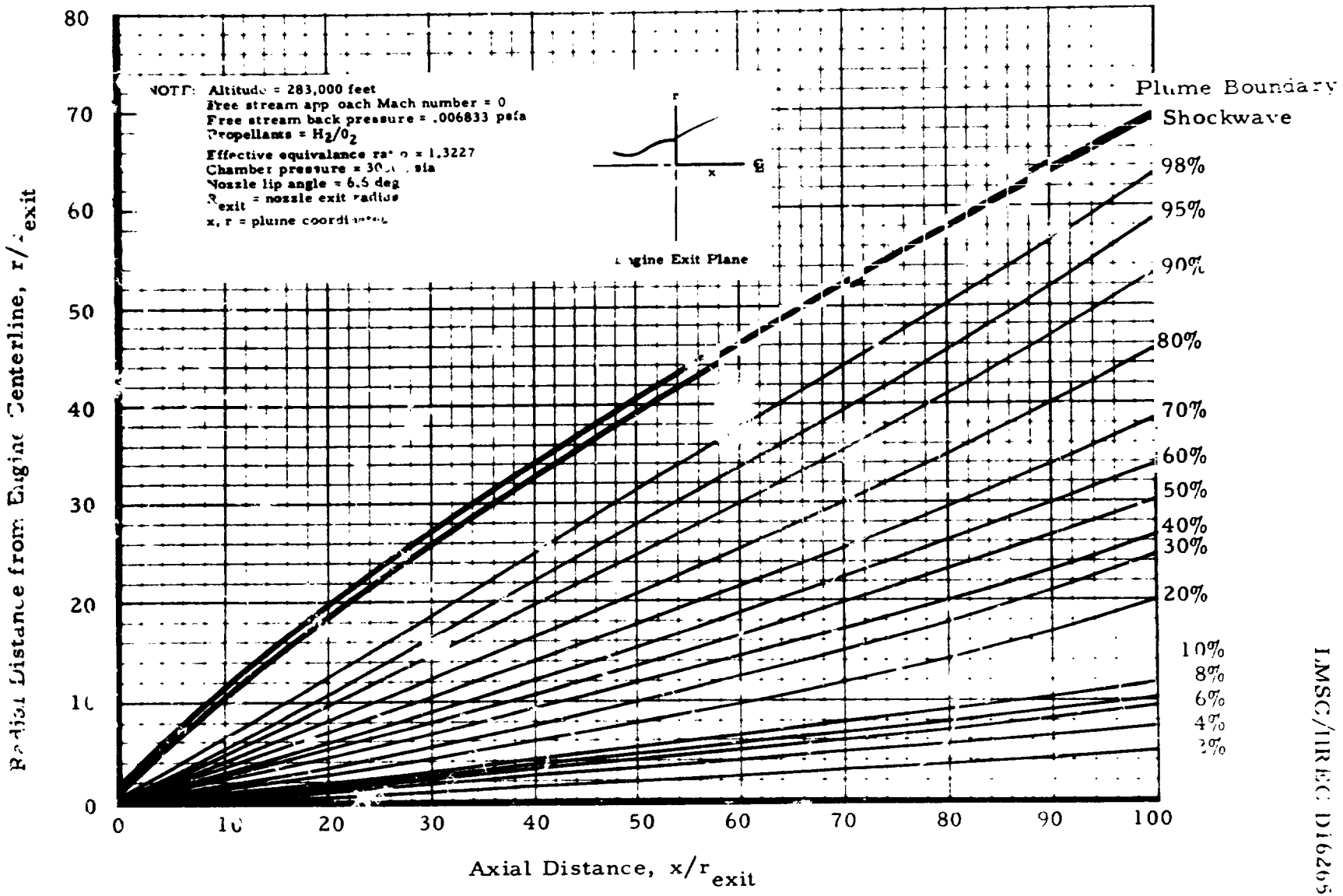

Fig. A-7 - Mass Flow Rate Distribution for the Orbiter High Altitude Plume Exhausting into Quiescent Conditions

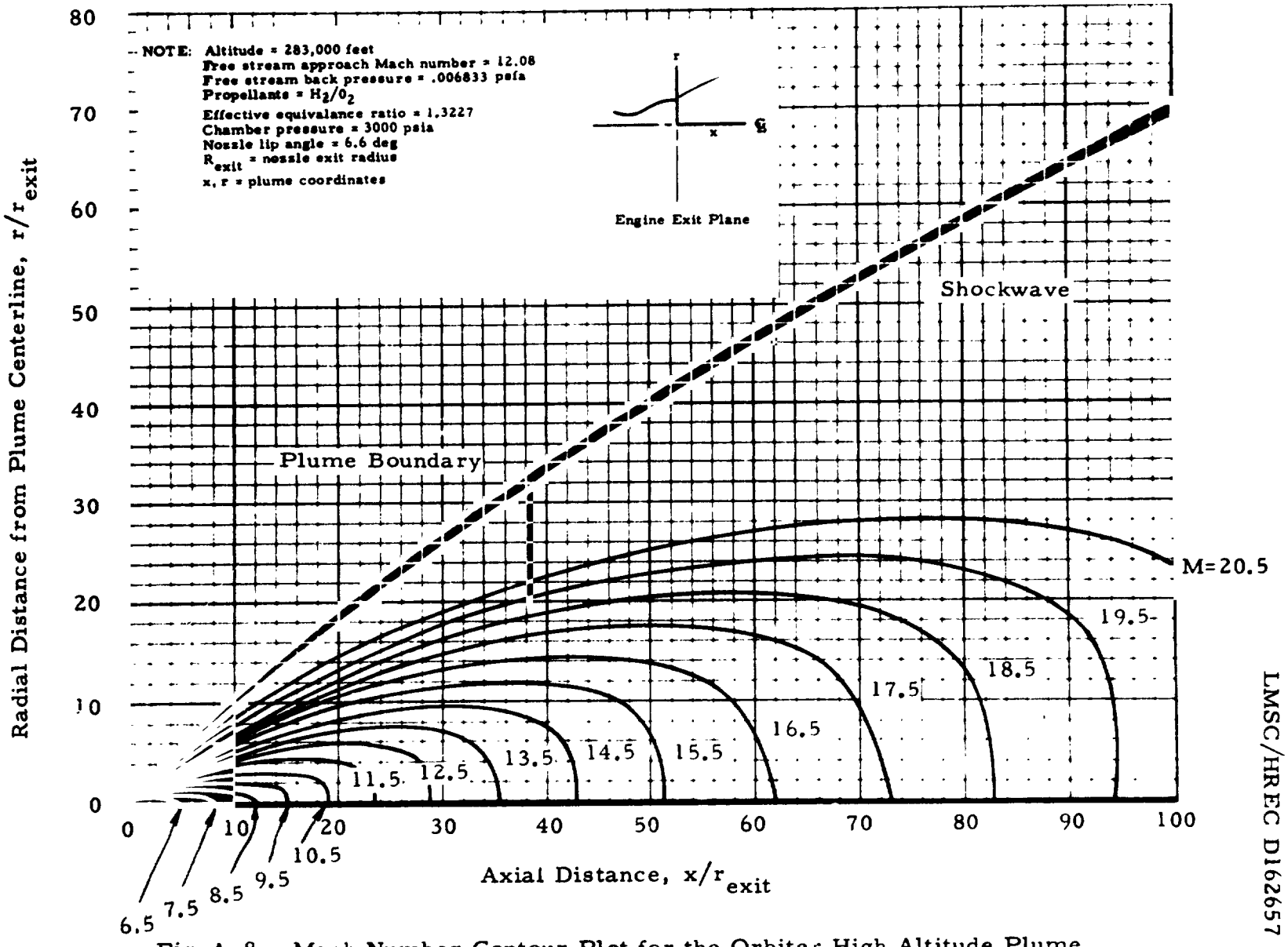

Fig. A-8 - Mach Number Contour Plot for the Orbiter High Altitude Plume Exhausting into Quiescent Conditions

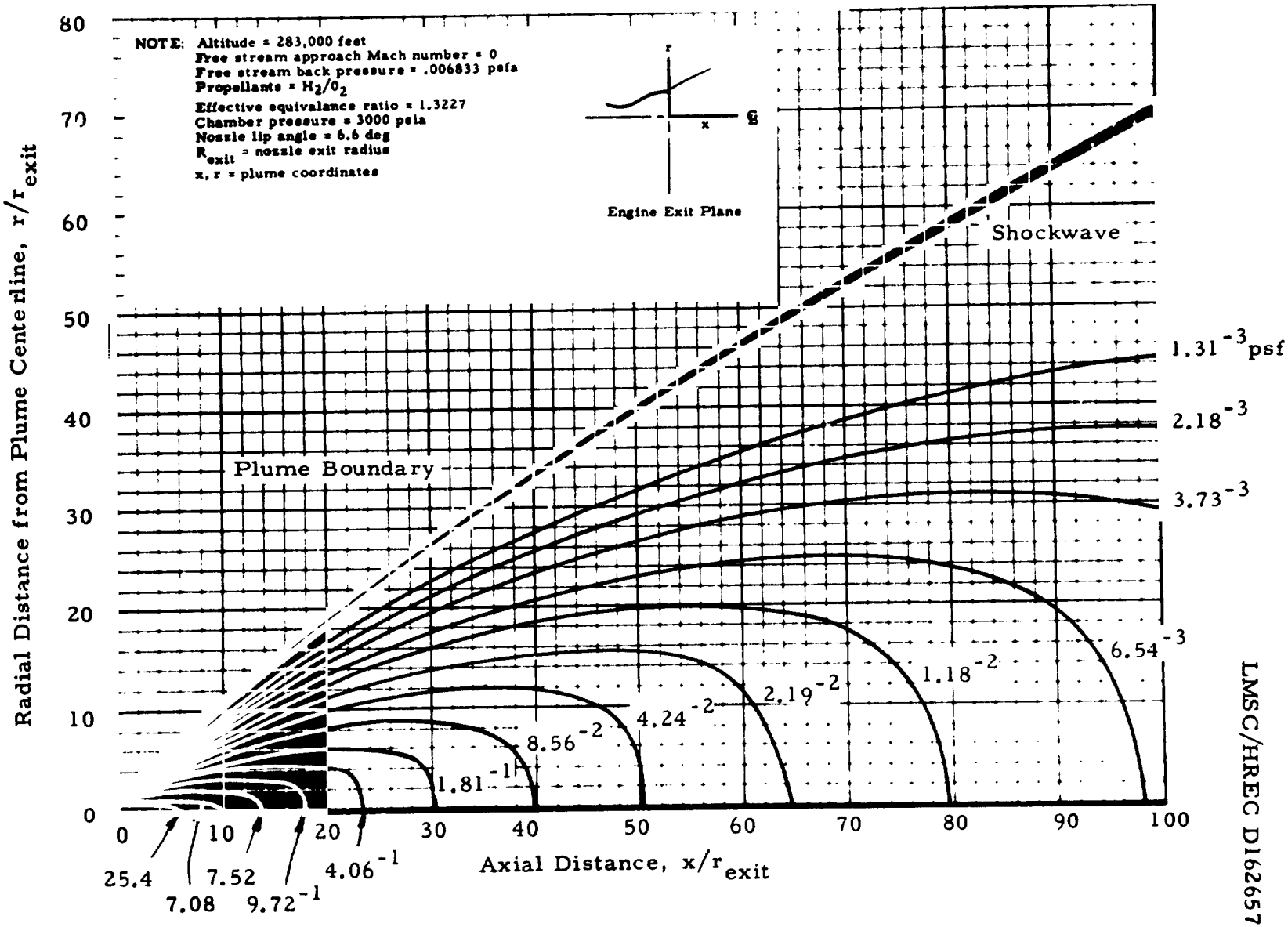

Fig. A-9 - Static Pressure Contour Map for a High-Altitude Orbiter Plume Exhausting into Quiescent Conditions

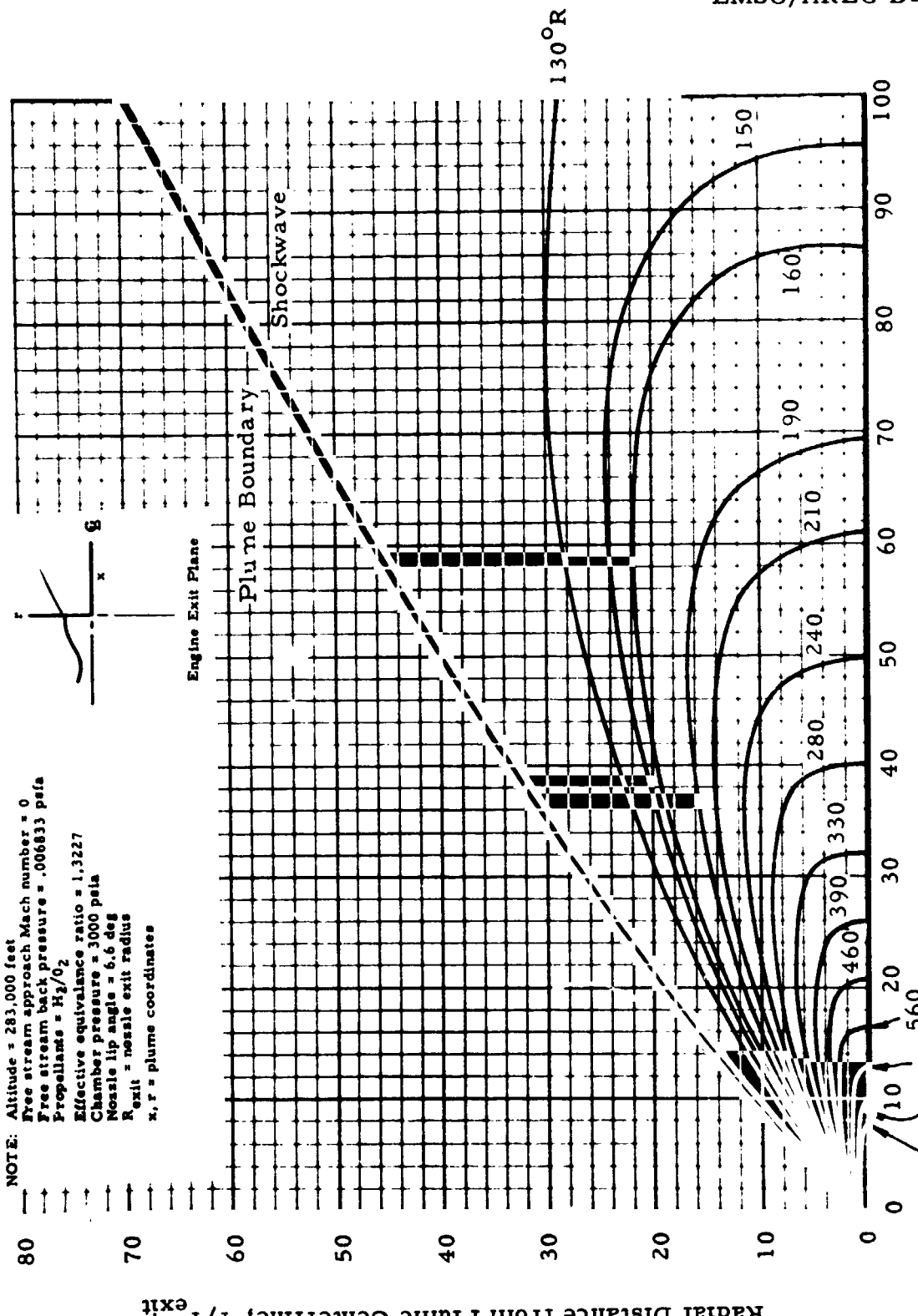

Fig. A-10 - Static Temperature Contour Map for the Orbiter High Altitude Plume Exhausting into Quiescent Conditions

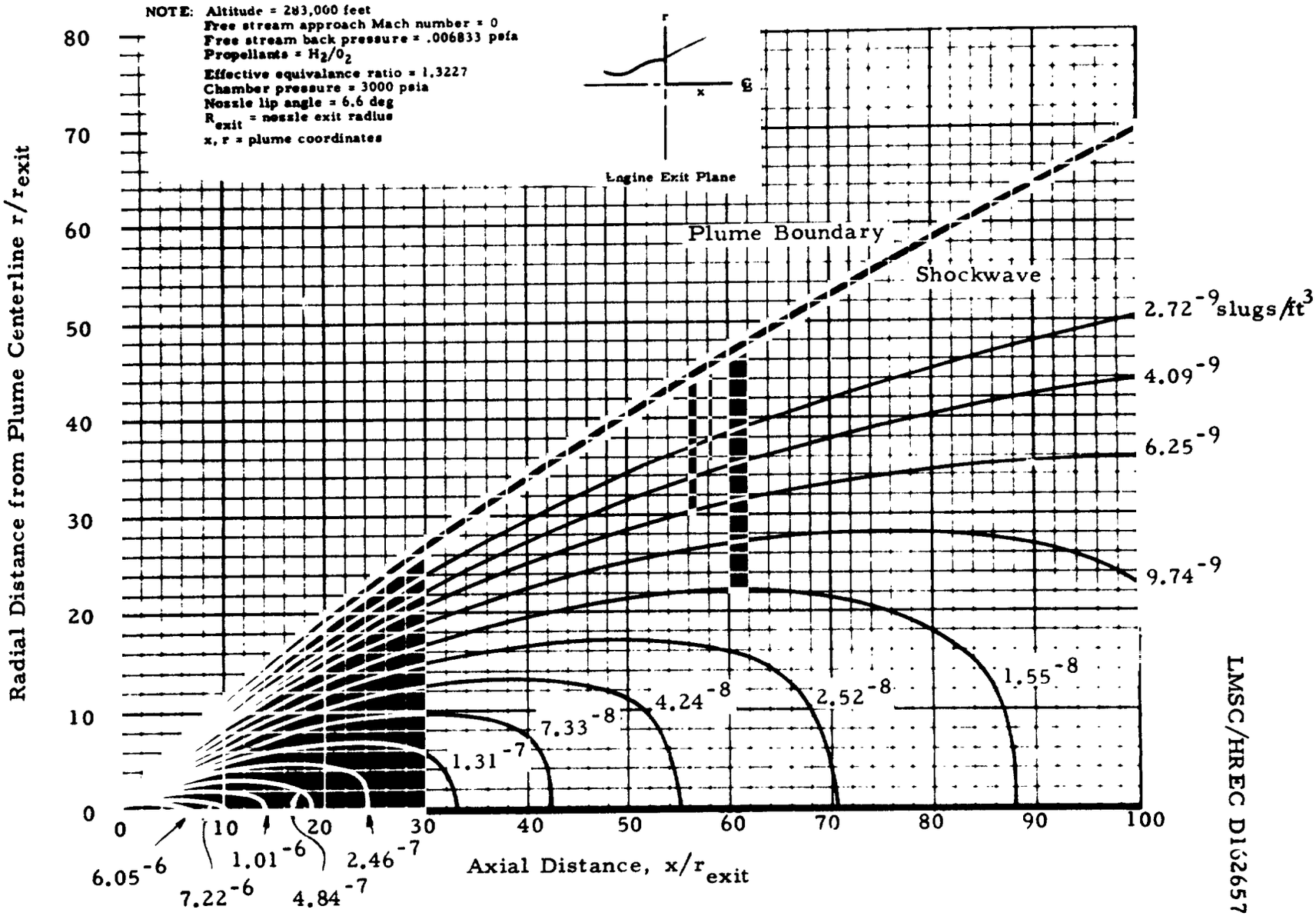

Fig. A-11 - Density Contour Map for the Orbiter Engine Plume Exhausting into Quiescent Conditions

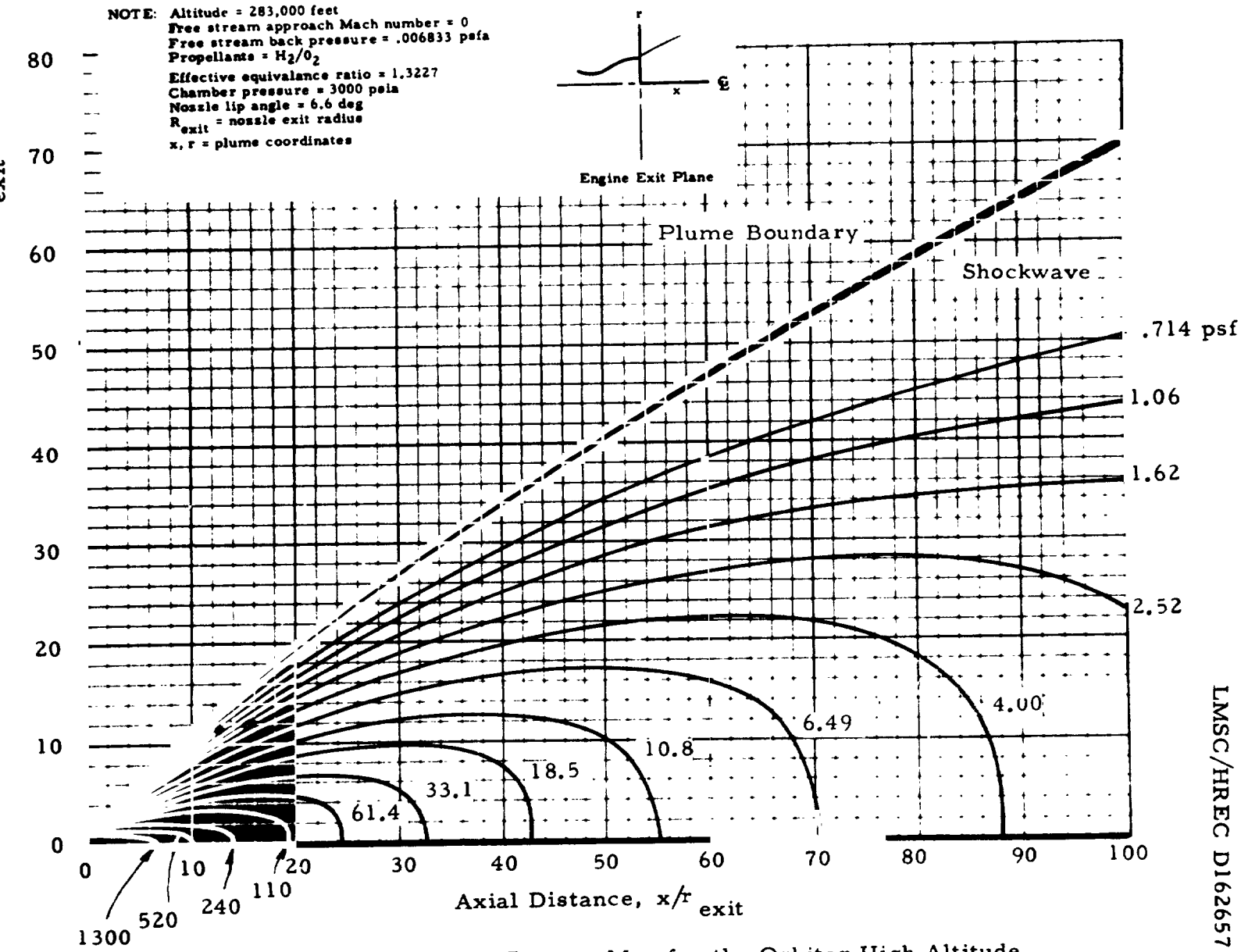

Fig. A-12 - Pitot Total Pressure Contour Map for the Orbiter High Altitude Plume Exhausting into Quiescent Condition

Appendix 3

WING GEOMETRY DEVELOPMENT

NOMENCLATURE

Symbols

c	chord, in.
dL	differential length vector
f	airfoil cross section function
i, j, k	unit vectors subshape system
$\bar{n}$	unit normal
$\hat{n}x, \hat{n}y, \hat{n}z$	defined in text
r	root chord, in.
s	span, in.
S	surface function
t_r	taper ratio (wing tip chord/root chord)
x, y, z	coordinates of point in local subshape system in.
x', y', z'	local leading edge coordinate system (normalized)

Greek

α	angle between normal to surface and y coordinate
β	defined in text
θ	sweep of y' = constant line
θ_s	leading edge sweep angle

Appendix B

INTRODUCTION

A comprehensive plume impingement program* has been developed under several support contracts. The impingement analyses conducted to date were mainly concerned with orbiter vehicles and the library of coded subshapes (conic sections, rectangular, triangular and circular flat plates) were adequate to describe the vehicle's geometry. Under Contract NAS9-11156, however, it was necessary to describe airfoil subshapes in order to accurately simulate the Space Shuttle vehicle geometry.

This Appendix describes the theoretical approach to this airfoil description. The airfoil considered for this study was NACA 0012-64 which is symmetrical. The subshape calculation has been coded, however, to permit the use of any airfoil as long as there is no spanwise variation in the normalized contour.

DISCUSSION

Consider the airfoil shown in Fig. B-1. Let x' = spanwise location normalized by the span; y' = chordwise distance aft of leading edge normalized by the chord; z' = airfoil thickness normalized by the chord. The airfoil cross section equation is

$$S\ (x', y', z') = z' - f(y') = 0$$

*Wojciechowski, C. J. and A. W. Ratliff, "Study of High Altitude Plume Impingement," LMSC/HREC D149118, August 1969.

from which it follows that

$$\nabla S = - \frac{\partial f}{\partial y'} \bar{j} + \bar{k} \quad .$$

It can be seen however that

$$\frac{\partial f}{\partial y'} = \tan(\alpha - \frac{\pi}{2}) = - \cot\alpha \, .$$

Consider the change of variables

$$x = s\, x'; \; y = x \tan\theta_s + r \left[1 - (1 - t_r) \frac{x}{s}\right] y'; \; z = r \left[1 - (1 - t_r) \frac{x}{s}\right] z'$$

where

$$c = r \left[1 - (1 - t_r) \frac{x}{s}\right].$$

Now

$$\left.\frac{dy}{dx}\right|_{y' = \text{const}} = \tan\theta = \tan\theta_s - \frac{r}{s}(1 - t_r) y'$$

and

$$\left.\frac{dz}{dx}\right|_{y' = \text{const}} = - \frac{r}{s}(1 - t_r) z' = \tan\beta \, .$$

From the chain rule $\frac{\partial S}{\partial \xi_j} = \frac{\partial S}{\partial \xi_i'} \frac{\partial \xi_i'}{\partial \xi_j}$

where

$$\frac{\partial x'}{\partial x} = \frac{1}{s}; \; \frac{\partial y'}{\partial x} = - \frac{\tan\theta}{c}; \; \frac{\partial z'}{\partial x} = - \frac{\tan\beta}{c}$$

$$\frac{\partial x'}{\partial y} = 0; \quad \frac{\partial y'}{\partial y} = \frac{1}{c}; \quad \frac{\partial z'}{\partial y} = 0$$

$$\frac{\partial x'}{\partial z} = 0; \quad \frac{\partial y'}{\partial z} = 0 \quad ; \quad \frac{\partial z'}{\partial z} = \frac{1}{c} \ .$$

The partial derivatives of S with respect to x, y, z are therefore;

$$\frac{\partial S}{\partial x} = - \frac{\cot\alpha}{c} \tan\theta - \frac{\tan\beta}{c}$$

$$\frac{\partial S}{\partial y} = \frac{\cot\alpha}{c}$$

$$\frac{\partial S}{\partial z} = \frac{1}{c} \ .$$

The normal to the surface is

$$\bar{n} = \frac{\tilde{n}_x \bar{i} + \tilde{n}_y \bar{j} + \tilde{n}_z \bar{k}}{\sqrt{\tilde{n}_x^2 + \tilde{n}_y^2 + \tilde{n}_z^2}}$$

where

$$\tilde{n}_x = - (\cos\alpha \tan\theta + \sin\alpha \tan\beta)$$

$$\tilde{n}_y = \cos\alpha$$

$$\tilde{n}_z = \sin\alpha \ .$$

Elemental Area

Taking the differential of the transformation yields

$$dx = s\,dx'; \quad dy = s(\tan\theta + \tan\beta)\,dx' + c\,dy'; \quad dz = s\tan\beta\,dx' + c\,dz' .$$

So that a differential length vector may be written as

$$d\bar{L} = s\,dx'\,\bar{i} + + \left\{ s\tan\theta\,dx' + c\,dy' \right\}\,\bar{j} + (s\tan\beta\,dx' + c\,dz')\,\bar{k} .$$

If a step is taken in dx' (dy' = 0)

$$d\bar{L}_1 = s\left[\bar{i} + \tan\theta\,\bar{j} + \tan\beta\,\bar{k}\right]dx' + c\,dz'\,\bar{k} .$$

If a step is taken in dy' (dx' = 0)

$$d\bar{L}_2 = c\,dy'\,\bar{j} + c\,dz'\,\bar{k} .$$

To ensure that these differential steps are taken along the surface it is necessary that

$$\bar{n} \cdot d\bar{L}_1 = \bar{n} \cdot d\bar{L}_2 = 0 .$$

But

$$\bar{n} \cdot d\bar{L}_1 = dz' = 0$$

so that

$$d\bar{L}_1 = s\left[\bar{i} + \tan\theta\,\bar{j} + \tan\beta\,\bar{k}\right]dx' .$$

It was found that the calculation of dz' from $\bar{n} \cdot d\bar{L}_2$ suffered from numerical inaccuracies. The quantity dz' is therefore found directly from the function and

$$d\bar{L}_2 = c\left(\bar{j} + \frac{dz'}{dy'}\,\bar{k}\right) dy' \ .$$

The differential area is

$$d\bar{A} = d\bar{L}_1 \times d\bar{L}_2$$

whence

$$\frac{d\bar{A}}{s\,c\,dx'\,dy'} = \left[\bar{i} + \tan\alpha\,\bar{j} + \tan\beta\,\bar{k}\right] \times \left[\bar{j} + \frac{dz'}{dy'}\,\bar{k}\right]$$

$$\frac{d\bar{A}}{s\,c\,dx'\,dy'} = \left[\tan\theta\,\frac{dz'}{dy'} - \tan\beta\right]\bar{i} - \frac{dz'}{dy'}\,\bar{j} + \bar{k}$$

and finally

$$dA = \left[\left\{\tan\theta\,\frac{dz'}{dy'} - \tan\beta\right\}^2 + \left\{\frac{dz'}{dy'}\right\}^2 + 1\right]^{1/2} s\,c\,dx'\,dy' \ .$$

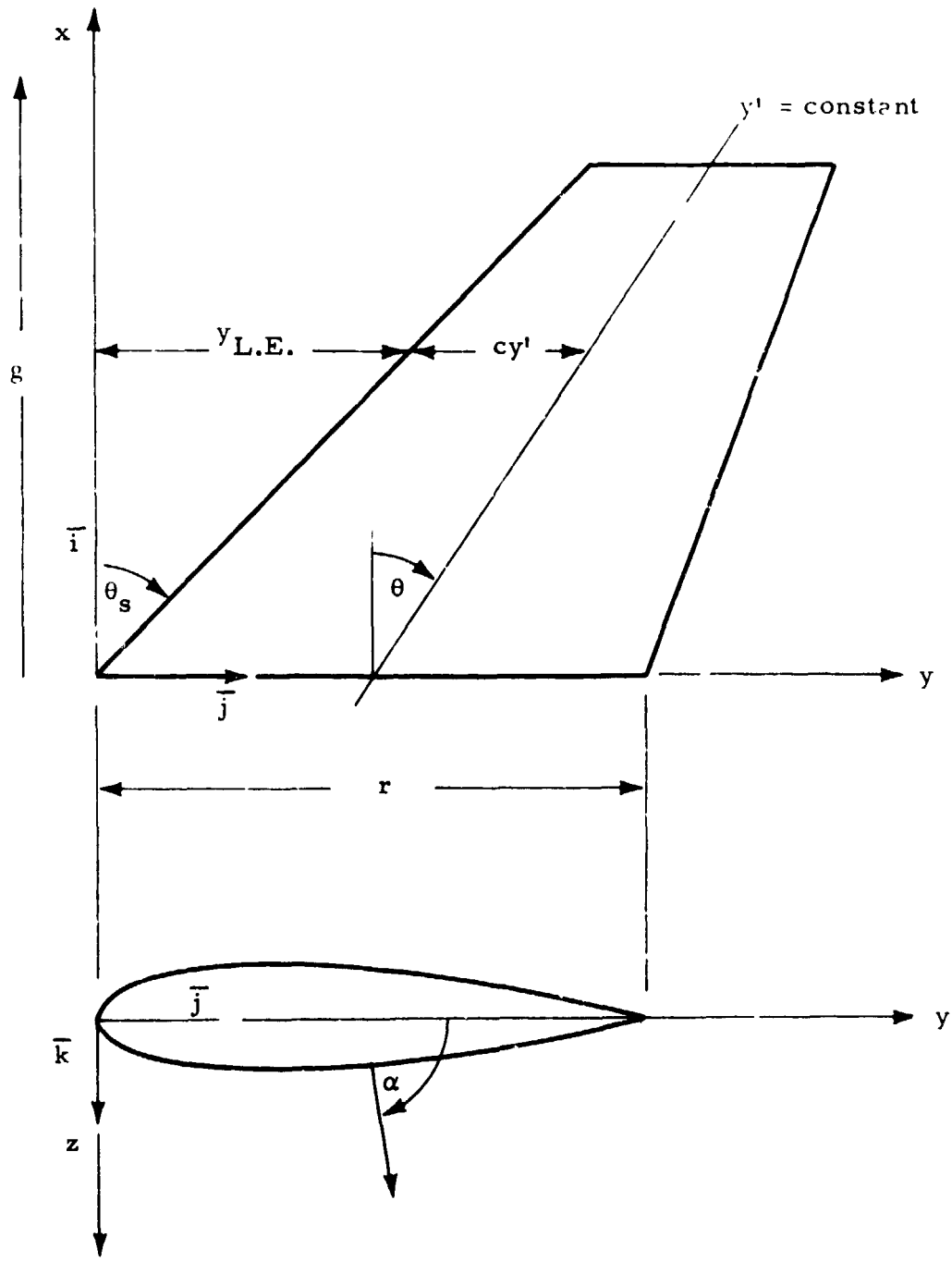

Fig. B-1 - Schematic of Airfoil Geometry

Appendix C

BOOSTER PLUME IMPINGEMENT ANALYSIS

Appendix C

The staging sequence of the Space Shuttle vehicle will result in those exhaust plumes of the orbiter main stage engines impinging on the booster surfaces. Calculations were made to determine the forces and the resulting moments imposed on the booster due to the orbiter exhaust plume environment.

The impingement analysis mapped the force and moment distribution on an area to sufficiently analyze the expected separation trajectories. The data include the effect of roll, pitch and yaw maneuvers for the booster and is presented in graphical form.

C.1 PROBLEM DESCRIPTION

The geometrical orientation for the Shuttle arrangement is shown in Fig. C.1. A reference coordinate system is located at the nose of the booster on the vehicle centerline. All forces and moments presented are referenced to this point. A simulated multiple nozzle was used to represent the orbiter main stage engines. The simulated nozzle has the same mass flow rate as the orbiter engine cluster and approximately the same plume shape.

In the plume impingement analysis, the various components of the booster were represented by four (4) basic subshapes (Fig. C.2). These were: (1) a cylinder for the upper portion of the fuselage; (2) flat plates for the lower sides of the fuselage; (3) a conical nose and airfoil shape NACA 0012-64 for the wing, vertical and horizontal tails.

C.2 DEFINITION OF THE PLUME IMPINGEMENT CHARACTERISTICS

The impingement characteristics were calculated by Lockheed's Plume Impingement Computer Program*. Basically, the procedure for obtaining the impingement characteristics is as follows. The vehicle composite shape and the particular motor are located with respect to the reference coordinate system. The composite shape is then represented by a series of geometrically simple subshapes (each with its own local coordinate system). These subshapes are further divided into smaller incremental areas. Local flow conditions on a given body are obtained by locating the centroid of each elemental area in the free plume** from a search of the plume flow field which is stored on magnetic tape. The flow properties thus obtained are assumed to act uniformly over the elemental area.

The body local flow regimes were determined by the value of the local Knudsen number. In this analysis, continuum flow was assumed to exist for Knudsen numbers less than 0.01; transitional flow exists for Knudsen numbers between 0.01 and 10.0; and Knudsen numbers greater than 10.0 define the "free molecular flow" regime. The characteristics lengths used in the Knudsen number calculations were a representative dimension (element area dimension) of the body in question so that the elemental area local flow regime is determined by comparing the mean free molecular path of the local plume to the body dimension. The analysis assumed the surfaces to be of an infinitesimally small thickness.

---

* Wojciechowski, C. J., and A. W. Ratliff, "Study of High-Altitude Impingement," LMSC/HREC D149118, August 1969.

** Prozan, R. J., "Development of a Method-of-Characteristics Solution for the Supersonic Flow of an Ideal, Frozen or Equilibrium Reacting Gas Mixture," LMSC/HREC D162220-III, May 1970.

** Smith, S. D., and A. W. Ratliff, "User's Manual-Variable O/F Method-of-Characteristics Program for Nozzles and Plume Flow Analysis," LMSC/HREC D162220-I, May 1970.

In the numerical integration scheme, the cylindrical portion of the fuselage and the conical nose section were divided in rings of 50.0 inches in increment with each ring further subdivided into 10.0-degree radial increments. All wing sections were divided into approximately 40.0 inch increments in the span direction. As discussed in Appendix B, a cosine distribution function is used to distribute the data points in the chord direction. This scheme biases the point distribution toward the wing-leading edge where largest gradients in surface curvature occur. Twenty (20) increments in the chord direction were used on the wing and horizontal tail surfaces while thirty (30) increments were used on the vertical tail surfaces where the highest values of heating rates and impingement force distribution occur. Uniform flow was assumed to exist over each elemental area of the respective surfaces with vacuum conditions considered to exist on the surfaces not exposed to the engine exhaust plume. Characteristics dimensions used in the Knudsen number calculations to determine the surface local flow regime were the element area dimensions and the diameters and lengths of the conical shaped bodies. Also, a representative plume molecular diameter of $.1 \times 10^{-6}$ in. was used in the Knudsen number calculations. It should be noted that the force integration results reflect the assumptions used to generate the engine exhaust plume.*

C.3 PLUME IMPINGEMENT FLOW REGIMES

In the continuum regime, the local impact pressures were calculated from a modified Newtonian impact theory** as given by

$$P_{imp} = P_{\infty} \left(1 + \frac{\gamma}{2} K M_n^2 \sin^2\alpha\right) \qquad (C.1)$$

with K given by

$$K = C_{P_s} \left(.814 + \frac{6.88}{\alpha^{4/5}}\right) . \qquad (C.2)$$

*Prozan, and Smith, LMSC/HREC D162220-I and LMSC/HREC D162220-III, May 1970.

**Buck and McLaughlin, ASP-TDR-63-552, August 1963 (Confidential).

Fundamental Newtonian theory assumes that the force felt by the body is due to the time rate of change of the normal momentum and is independent of the angle of incidence of the body surface so that there is no transfer of the tangential momentum. The parameter K is included to account for the higher pressures noted experimentally* for small-incidence angles on flat plates. For this analysis, K ranged from 1.8 to 6.0 and was set to 6.0 for local incidence angles less than 3 deg. The forces and moments were then obtained by numerically integrating the local impact pressure distribution over the body.

The free molecular flow regime is characterized by the fact that the local properties on the body depend only upon collisions of the gas molecules with the body surface. A Lockheed/Huntsville-developed impingement program** assumes environmental equilibrium so that a Maxwellian-type flow exists and the local flow properties are calculated from kinetic theory and Maxwell's law of distribution of molecular velocities. The local force on the elemental area is obtained by computing the forces produced by the incident and reflected molecules and adding them. The force is given by

$$\frac{dF}{dA} = \frac{\xi}{2\beta}\left\{\frac{1}{\sqrt{\pi}}(ke + \ell\gamma + t\eta)\left[\gamma S^2\sqrt{\pi}(1 + \operatorname{erf}(\gamma S) + Se^{-\gamma^2 S^2}\right]\right.$$

$$\left. + \frac{\ell}{2}(1 + \operatorname{erf}(\gamma S) + \frac{\ell}{2}\sqrt{\frac{T_R}{Ti}}\left[\gamma S\sqrt{\pi}(1 + \operatorname{erf}(\gamma S) + e^{-\gamma^2 S^2}\right]\right\}. \quad (C.3)$$

---

* Buck, M. L. and E. J. McLaughlin, "A Technique for Predicting Pressure Distributions and Aerodynamic Force Coefficients for Hypersonic Wing Reentry Vehicles (U)," ASP-TDR-63-552, Wright-Patterson AFB, Ohio, August 1963 (Confidential).

** Wojciechowski, C. J., and A. W. Ratliff, "A Study of High Altitude Impingement," LMSC/HREC D149118, August 1969.

The total force in the free molecular regime is obtained by numerically integrating Eq. (C.3) over the body surface. A detailed development of Eq. (C.3) is given in a Lockheed/Sunnyvale document.*

In the transition flow regime the local force is calculated from the following empirical expression from a Lockheed/Huntsville document.**

$$P_{tran} = P_{cont} + (P_{f.m.} - P_{cont}) \sin^2 \left[\pi (1/3 + 1/6 \log_{10} K_n\right]. \qquad (C.4)$$

Equation (C.4) is a function of Mach number and Knudsen number and yields a smooth transition from the continuum to the free molecular flow regime.

C.4 INTEGRATED PRESSURE FORCES AND RESULTING IMPINGEMENT MOMENTS

The integrated forces for the booster are obtained by numerically integrating impact pressure distributions over the individual booster subshapes. The force on an elemental area of a subshape is given by

$$\vec{F}_\ell = P_{imp}\, dA\, \vec{\eta} \ . \qquad (C.5)$$

The resultant force acting the booster due to orbiter exhaust plume impingement is then obtained by summing the forces over each subshape. The

---

* Sentman, Lee H., "Free Molecular Flow Theory and Its Application to the Determination of Aerodynamic Forces," LMSC-448514, Lockheed Missiles & Space Company, Sunnyvale, Calif., October 1961.

** Ratliff, A. W., et al., "Analysis of Heating Rates and Forces on Bodies Subject to Rocket Exhaust Plume Impingement," LMSC/HREC A791230, March 1968.

resultant force acting on the booster and referenced to the booster nose is then expressed as

$$\left\{\vec{F}_{B.N.}\right\} = \sum_{m=1,N} \left(\left[T_{m-B.N.}\right] \sum_{\ell=1,M} \left\{\vec{F}_{\ell}\right\} \right)_m . \qquad (C.6)$$

Since the flow distribution is assumed to be uniform over each elemental area of a given subshape, the resultant force for the elemental area then acts at the centroid of the element. The moment acting on the element area is then given by the expression

$$\vec{M}_{\ell} = \vec{r}_{\ell} \times \vec{F}_{\ell} , \qquad (C.7)$$

where the vector $\vec{r}_{\ell}$ is the distance vector from the origin of the subshape coordinate system to the centroid of the element in question. The resultant moment acting on the booster is given by a summation of the moment distribution over the booster. The mathematical expression becomes

$$\vec{M}_{B.N.} = \sum_{m=1,N} \left(\vec{r}_{\ell-B.N.} \times \left\{\vec{F}_{B.N.}\right\} + \left[T_{m-B.N.}\right] \sum_{\ell=1,M} \vec{M}_{\ell} \right)_m . \qquad (C.8)$$

The impingement calculations assume the flow field to be inviscid. Therefore any boundary layer effects which produce plume impingement outside the calculated plume boundary are disregarded as is any viscous (skin) forces between the plume and the respective subshapes.

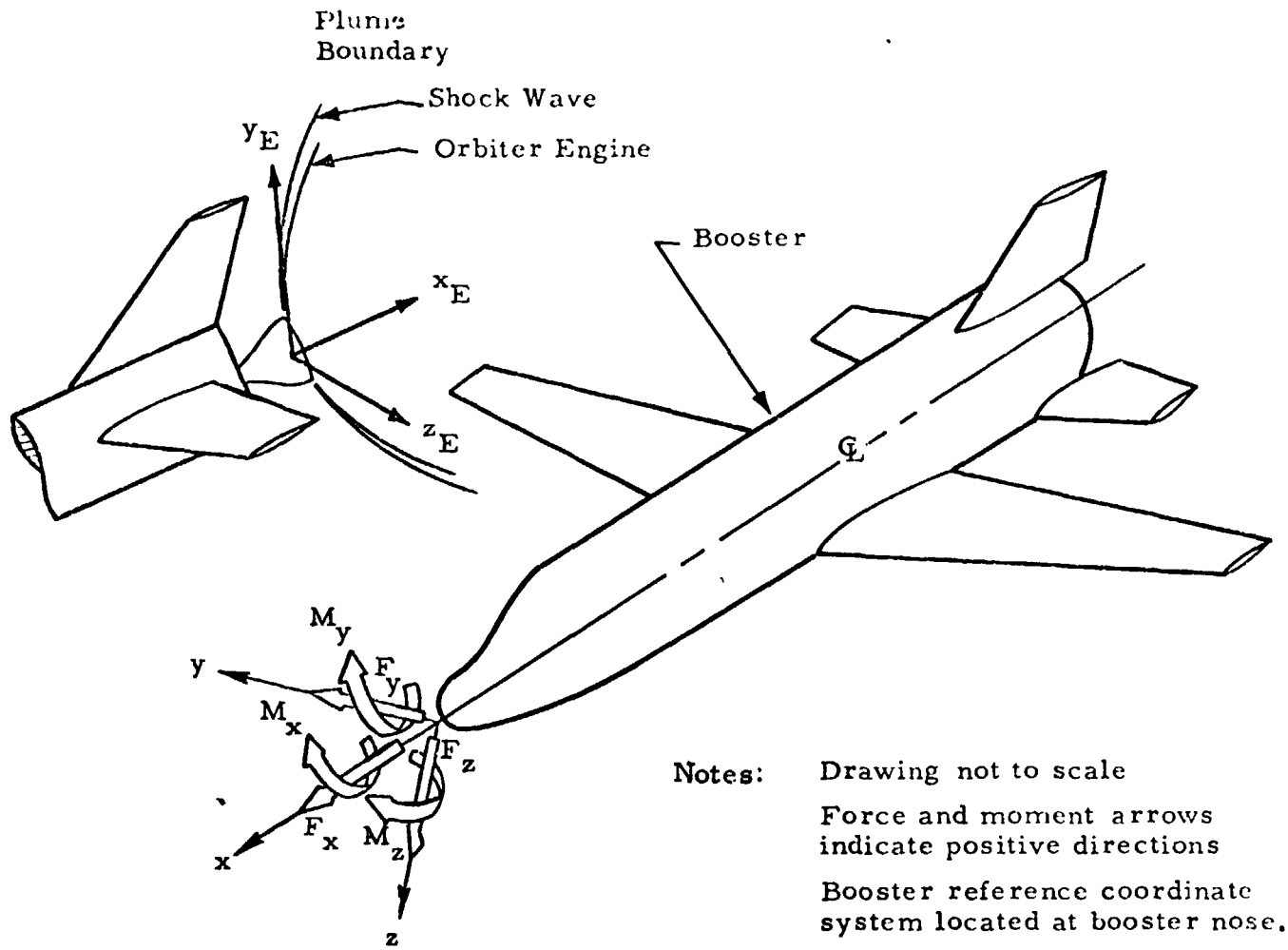

Fig. C-1 - Three-Dimensional Perspective of the Booster Reference Coordinate System and the Orbiter Plume Coordinate System

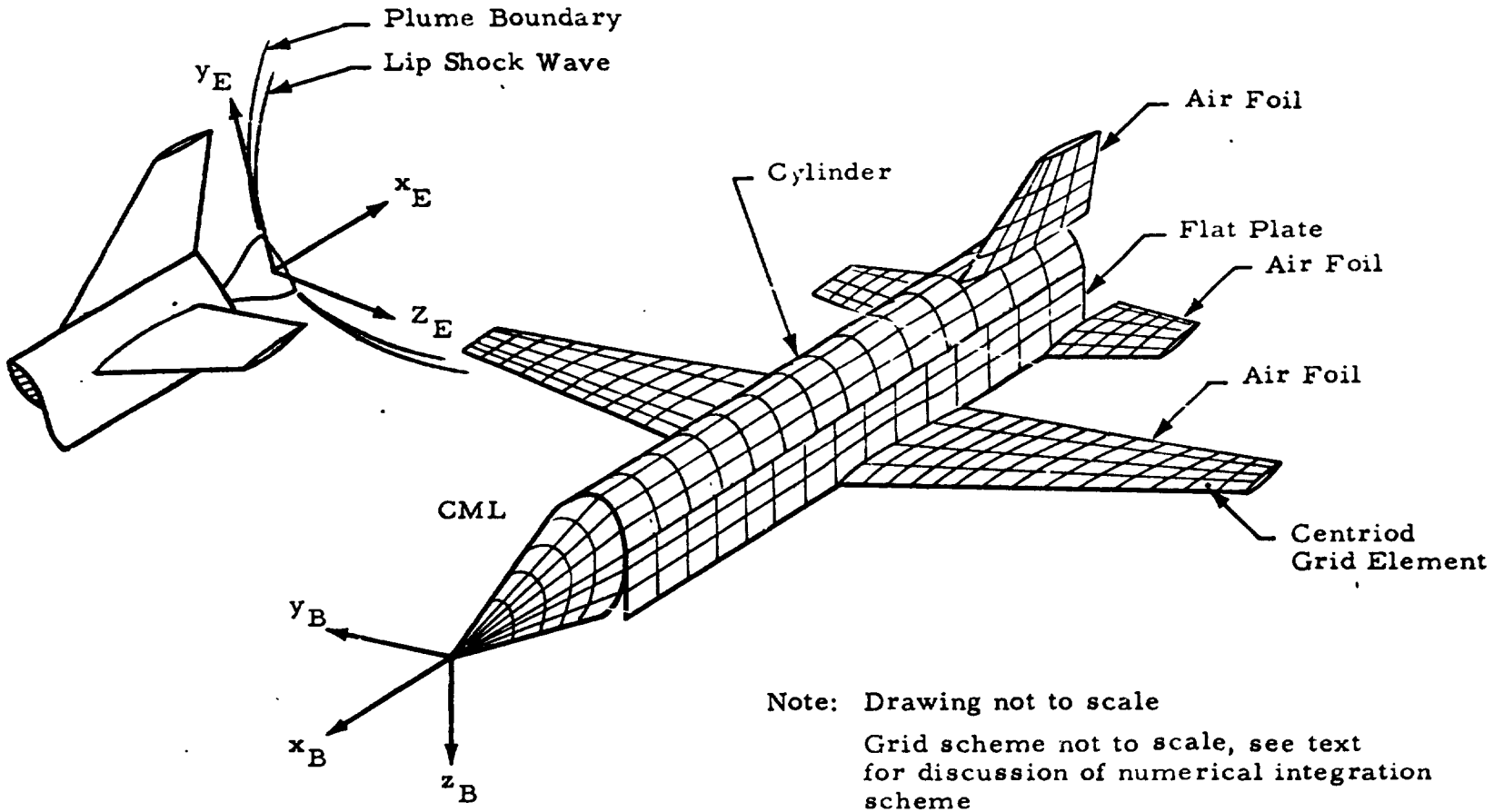

Note: Drawing not to scale

Grid scheme not to scale, see text for discussion of numerical integration scheme

The wing, horizontal and vertical tails are NACA airfoil 0012-64

Impingement data obtained at centroid of each grid element.

Fig. C-2 - Sketch of Subshape System of Grid Scheme Used in the Force, Moment and Heating Analysis

Appendix D
BOOSTER IMPINGEMENT HEATING ANALYSIS

NOMENCLATURE

Symbols

C_p	specific heat (Btu/lbm-^oR)
g	gravitational constant (ft-lbm/lbf-sec^2)
H	total enthalpy (Btu/lbm)
h	static enthalpy (Btu/lbm)
k	thermal conductivity (Btu/Ft-sec-^oR)
M	Mach number
P	pressure (lbf/Ft^2)
Pr	Prantl number
$\dot{q}$	convective heating rate (Btu/Ft^2-sec)
R	radius of cylinder (Ft)
T	temperature (^oR)
t	time (sec)
u	normal component of freestream velocity (ft/sec)
V	velocity (ft/sec)
v	tangential component of freestream velocity (ft/sec)
x	length (ft)

Greek

θ	angle of attack - radians
γ	ratio of specific heats
δ	flow deflection angle - radians

ρ	density (slugs/Ft^3)
μ	viscosity (slugs/Ft-sec)

Subscripts

e	boundary layer edge values
o	frustum stagnation conditions
r	recovery value
s	stagnation line conditions
w	wall conditions
∞	freestream condition ahead of shock
1	property upstream of shock
2	property downstream of shock

Appendix D

This appendix discusses the heat transfer theories used in this study and contained in the plume impingement program (Ref. D.1). For the range of separation distances considered in this study only continuum regime heat transfer theories were used. The boundary layer convective heat transfer theories are discussed in terms of two regions; i.e., the stagnation regions, and the non-stagnation regions.

In the continuum regime, the MSC booster will experience turbulent as well as laminar boundary layer convective heating. For close orbiter/booster separation distances, the local freestream Reynolds numbers for the impinging flow are high and therefore turbulent boundary layer heat transfer theory was used. For large orbiter/booster separation distances, the local freestream Reynolds numbers of the impinging flow are low, and therefore, laminar boundary layer theory was used. The criteria used to establish the state of the boundary layer, i.e., either laminar or turbulent, are also presented in this Appendix.

The following sketch denotes the orbiter engine impingement flow field on the booster. Noted on the sketch are the flow stagnation lines on the leading edges of the wing and tail surface and top of the fuselage. Along these lines, stagnation line heating rate methods were used. For heating rate distributions off the stagnation lines only the component of the flow in the crossflow direction was used. This resulted in simple ratios of local-to-stagnation line heating rates which were strongly dependent on the ratio of local-to-stagnation line pressures. Noted in the sketch are several possible shock/shock interaction areas caused by the fuselage shock envelope intersecting the leading edge shock envelopes.

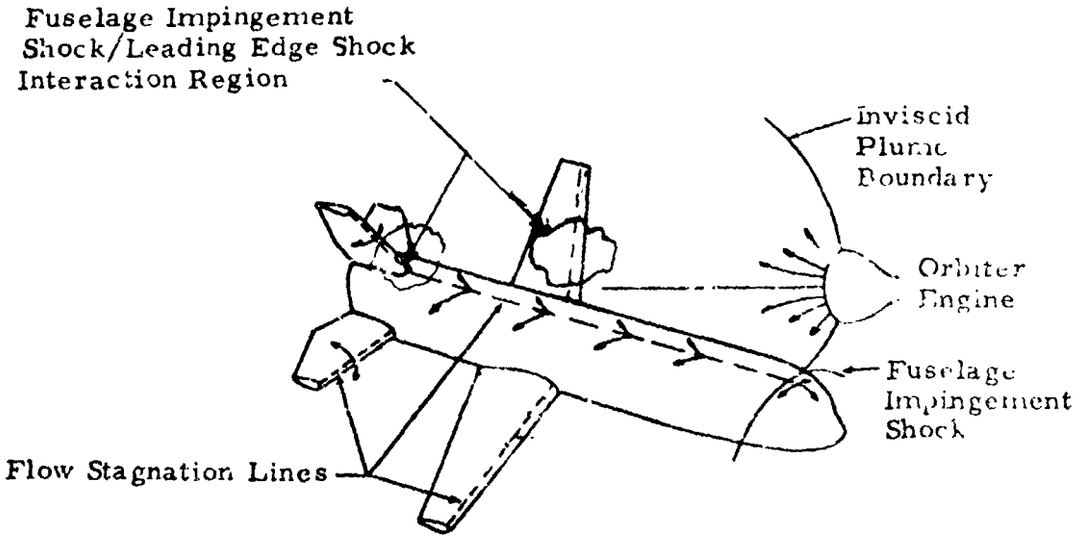

The effects of these shock interactions were treated in this preliminary study in the context of promoting early boundary layer transition. The increased heat transfer in these areas due to vortex impingement will be studied in a subsequent report.

Preceding the discussion on the boundary layer convective heat transfer theories will be a section on the methods used to obtain the local impingement flowfield properties which are used as the inviscid conditions at the edge of the boundary layer in the heat transfer equations.

Following the discussion of the boundary layer transition criteria will be a section discussing the methods used to obtain the structural thermal response to the impingement heating rates.

D.1 LOCAL FLOWFIELD CALCULATION METHOD

This section presents the method used to calculate the local flowfield properties along the stagnation lines on the booster fuselage, wing and tail surfaces. Inviscid analysis methods were used and no boundary layer interactions were treated.

The impingement pressure on the body was calculated using Modified Newtonian theory as discussed in Appendix C. With the pressure along the stagnation line calculated in this fashion, the remaining local flow properties at the boundary layer edge are computed as the real gas conditions behind an oblique shock wave which is parallel to the local body slope.

Basically the solution involves the solution of the continuity, momentum, and energy equations plus an equation of state. The following sketch shows the flowfield geometry.

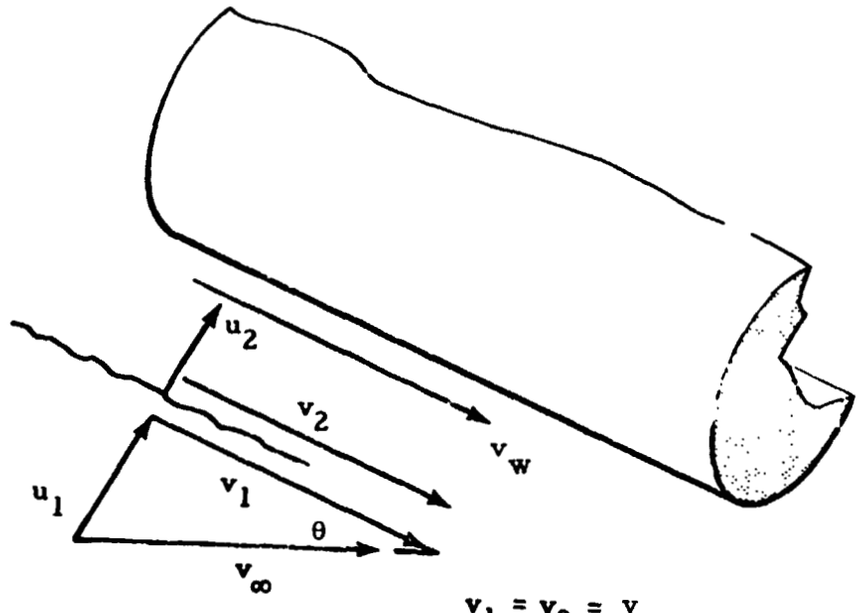

$$v_1 = v_2 = v_w \qquad \text{(D.1)}$$

The pertinent equations are

$$\frac{P_2}{P_1} = 1 + \gamma_1 M_1^2 \left[1 - \left(\frac{u_2}{u_1}\right)\right] \qquad \text{Conservation of Momentum} \qquad (D.2)$$

$$\frac{h_2}{h_1} = 1 + \frac{\gamma_1 - 1}{2} M_1^2 \left[1 - \left(\frac{u_2}{u_1}\right)^2\right] \qquad \text{Conservation of Energy} \qquad (D.3)$$

$$\rho_1 u_1 = \rho_2 u_2 \qquad \text{Continuity} \qquad (D.4)$$

$$\frac{\tan(\theta - \delta)}{\tan \theta} = \frac{U_2}{U_1} \qquad \text{Oblique Shockwave Geometry} \qquad (D.5)$$

where $M_1 = M_\infty \sin \theta$.

An iteration procedure is used to obtain the solution to the preceding set of equations. After the shock solution is obtained, the flow is isentropically decelerated such that u_2 equals zero with a corresponding increase in T_2.

D.2 BOUNDARY LAYER HEAT TRANSFER THEORY

In this section, the boundary layer heat transfer theories are discussed in terms of two regions; i.e., the stagnation regions, and the non-stagnation regions. Both turbulent and laminar boundary layer theories are discussed. The heating rates along the stagnation lines are calculated using yawed infinite cylinder theory.

D.2.1 Stagnation Regions

Turbulent Boundary Layers. The heat transfer rates along the stagnation lines for turbulent boundary layers were calculated using a modified

version of the turbulent swept cylinder theory of Beckwith and Gallagher (Ref. D.2); i.e.,

$$\dot{q} = \frac{0.0288}{Pr_w} \left(\frac{V_\infty \cos\theta}{\mu_s} \right)^{0.6} \left(\frac{dV}{dR} \right)^{0.2} (\rho_w \mu_w)^{0.8} (H_r - h_w) . \qquad (D.6)$$

Modifications to this theory include the introduction of the enthalpy driving potential to make it more applicable to boundary layers in plumes. The complete derivation of Eq. (D.6) is given in (Ref. D.2). Briefly, the integral energy and momentum equations for the turbulent boundary layer on a yawed infinite cylinder are solved using simplifying assumptions for skin friction, velocity and thermal profiles, secondary flow and Reynolds analogy. Eq. (D.6) is based on the assumption of a Blasius flat plate skin-friction law for the flow along the leading edge and zero secondary flow which is valid only at the stagnation line. A comparison of the results of this modified theory with test data is given in Ref. D.3. A typical figure from this work is shown in Fig. D.1.

The transport properties used in the heating rate equation are calculated for the individual gas species using the Lennard-Jones potential model. The mixing laws for obtaining the viscosity and conductivity of the gas mixture are the same as those described in Refs. D.5 and D.6. The velocity gradient can be estimated from Newtonian theory or from the calculated pressure gradients in the stagnation region (Ref. D.4).

If the crossflow velocity component is supersonic, then the velocity gradient is computed by combining the edge of the boundary layer momentum equation with the Newtonian pressure distribution for a cylinder, i.e.,

$$\frac{dV}{dR} = \frac{1}{R} \sqrt{2g \left(\frac{P_s - P_\infty}{\rho_s} \right)} . \qquad (D.7)$$

If the crossflow velocity component is subsonic, then the velocity gradient is computed by the following equation.

$$\frac{dV}{dR} = \frac{V_\infty \sin\theta}{2R}\left[5.1\cos(M_\infty \sin\theta) - 1.6\right]. \qquad (D.8)$$

Laminar Boundary Layer The heat transfer rates along the stagnation lines for laminar boundary layers were calculated using the empirical correlations of Ref. D.7 . The resulting heat transfer correlation obtained was

$$\dot{q} = \frac{0.565}{Pr_w^{0.6}}\sqrt{\rho_w \mu_w \frac{dV}{dR}}\left(\frac{\rho_e \mu_e}{\rho_w \mu_w}\right)^{0.44}(H_r - h_w). \qquad (D.9)$$

This equation agrees closely with the theoretically derived heat transfer equation of Beckwith (Ref. D.26).

D.2.2 Non-Stagnation Regions

Equations (D.6) and (D.9) are valid only along the flow stagnation lines. To obtain heat transfer distributions off the stagnation lines use is made of empirical correlations.

Turbulent Flow. The heating rates off the stagnation lines for turbulent flow were calculated using a modified form of the heat transfer ratio derived in Ref. D.2, i.e.,

$$\frac{q}{q_s} = \left(\frac{P}{P_s}\right)^{\frac{3\gamma-1}{2\gamma}}\left[\frac{\left(\frac{Ps}{P}\right)^{\frac{\gamma-1}{\gamma}} - \frac{Ts}{To}}{1 - \frac{Ts}{To}}\right]^{0.375}. \qquad (D.10)$$

Examination of turbulent heating rate distribution data for swept cylinders revealed that equation D.10 correlated the data better than the original form of the equation presented in Ref. D.2.

Laminar Flow. The heating rate at a point on the surface for an isothermal wall with local similarity assumed can be expressed in terms of the heat transfer rate at the stagnation line by, (Refs. D.8 and D.9).

$$\frac{q}{q_s} = \frac{\left(\frac{P}{P_s}\right)\left(\frac{u_e}{u_\infty}\right)}{\sqrt{2\int_o^s \left(\frac{P}{P_s}\right)\left(\frac{u_e}{u_\infty}\right) ds \left(\frac{dv}{u_\infty R}\right)_c}} \left[\frac{g'(0)}{g'_o(0)}\right] . \qquad (D.11)$$

The above equation consists of the product of inviscid and viscous quantities. The inviscid quantities require a knowledge of the local surface pressure distribution as well as the thermodynamics of the inviscid flow. The viscous quantities, i.e., $g'(0)$ and $g'_o(0)$, require the appropriate solution to the boundary-layer equations which are implicitly related to the inviscid flow through the local surface pressure and pressure gradient. The preceding statements infer a strong dependence of heating rate ratio Eq. (D.11) on the pressure ratio. With this thought in mind, the authors of Ref. D.8 plotted heating rate ratios $q/q_{s'}$ versus pressure ratio P/P_s. The resulting plots represented an equation of the form

$$\frac{q}{q_s} = \left(\frac{P}{P_s}\right)^m . \qquad (D.12)$$

The data indicate that on hemispherical forebodies the exponent m in Eq. (D.12) assumes values between 0.8 and 0.9 while over the afterbody, m assumes values between 0.9 and 1.0. These results demonstrated the strong dependence of heating rate ratio on pressure ratio and are useful for obtaining reasonable estimates of the local heating rates once the stagnation heating rates are known. Examination of heating rate ratios for yawed cylinders revealed the same dependence of heating rate ratio on pressure ratio. The value of m in Eq. (D.12) which correlated the heating rate ratio best was a value of 0.85. Fig. D.2 shows two such correlations over cylinders at angles

of attack of 80 and 50 degrees. Due to the simplicity and speed (short computation time) afforded through the use of Eq. (D.12), this equation was used in this study to obtain heating rates off the stagnation lines.

D.3 BOUNDARY LAYER TRANSITION CRITERIA

The following sketches denote the plume impingement phenomena occurring during the staging maneuver.

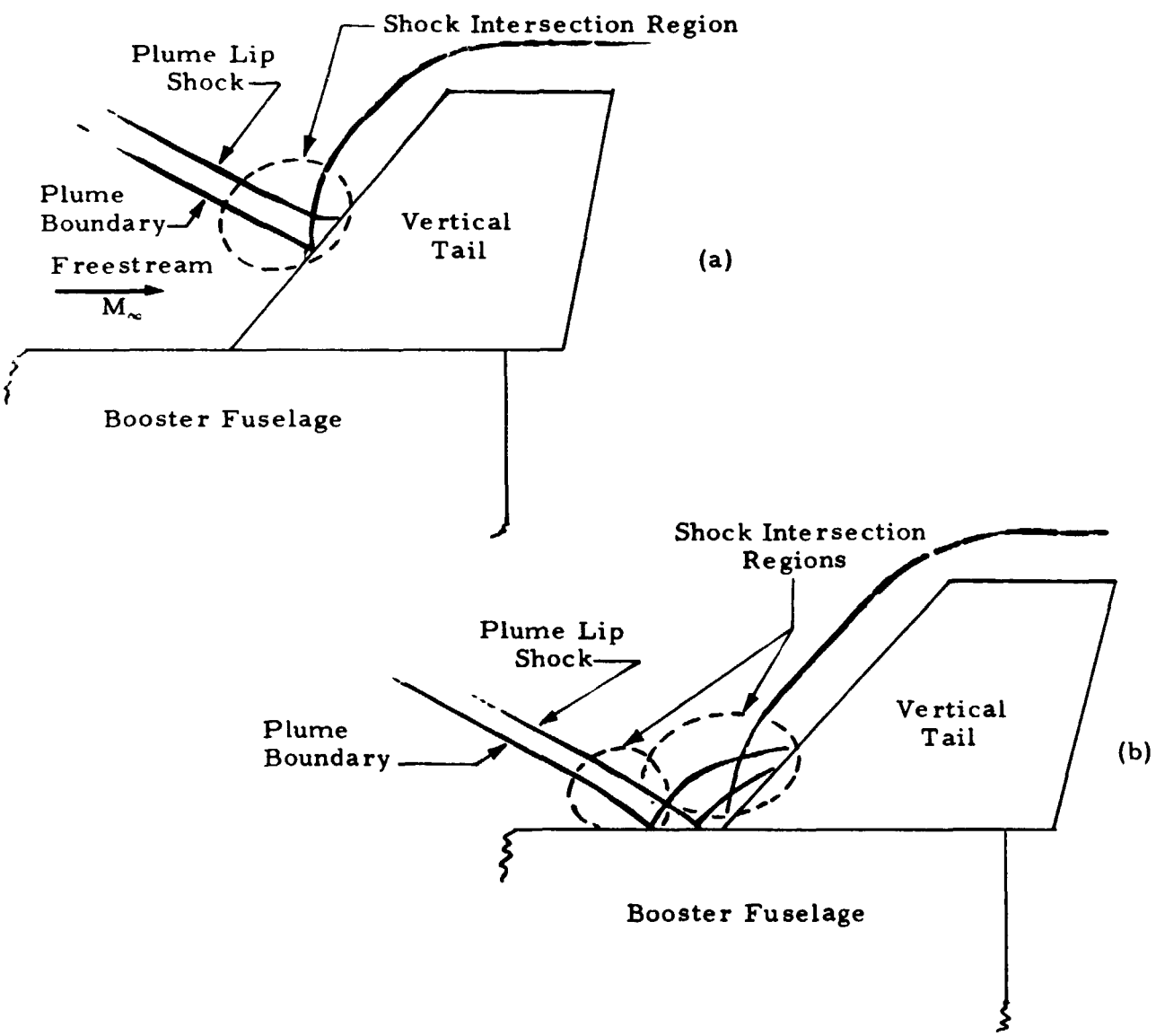

Noted in the sketches are several possible shock intersection regions. Besides the nozzle lip shock intersection with the bow shock there is an additional shock intersection region noted in sketch (B), i.e., the fuselage shock intersection with the vertical tail bow shock.

Several experimental investigations of the leading-edge shock-impingement problem have been conducted over the years (Refs. D.11 through D.22). The available data for boundary layer transition on the leading edge in the presence of an impinging shock wave indicate that transition occurs at Reynolds numbers, based on freestream conditions and leading edge diameter, between 130,000 and 200,000 for sweepback angles of 25 degrees and greater. If the freestream turbulence level present in the plume for this study was also accounted for, the transition Reynolds number would be lower (Refs. D.23 and D. 24. However, in the absence of a detailed study or experimental data on freestream turbulence in the orbiter exhaust plume, the lower limit of 130,000 was used in this study as the boundary layer transition criteria.

D.4 STRUCTURAL THERMAL RESPONSE

The structural temperatures presented in this study were calculated using one-dimensional transient heat conduction theory as programmed in Ref. D.25. Briefly, the material is divided into a series of nodes and an energy balance is performed across each node. For an internal node the energy balance equation is

$$\rho C_p \frac{dT}{dt} = k \frac{dT}{dx} \quad . \qquad (D.13)$$

The term or the left hand side accounts for the change in node temperature with time and the term on the right-hand side accounts for the transfer of heat by conduction.

The energy balance for the surface node contains the additional terms of heat transfer by convection and radiation and is given by,

$$\rho C_p \frac{dT}{dt} = \dot{q}_{conv} - \dot{q}_{rad} + k \frac{dT}{dx} . \qquad (D.14)$$

The above equations were solved using forward-finite difference techniques. Also accounted for were the temperature dependency of the material properties.

REFERENCES

D. 1 Wojciechowski, C. J., and A. W. Ratliff, "Study of High Altitude Plume Impingement," LMSC/HREC D149118, Lockheed Missiles & Space Company, Huntsville, Ala., August 1969.

D. 2 Beckwith, I. E., and J. J. Gallagher, "Local Heat Transfer and Recovery Temperatures on a Yawed Cylinder at a Mach Number of 4.15 and High Reynolds Numbers," NASA TR R-104 (1961).

D. 3 Dean, W. G., C. J. Wojciechowski, and A. G. Bhadsavle, "Convective Heating Rates to Cones and Cylinders at Angle of Attack," Lockheed Missiles & Space Company, Huntsville, Ala., LMSC/HREC D162315, May 1970.

D. 4 Wojciechowski, C. J., and R. J. Rader, "A Method for Calculating Stagnation Region Convective Heat Transfer to Arbitrary Surfaces Immersed in the Space Shuttle Attitude Control System Plumes," LMSC/HREC D162334, Lockheed Missiles & Space Company, Huntsville, Ala., May 1970.

D. 5 Svehla, R. A., "Thermodynamic and Transport Properties for the Hydrogen Oxygen Systems," NASA SP-3011 Lewis Research Center, Cleveland, Ohio, 1964.

D. 6 Dorrance, W. H., Viscous Hypersonic Flow, McGraw-Hill, New York, 1962.

D. 7 Kemp, H. H., P. H. Rose, and R. W. Detra, "Laminar Heat Transfer Around Blunt Bodies in Dissociated Air," JAS (1959).

D. 8 Marvin, Joseph G., and C. M. Akin, "Pressure and Convective Heat Transfer Measurements in a Shock Tunnel Using Several Test Gases," NASA TN D-3017, September 1965.

D. 9 Marvin, Joseph G., and A. R. Sinclair, "Convective Heating in Regions of Large Favorable Pressure Gradient," AIAA J., Vol. 5, No. 11, November 1967, pp 1940-1948.

D.10 Bergquam, J. E., "Aerodynamic Heating Investigation of Cylindrical Configurations in AEDC Tunnel C(R-128), LMSC-805538, Lockheed Missiles & Space Company, Sunnyvale, Calif., November 1965.

D.11 Bushnell, Dennis M., "Effects of Shock Impingement and Other Factors on Leading Edge Heat Transfer," NASA TN D-4543, April 1968.

D.12 Beckwith, Ivan E., "Experimental Investigation of Heat Transfer and Pressures on a Swept Cylinder in the Vicinity of Its Intersection with a Wedge and Flat Plate at Mach Number 4.15 and High Reynolds Numbers," NASA TN D-2020, 1964.

D.13 Jones, Robert A., "Heat-Transfer and Pressure Investigation of a Fin-Plate Interference Model at a Mach Number of 6," NASA TN D-2028, 1964.

D.14 Bushnell, Dennis M., "Interference Heating on a Swept Cylinder in Region of Intersection with a Wedge at Mach Number 8," NASA TN D-3094, 1965.

D.15 Gulbran, C. E., E. Redeker, D. S. Miller and S. L. Strack, "Heating in Regions of Interfering Flow Fields. Part II: Leading Edge Shock Impingement," AFFDL-TR-65-49, Pt. II, U.S. Air Force, Jan. 1967.

D.16 Newlander, Robert A., "Effect of Shock Impingement on the Distribution of Heat-Transfer Coefficients on a Right Circular Cylinder at Mach Numbers of 2.65, 3.51, and 4.44," NASA TN D-642, 1961.

D.17 Hiers, Robert S., and William J. Loubsky, "Effects of Shock-Wave Impingement on the Heat Transfer on a Cylindrical Leading Edge," NASA TN D-3859, 1967.

D.18 Francis, W. Leon, "Experimental Heat-Transfer Study of Shock Impingement on Fins in Hypersonic Flow," J. Spacecraft Roc., Vol. 2, No. 4, July-August 1965, pp. 630-632.

D.19 Siler, L. G., and H. E. Deskins, "Effect of Shock Impingement on the Heat-Transfer and Pressure Distributions on a Cylindrical-Leading-Edge Model at Mach Number 19," AEDC-TDR-64-228, Arnold Air Force Station, Tenn., November 1964.

D.20 Knox, E. C., "Measurements of Shock-Impingement Effects on the Heat-Transfer and Pressure Distributions on a Hemicylinder Model at Mach Number 19," AEDC-TR-65-245, Arnold Air Force Station, Tenn., November 1965.

D.21 Ray, A. D., and R. L., Palko, "An Investigation of the Effects of Shock Impingement on a Blunt Leading Edge," AEDC-TR-65-153, Arnold Air Force Station, Tenn., July 1965.

D.22 Bushnell, Dennis M., and Jarrett K. Huffman, "Investigation of Heat Transfer to Leading Edge of a 76° Swept Fin With and Without Chordwise Slots and Correlations of Swept-Leading-Edge Transition Data for Mach 2 to 8," NASA TM X-1475, 1967.

D.23 Broslow, Albert L., "A Review of Factors Affecting Boundary-Layer Transition, NASA TN D-3384, 1967.

D.24 Blackledge, M. L., "Evidence of a Unified Transition Theory for Turbulent Flows," LMSC/HREC D162423, Lockheed Missiles & Space Company, Huntsville, Ala., August 1970.

D.25 Wojciechowski, C. J., "Development of a Method and Digital Computer Program to Determine Ablative Material Impulse," LMSC/HREC A782808, Lockheed Missiles & Space Company, Huntsville, Ala., 15 November 1966.

D.26 Beckwith, I.E., "Similar Solutions for the Compressible Boundary Layer on a Yawed Cylinder with Transpiration Cooling," NASA TR-R-42, 1959.

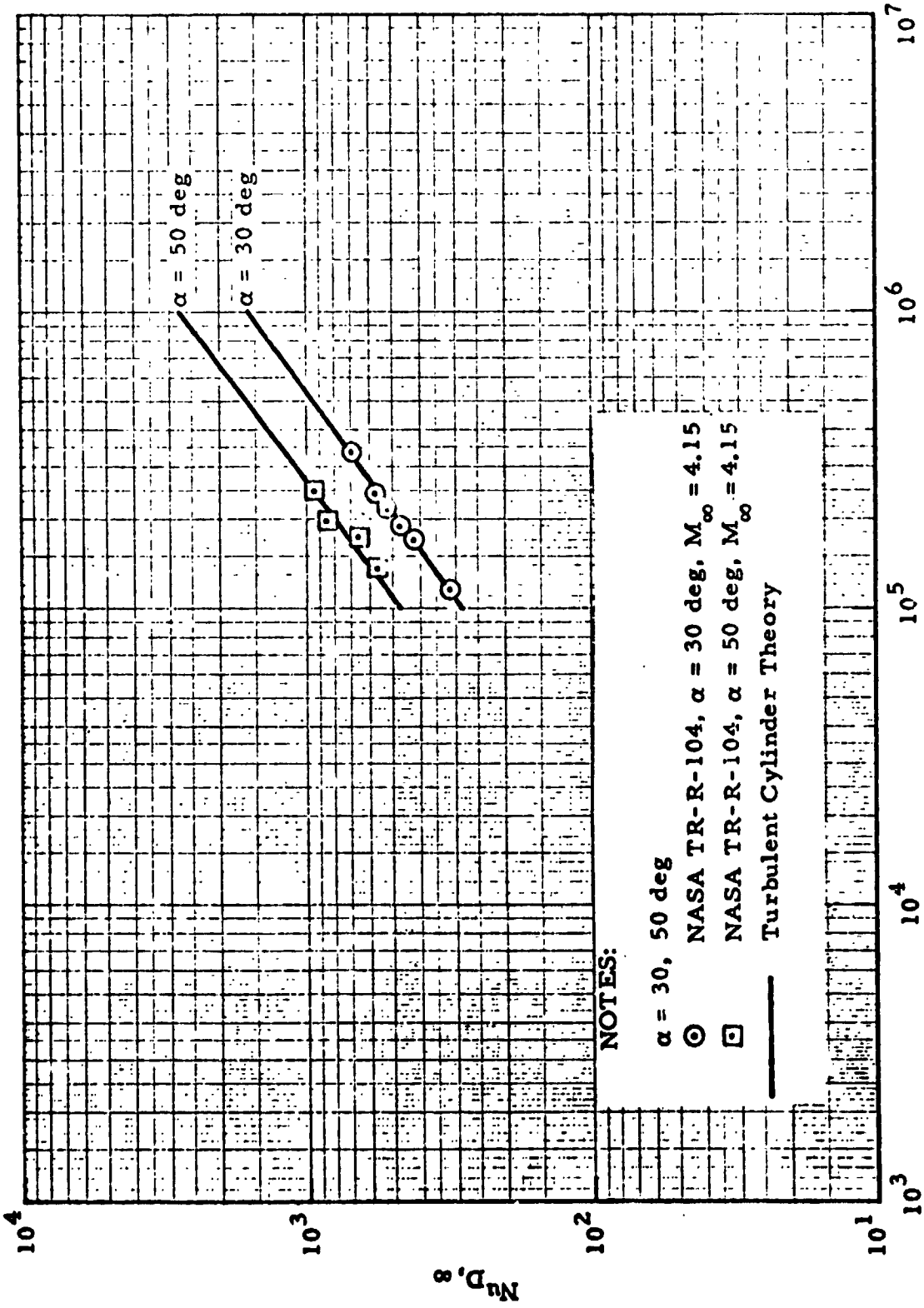

Fig. D-1 - Freestream Nusselt Number vs Freestream Reynolds Number for Turbulent Flow over Cylinders at α = 30 and 50 Degrees

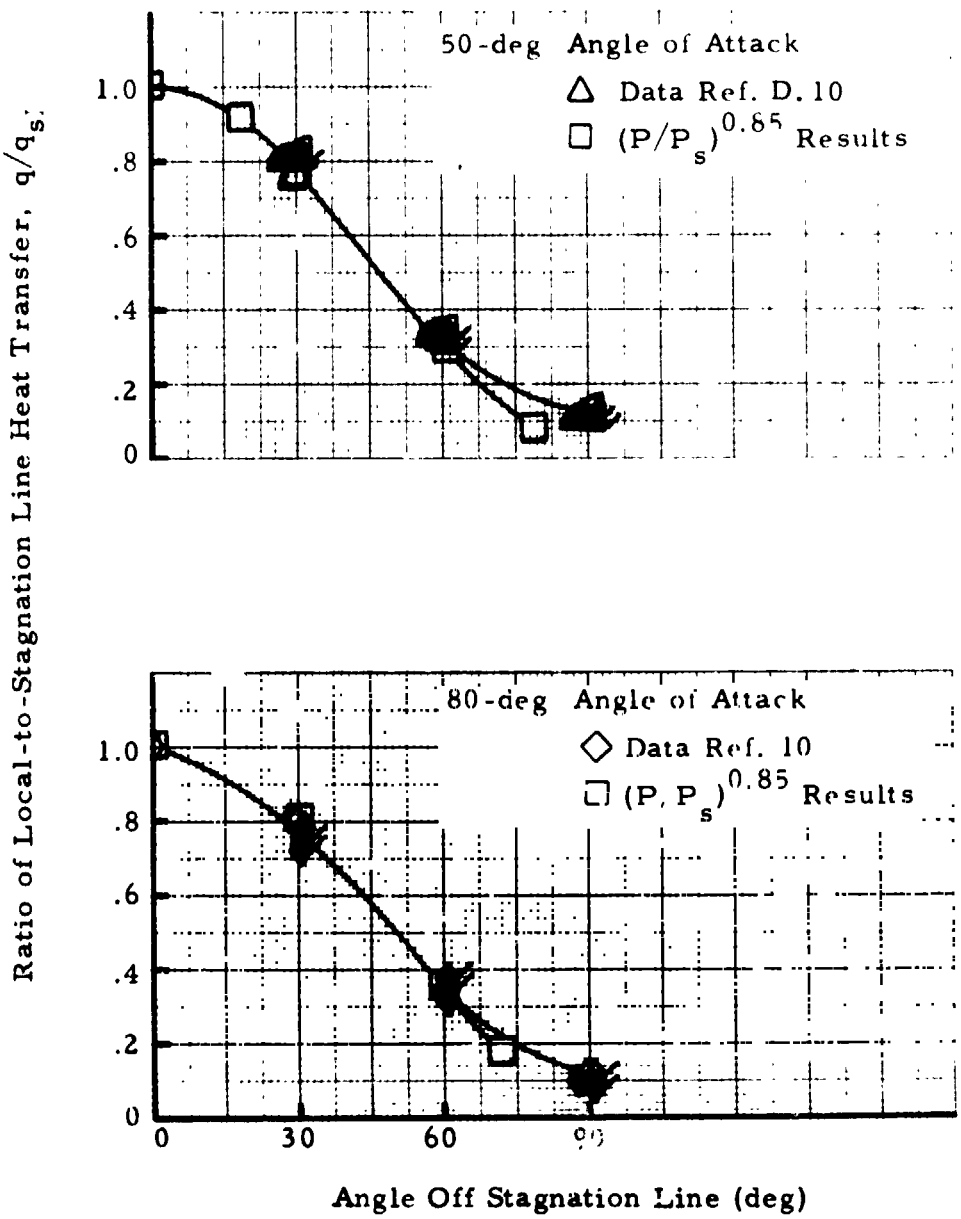

Fig. D-2 - Chordwise Laminar Heating Distribution